UNIVERSITY OF CALIFORNIA

RIVERSIDE

Garnet Materials Development and Spin Transport Phenomena in Magnetic Insulator/ Normal Metal Heterostructures

A Dissertation submitted in partial satisfaction
of the requirements for the degree of

Doctor of Philosophy

in

Physics

by

Mohammed Hamad R Aldosary

September 2018

Dissertation Committee:

Dr. Jing Shi, Chairperson
Dr. Ward P. Beyermann
Dr. Yongtao Cui

The Dissertation of Mohammed Hamad R Aldosary is approved:

Committee Chairperson

University of California, Riverside

Acknowledgements

The dream of Ph.D. achievement in Physics becomes finally true and the journey comes to the end. Throughout six years of research journey, I have experienced massive exciting, enjoyable and productive moments, as well as some anxious, stressful and sad times. However, they all not only turn out to be unforgettable and invaluable memories when I remember them now, but also sharpen my critical thinking for scientific career. That is why I am grateful for University of California, Riverside to give me an opportunity to pursue my Ph.D. here and teach me all different research skills as a foundation for future research. Besides that, I would like to thank a lot of people who help me in many ways throughout my Ph.D. study.

First and foremost, I would like to express my most sincere gratitude to my thesis advisor, Prof. Jing Shi for his extensive support, advice, encouragement and guidance. Prof. Shi is great scientist who not only inspires me with his rich and scientific knowledge to visualizes and understand clear physics pictures in research projects but also his unique passion and motivation to explore new physics ideas and how to do them experimentally in clever ways. He is helpful and patient during discussions of updated projects results trying to clarify difficult parts and giving insightful comments and suggestions. With great enthusiasm and supervision of Prof. Shi, I collaborate with other groups inside and outside campus resulting in successful publishing papers and some ongoing projects. Prof. Shi, thank you very much for invaluable mentorship.

I am also very grateful to all my thesis committee members: Prof. Ward P. Beyermann and Prof. Yongtao Cui for giving me valuable suggestions and comments on my Ph.D. projects. I would like to thank the other two oral exam members Prof. Peng Wei and Prof. Jianlin Liu for useful feedbacks and comments. Furthermore, I would like to thank cleanroom staff in the Center for Nanoscale Science and Engineering. They are Mark Heiden, Nissim Amos, Dong Yan, John Butler, Frank Lee for their technical assistance on nanofabrication equipment. I would like to thank Glenda Barraza and Dorothea Northcut in SHINES center for big help of dealing with many lab items orders, shipping and reimbursements.

I want to acknowledge my previous and current colleagues in Prof. Shi lab for interesting discussions and helpful assistance and training to build up my current scientific experience. They are Zhiyong Wang, Hamad Alyahyaei, Zilong Jiang, Chi Tang, Zhisheng Lin, Bowen Yang, Victor Ortiz, Yawen Liu, Mark Lohmann, Jhen-Yong Hong, Benjamin Madon, Zhong Shi, Mohammed Alghamdi, Tang Su and Wei Yuan. Additional thanks go to postdoc. Dr. Junxue Li for his strong motivation towards research work particularly during discussions of updated results, new ideas and some concepts in spintronics. I want also to thank all my friends in Riverside for great conversations, support and friendship. Sincere wishes for you all on your research and career.

I would like to thank all collaborator groups inside UCR and from other universities for their useful discussions and exchange results and ideas. They are Prof. Igor Barsukov and Bassim Arkook from UCR, Prof. Nathaniel Gabor and Max Grossnickle from UCR, Prof. Richard Wilson and Michael Gomez from UCR, and Prof.

Javier Garay and Chad Warren from UCSD, Prof. Kang Wang and Aryan Navabi from UCLA, Illya Krivorotov and Chris Safranski from UCI and Prof. Ken Burch and Yiping Wang from Boston College.

I also want to express my deep appreciation to King Saud University for giving me six years scholarship to study Ph.D. and offering me a faculty position after I come back. Thanks go also to Saudi Arabian Cultural mission for great financial support and consistent management care and encouragements.

At last, I want to express my sincere gratitude and deep love to my big family members; My parents, my brothers, my sisters, my wife, my cousins, and all Aldosary community; for their true love, huge support emotionally, morally and financially, encouragements and trust. They all stand behind me for any challenges or difficulties that I faced with strong help for finding suitable solutions. I am proud of my whole family and I cannot accomplish what I have today without them being in my life. I love you all forever!

ABSTRACT OF THE DISSERTATION

Garnet Materials Development and Spin Transport Phenomena in Magnetic Insulator/ Normal Metal Heterostructures

by

Mohammed Hamad R Aldosary

Doctor of Philosophy, Graduate Program in Physics
University of California, Riverside, September 2018
Dr. Jing Shi, Chairperson

The Nobel prize was awarded in 2007 due to the big discovery of the giant magnetoresistance effect (GMR) in 1988 giving birth to the new, spin-based electronics or spintronics. In addition to the charge degree of freedom, spin degree of freedom of electrons has attracted a great deal of research interest in the last two decades. Based on electron spin, technology of spintronics has emerged with new device functionalities and decreased electric power consumption. For example, applications such as computer read-heads and magnetoresistive random access memories are based on spin-dependent effects that originate from interaction between spin of the carriers and the magnetic properties of the materials. Therefore, making new magnetic materials and understanding their magnetic properties is very important. This work focuses mainly on rare-earth iron garnet magnetic insulator (REIG-MI) materials and heterostructures of REIG-MI and heavy metals (strong spin-orbit coupling). These REIG-MI materials have unique properties of large electronic band gap, room temperature ferrimagnetism and long spin wave

propagation length and thus are ideal materials for low-power spintronics. Heterostructures of REIG-MI and heavy metals give rise to a variety of interesting effects such as the spin Seebeck effect and the spin Hall magnetoresistance effect.

This dissertation summaries all my work in past five years and is divided into seven chapters. The first chapter starts off with a short introduction to magnetism by explaining fundamental concepts as an entrance to spintronics field and then some important transport phenomena in spintronics. The last part is devoted to the importance of thin films and critical role of interface properties and interface engineering.

The second chapter presents the state-of-the-art growth of yttrium iron garnet (YIG). A special emphasis is placed on optimizing growth conditions using pulsed laser deposition (PLD). Epitaxial growth with the layer-by layer mode, growth of strained single crystal YIG and polycrystalline YIG development are discussed in detail with full characterization results.

The third chapter shows a breakthrough of the growth of YIG on the top of Pt, an inverted bilayer structure, where we overcome the Pt stability problems related to high temperature growth or annealing. Mastering growth control leads to single crystal phase for YIG and Pt in the inverted structure with flat and sharp interface.

The fourth chapter mainly discusses the experimental observation of theoretically predicted magnon-mediated current drag effect in HM/FMI/HM heterostructures, here HM denoting heavy metal either Pt or Ta, and FMI denoting ferrimagnetic insulator YIG. This system is ideal to realize SHE in one HM layer and detect ISHE in the second layer

of HM. More importantly, distinctive behaviors of this effect are studied via nonlocal voltage response as a function of magnetic field strength, angles and temperature with comparison to local signal of SMR and SSE.

The fifth chapter shows the observation of a giant magnetoresistance (GMR) effect in spin valve-like structure consisting of two identical magnetic insulator layers of YIG where they are separated by a non-magnetic metal layer. Magnetization of anti-parallel state between two layers gives rise to high resistance. SSE measurements confirm individual contribution of thermal spin current from each YIG layer.

Chapter six describes the interface modulated spin dynamics of magnetic insulator (YIG)/Pt bilayers with engineering different resistivities of Pt layer. Gilbert damping constant is tuned based on Pt resistivities and interfacial spin mixing is investigated. Both cavity FMR and broadband FMR with coplanar waveguide set-up are used.

Chapter seven discusses strain effect to tune magnetic anisotropy from in-plane to out-of-plane via magnetostriction effect utilizing strain modulation over a wide range of thicknesses ranging from 5 to 100 nm in TbIG. Study of anomalous Hall and compensation effects on these thicknesses are investigated.

Contents

List of Figures

List of Tables

Chapter 1 Introduction to Magnetism and Spintronics

1.1. Brief Introduction to Magnetism

1.1.1. Magnetic Moment of Individual atoms

In February 1922, modern magnetism just begun when Stern and Gerlach experimentally discovered the electron can be defined by two possible magnetic states proving the space quantization of the magnetic moments of atom besides its charge *e* when they fired a beam of silver atoms across an applied magnetic field.[1] Three years later, Unhelnbeck and Goudsmit postulated theoretically that the electron possesses an intrinsic angular momentum (spin) with two possible states of spin up and spin down.[2] Electrons are the main sources of magnetic moment in solids and each electron has two distinct sources of angular momentum, one is spin and the other is orbital motion around the nucleus. This spin has a quantum number $s = \frac{1}{2}$ and there is intrinsic magnetic moment association with, unrelated to orbital motion, which can only espouse one of two orientations when they interact with magnetic field. More importantly, the magnetic moment associated with the electron spin turns out not be a half but almost exactly one Bohr magneton. [3] The magnetic moment here defines $m = -\frac{e}{m_e} s$ and there are only two possible angular momentum states stating magnetic quantum number value by $m_s = \pm\frac{1}{2}$. Therefore, the magnetic moment in a direction, chosen z, will be $m_z = -\frac{e}{m_e} m_s \hbar$ with spin angular being quantized in unit of $\hbar$. when electrons revolve around the nucleus

in circular orbits because of the Coulomb force influence are equivalent to a current loop when the current direction is opposite to the sense of circulation due to electron charge being negative. The magnetic moment associated with the current loop in term of angular momentum is: $m = -\frac{e}{2m_e}\, l$. The relation between the magnetic moment and angular momentum defines as: $m = \gamma\, l$ where γ is known as the gyromagnetic ratio and it is equal to $-\left(\frac{e}{2m_e}\right)$ for orbital motion. Then, the magnetic moment competent in a particular direction, chosen as z-direction, with orbit angular momentum being quantized in the unit of $\hbar$ is $m_z = -\frac{e}{2m_e}\, m_l \hbar$ where m_l is an orbital magnetic quantum number and its value is (0, ±1, ±2, …). We need to introduce the constant and natural unit for expressing magnetic moment of an electron which can originate from either the orbital or the spin angular momentum and that called Bohr magneton that is defined as $\mu_B = \frac{e\hbar}{2m_e}$. Comparing orbital to spin momentum for creating magnetic moment, the spin angular momentum is twice as efficient as orbital angular momentum.[3] As a result, for a given atom or ion, the total magnetic moment is the sum of each magnetic moment of each electron which includes the sum of both contributions: $m_T = -\mu_B(l + 2s)$ with emphasis of m_T is noncollinear with total kinetic energy moment $l_t = l + 2s$.[4] based on that, magnetic moment comes from electrons of unfiled shells which constrain by Hund's rule and Pauli exclusion principle. Filled shells do not contribute to magnetization and nuclei contribution is much smaller compared to electron.[4] Now, after identifying origin of magnetic moment, it is time to discuss how these ordered electrons coupled to each other to determine the magnetic ordering through exchange interaction and different

magnetic anisotropy types to specify magnetic easy axis which they are produced by spin-orbit interaction effect.

1.1.2. Exchange Interaction

The exchange interaction was first proposed by Heisenberg [5] in 1928 stating that there is interaction energy between atoms with spin S_i and S_j and thus the exchange Hamiltonian is $H = -2 J_{ij} S_i . S_j$ where J_{ij} is the exchange integral or exchange constant, which gives the strength to the interaction. Therefore, this kind of interaction couples the total spin S of two nearby atoms (labeled i and j) leading to the magnetic order. We should point out that the origin of the exchange interaction is due to the interplay between Pauli principle and Coulomb repulsion between electron. Exchange interaction stabilizes the magnetic moments in both isolated atoms (via Hund's rules) and solid materials also determines the magnetic ordering classifying the materials' type in terms of magnetization. For example, if $J_{ij} > 0$, then the energy is lowest when $S_i \parallel S_j$ and the magnetic moments align in the same direction forming ferromagnetic (FM) alignment which is stable.[5] Ferromagnets have a spontaneous net magnetization which means in the absence of an applied magnetic field, there is a net magnetic field such as iron (Fe), cobalt (Co) and NiFe (Py). It is obvious that the exchange is short-range interaction telling us the value of J_{ij} is largest for nearest-neighbor spins forcing theses spins to be

parallel for positive J_{ij}. Furthermore, if $J_{ij} < 0$, then the spins align in opposite direction preferring anti-parallel state to be stable and if the net magnetic moment is equal to zero, this type called antiferromagnetic (AFM). We should mention here, Curie temperature (T_C) which is related to exchange coupling and thermal energy exceeds coupling, the magnetic order is lot and the material become paramagnetic. In the case of AFM, it is called Neel temperature (T_N). In brief, listing two different type of exchange interaction mechanisms here, the simplest case is direct exchange which is coupled each spin to the nearest- neighbor directly. The second one is called super-exchange (indirect exchange) which means the magnetic ions are separated by non-magnetic oxygen ions. It occurs because of hybridization between *d* orbitals and p orbital of oxygen ions. This kind of interaction is important in this thesis and it will mention a lot for iron garnet material such as (YIG) and the coupling is usually antiferromagnetic, but it can also be positive as in EuO.

1.1.3. Spin-Orbit Coupling

Spin-orbit coupling (SOC) whose origin is relativistic is the interaction between electron's spin and its angular momentum. SOC occurs because, at large orbital velocity of electron, the electric field due to positive nucleus is transformed relativistically into a magnetic field that couples to the electron spin[5,6]. Hamiltonian's term relevant to SOC contribution described as[7]

$$H_{SOC} \approx \frac{g_e}{2}\frac{e}{m^2c^2}\frac{1}{r}\frac{\partial V(r)}{\partial r} s.l$$

Where g is the electron g factor, e and m are electron charge and mass, c is the speed of light, $V(r)$ is the Coulomb interaction and s and l are spin and orbital angular momenta of electron for a given atom. Also, the strength of SOC (λ_{nl}) depends both on the potential $\frac{\partial V(r)}{\partial r}$ which increase as nuclear charge increases and radial wave function of the orbital $\psi_{nl}(r)$ with quantum number n and l and it is well-known the SOC strength (λ_{nl}) increases rapidly with the atomic number Z. If nuclear charge scaling simply holds, then *4d* orbitals in transition metals should have much stronger SOC than *3d* following simple arguments based on the hydrogen atom wave functions lead to a Z^4 dependence[6]. However, *4d* orbitals have a node in the radial wave function lowering amplitude deep in the core where SOC potential is the highest[7]. Thus, the *4d* elements in the left section of the periodic table have lower SOC than the 3d elements in the right section. Therefore, there is some confusion in the literature about how rapid increase is and the correlation between the (λ_{nl}) and the effect of SOC in solids is complicated and requires band structure calculations.[6,7]

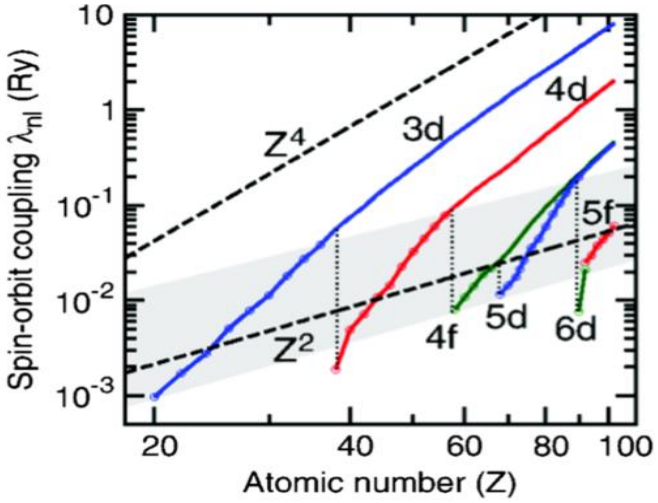

Figure 1- 1: Dependence of the individual orbital spin-orbit coupling strength (λ_{nl}) for atoms as a function of their atomic number Z. Colored lines are calculated using Hartree-Fock method and compared to hydrogenic dependence $\boldsymbol{Z^4}$. Circles and shaded area are for outermost electrons which are the relevant electron in solids. Adapted from K. V. Shanavas et al. PRB 90, 165108 (2014).

As it can be seen in Fig. (1-1), Z^4 power dependence is not bad for large Z nonetheless the SOC strength (λ_{nl}) far smaller than the Z^4 dependence naively expected which should not be surprising because the hydrogen calculation neglected the screening of the nuclear potential by the innermost core electron.[5] On the other hand, considering outermost electrons which their quantum number *n* and *l* change with Z for the atoms, the (λ_{nl}) increase much more slowly following roughly the Landau-Lifshitz Z^2 dependence (showed by dots and shaded area).[6, 7, 8]

The significant result of SOC is physical origin of the anisotropy in which connect the magnetization direction to the crystal lattice causing preferential direction of magnetization **M**. Thus, different kind of anisotropies will be discussed in the next section.

1.1.4. Magnetic Anisotropy

Magnetic anisotropy energies derive in principle from two factors, the spin–orbit coupling and the magnetostatic dipole–dipole interaction.[9,10] Thus, they influence significantly the materials' electronic structure determining the orientation of magnetization.[9] I will describe briefly three different anisotropies as they are studied in this thesis.

- **Magneto-crystalline anisotropy** is intrinsic to the material since it depends on the crystal structure and the origin for this anisotropy is mainly due to spin-orbit coupling and orbital-lattice coupling (crystal-field interaction).[9,10] Together, these two sources result in set of directions along which the energy of the system (material) is minimized and consequently magnetic measurements along different crystallographic directions yield different magnetization directions reflecting the crystal symmetry. In this case, this symmetry tends to align the moments along one axis which defines as easy axis and therefore, different crystal directions give different saturation when they are subjected to a magnetic field. [11] This anisotropy occurs in either bulk or thin film materials and it is typically weak in materials with cubic symmetry due to the large number of symmetry axes, but it can be quite large in materials with large spin-orbit coupling and uniaxial symmetry.[11]

- **Shape anisotropy** is magneto-static phenomenon which is produced by the magnetic dipole -dipole interaction describing the magnetic field produced at each spin by all the surrounding spins in the material.[10] This magnetic dipolar interaction between spins is much weaker than the exchange interaction (short-range), but it become dominant at long distance and hence it is long-range interaction. Here, dipolar energy tends to create a demagnetization field anti-parallel to the magnetization direction to minimize the energy occurring from the charges on the surface of magnetic materials. Therefore, without other terms this anisotropy constrains the magnetization to align in the direction to minimize magneto-static energy. Furthermore, this dipole depends on the material's shape, so in the case of thin films, the number of free charges is larger on the surface than the edge imposing the magnetization to be in-plane direction. The shape energy term for thin film is ($K_{shape} = \frac{1}{2} N {M_s}^2$)[10] where N is the demagnetization factor and it is equal to (4π).

- **Strain Anisotropy** is a magneto-elastic effect which arises again due to the spin-orbit interaction.[9] One approach to engineer a large magnetic anisotropy field for magnetic thin films, epitaxial strain can be utilized due to lattice mismatch between the thin films and substrate and the energy term here is ($K_{strain} = \frac{3}{2} \lambda \sigma_{\parallel}$) where is λ magnetostriction coefficient and $\sigma_{\parallel}$ is related to in-plain strain.[9] For example, if λ is positive, then compressive strain is

required and vice versa to produce a change in preferred magnetization direction from in plane to perpendicular (normal to the surface). The strain anisotropy effects typically relax with a few nanometers for metallic systems whereas the relaxation is very slow in magnetic insulators in which strain effect persists up to ~ 100 nm. Strain modulation is of great importance in the nanomagnetism and nanostructures applications and the last chapter of this thesis is about strain induced magnetic anisotropy in ($Tb_3Fe_5O_{12}$). On the other hand, there are other kinds of anisotropy such as surface anisotropy and growth-induced anisotropy which are not studied in this thesis.

1.2. Spin Transport Phenomena Based Spintronics

1.2.1. Spintronics Overview

The field of spintronics (spin electronics), or magneto-electronics [12], is the area of condensed matter physics which explores phenomena that interlink the spin and charge degrees of freedom to control equilibrium and non-equilibrium properties of materials and device. [13, 14] The pioneering independent work of Albert Fert and Peter Grunberg led to the discovery of the giant magnetoresistance (GMR) effect in 1988 and they were awarded the Nobel Prize in physics in 2007. Such a discovery is genesis to a new field called spintronics and the operational principle of GMR is based on spin valve structure in which nonmagnetic spacer of nanometer thickness sandwiches between two

ferromagnetic layers. Based on magnetic state controlled by applied magnetic field, either the two are parallel and the valve is open or in low resistance state or the two are anti-parallel and the valve is closed or in high resistance state. [15] Since this discovery, GMR and later the tunneling magnetoresistance (TMR) [16] became an integral part in magnetic hard disk drives giving strength to commercial spintronics. [17]

Generation, manipulation, and detection of spin current is one of significant parts in the field of spintronics. So, in a complete analogy to charge current, spin current is described as a flow of a spin angular momentum $\hbar$ and can be employed to transport, carry and process information. [18] This spin angular momentum can be carried by moving (or conduction) electrons or magnons where electrons that have spin angular momentum do not move, but spin precesses locally. Thus, Magnons; quantized particles of spin waves; are representing a low-energy excited state of magnetic materials and a flow of magnons during non-equilibrium magnetic excitations implies a flow of angular momentum (spin current). Furthermore, a magnon is a boson and carries basic spin angular momentum quanta of $\boldsymbol{\hbar}$. [19] Generation of spin current can be achieved in several ways. To list a few, first, electrical spin injection method used to transfer angular momentum from magnetic materials to adjacent normal metal layer and such experiment is nonlocal geometry. Second method is spin pumping where the spin angular momentum is transferred from magnetization precession motion to conduction-election in adjacent normal layer such as Pt. Furthermore, thermal method is another way of making pure spin current. Comparing magnetic insulators (electrically insulating with frozen charge degree of freedom) to ferromagnetic metals, magnetic insulators, firstly, can generate

only a pure spin current without accompany of charge current which led to no Joule heating dissipation and secondly, spin wave decay length is persistent for much greater distance than ferromagnetic materials.

One of the most outstanding recent developments based on theoretical prediction and experimental verification is topological insulators materials showed dissipationless gapless edge states for two dimensions (2D) or surface states for three dimensions (3D).[20] Progression in the field of spintronics continues to grow at a rapid pace and it is highly dependent on the discovery, exploration, and engineering of novel materials. Indeed, spintronics promises to show significant influence in the world of science and technology. [21] In this chapter, I will highlight some spin transport phenomena concepts and mechanisms which are experimentally studied and verified throughout this thesis for magnetic insulators/normal metals heterostructures.

1.2.2. Spin Hall Effect and Inverse Spin Hall Effect

Historically, in 1971, a brilliant theoretical prediction was made by M. I. D'yakanov & V. I. Perel in which they proposed that the electric current in semiconductor induces spin orientation near the surface of the sample [22] in a thin film yielding the first thought of the existence of spin Hall effect (SHE) [23]. Thus, SHE is the splitting of spin-up and spin- down currents along opposite edges of the sample induced by transverse electric field due to SOC. [18,19,24] Therefore, as a result, in a material with large SOC, an electric current passing through can generate a transverse pure spin current

with spin polarization normal to the plane defined by the charge and spin current. On the experimental front, it was observed in 2004 through optical detection of Kerr rotation microscopy in thin films of the semiconductors of GaAs and InGaAs imaging induced opposite spin accumulations (polarizations) at the edge of the samples. [25]

On the contrary to SHE, inverse spin Hall effect (ISHE) involves a pure spin current through a high SOC material generating a transverse charge current which can be detected electrically. These two effects correlate the charge degree of freedom and the spin degree of freedom and provide an ability to reversibly convert spin and charge currents into one another. Figure 1-2 sketch the mechanism of SHE and ISHE.[19,26]

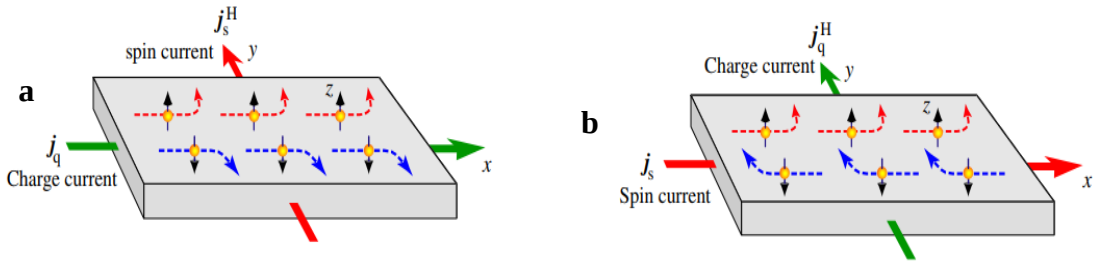

Figure 1- 2: SHE and ISHE mechanism sketches. a) SHE: charge current $\boldsymbol{J_q}$ along $\boldsymbol{x}$-direction induces the spin current $\boldsymbol{J_s}$ in $\boldsymbol{y}$-direction with the polarization parallel to the $\boldsymbol{z}$ -direction. b) ISHE: spin current $\boldsymbol{J_s}$ along $\boldsymbol{x}$- direction induces the charge current $\boldsymbol{J_q}$ in $\boldsymbol{y}$-direction with the polarization parallel to the $\boldsymbol{z}$ -direction. Adapted from Sci. Technol. Adv. Mater. 9, 014105 (2008).

Besides these effects, spin Hall angle (θ_{SH}) should be mentioned here which is the effectiveness of the spin-charge conversion and this conversion depends SOC strength.

For example, $\theta_{SH}$is large in heavy metals such as Ta, W, Ir, and Pt due to large SOC and θ_{SH} can be quantified through magneto-transport measurements.[27]

1.2.3. Anomalous Hall Effect and Quantum Anomalous Hall Effect

The anomalous Hall effect (AHE) originates from spin-orbit interaction (SOC) in ferromagnetic materials with broken time-reversal symmetry (TRS) as they have spontaneous magnetization. First, in ordinary (normal) Hall effect (OHE), placing a normal (nonmagnetic) conductor with charge current flow (*x*-direction) in a magnetic field (*z*-direction), charge carriers, as a result, are deflected to one edge of the conductor due to Lorentz force creating a voltage drop across the sample in the transverse direction (*y*-direction).[28] However, in the case of ferromagnetic materials, the Hall resistivity has the form of $\rho_{xy} = R_0 H_z + R_s M_z$ with the second anomalous term representing (ρ_{AH}) which is proportional to the magnetization of the ferromagnets, where R_s is the anomalous Hall coefficient (material-dependent) and M_z is the magnetization averaged over the sample.[29] Figure 1-3 (a, b) shows the sketch of OHE and AHE mechanism. Therefore, the electrical measurements of the Hall resistivity (ρ_{xy}) consists of both OHE as a linear background and AHE, after subtracting the linear background AHE contribution is obvious as a hysteretic loop resembling the magnetization behavior of magnetic materials.

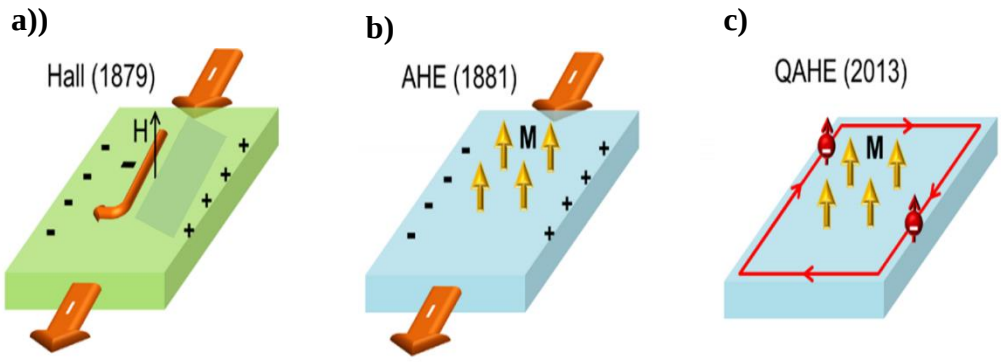

Figure 1- 3: Three different versions of Hall effects. (a) Ordinary Hall effect discovered in 1879. (b) Anomalous Hall effect (AHE) discovered in 1881. (c) Quantum Anomalous Hall effect (QAHE) discovered in 2013. Adapted from J Phys-Condens Mat 28, 123002 (2016).

As an origin of this AHE, theoretical and experimental studies on different ferromagnets have revealed three mechanisms, namely intrinsic deflection related to band structure effect and the non-zero Berry curvature, or extrinsic of side jump and skew scattering. We can distinguish between these mechanism through different power law relation of $\rho_{AHE} \sim \rho_{xx}^{\beta}$ where is β power law coefficient. For intrinsic and side jump, $\rho_{AHE} \sim \rho_{xx}^{2}$ with (β = 2) whereas for skew scattering, $\rho_{AHE} \sim \rho_{xx}$ with β = 1. [28, 29]

On the other hand, it is predicated to realize the quantized state of AHE as the last member of the Hall family and to exhibit quantized Hall conductivity ($\sigma_{yx} = \frac{e^2}{\hbar}$) without any external magnetic field.[30,31] Quantum anomalous Hall effect (QAHE) is predicted to possess spin-polarized chiral edge channels which carry current without dissipation at a zero-magnetic field. This dissipationless current is an exciting property in terms of

technological perspective. To realize QAHE, two requirements should be satisfied. First one is breaking time-reversal symmetry (TRS) through magnetic order by either magnetic doping or induced-ferromagnetism such as magnetic proximity effect. Second one is nontrivial band gap inversion in the entire Brillouin zone so that the bulk is insulating and only the surface (or the edge) is metallic with strong SOC. It is recently observed experimentally in thin film Cr and V- doped $(Bi,Sb)_2Te_3$, known as 3D magnetic topological insulators, at extremely low temperature (T~ order of 10 mK) where Hall resistance reaches the predicted quantized Hall plateau value of $(\frac{e^2}{\hbar})$ and accompanies with considerable drop in the longitudinal resistance.[32] Up to now, very low temperature of realization of QAHE hinders realistic low power consumption applications in spintronics devices.

1.2.4. Spin Caloritronics

Spin caloritronics focuses on the interaction of spin and heat currents transport in (mostly) magnetic structures and devices. From there, thermal spin currents can be actively generated, manipulated, and detected through various processes such as, ordinary Seebeck, Peltier and spin Seebeck. Spin caloritronics only emerged after the discovery of the spin Seebeck effect (SSE) in 2008 by Uchida *et al.* in ferromagnetic metal $Ni_{81}Fe_{19}$,[33] and later in 2010 for both, in ferromagnetic semiconductor GaMnAs in a low temperature regime and finally in magnetic insulators such as $Y_3Fe_5O_{12}$ (YIG) and LaY2Fe5O12 (La:YIG) proving that SSE is a universal phenomenon in magnetic materials.[34] It is

important in this context to emphasize and distinguish the difference between the conventional Seebeck effect and the SSE, normal Seebeck is an electric voltage along a temperature gradient and requires mobile charge carriers which exist only in metal and semiconductors. SSE, on the other hand, stands for the generation of spin voltage as a result of spin current; a flow of spin angular momentum perpendicular to a temperature gradient and therefore SSE is associated with magnetization dynamics.[35]

SSE is a two-step process occurring at the interface between ferromagnets (FM) and heavy metal (HM). First step is the thermal spin transport to generate a pure spin current as a result of temperature gradient ∇T. the second step is ISHE process in which spin current is injected across the interface into the HM which has sufficiently strong spin-orbit coupling to convert that into a charge current as can be seen in figure 1-4, (c). The magnitude of the SSE is quantified as the SSE coefficient $S_{SSE} = \frac{V_{thermal}}{L(\frac{\Delta T}{d})}$ where $V_{thermal}$ is the measured ISHE voltage, ΔT is the temperature difference between the two surfaces of the sample, d is the thickness of the whole sample where L is the distance between the voltage leads. ISHE voltage = $\frac{2\,|e|\rho\theta_H}{\hbar}(J_s \times \sigma)$ where J_s is spin current, σ is the spin polarization, θ_H is the spin Hall angle of HM and ρ is the electric resistivity of HM.[36]

The observation of the SSE has been shown in two different configurations; transverse and longitudinal. The original discovery of SSE was in transverse geometry in which the spin current flowing is perpendicular to the temperature gradient (clear setup is

in figure 1-4, (a)). In this geometry, the spin current measurements have some controversy because of complications with analyzing the results due to $\nabla_x T$ being in-plane. Thus, there is overwhelming heat conduction through the substrate occurring $\nabla_z T$ component which gives rise to anomalous Nernst effect (ANE) and consequently the voltage measured is not entirely or even mainly due to SSE ($\nabla_x T$) but there is a significant contribution of ANE ($\nabla_z T$). These two quantities of SSE and ANE voltages are additive, entangled and insperabale[37]. Another setup of SSE is longitudinal geometry (LSSE) and spin current flow is parallel to the temperature gradient(sketch setup is in figure 1-4, (b).[38] The geometry, in this case, is straightforward and less complicated for magnetic insulators as demonstrated in YIG/Pt bilayer system in 2010. Otherwise, if the magnetic materials are conductive, ANE of the magnetic materials dominate in in this configuration and then the SSE data are difficult to be separated out.

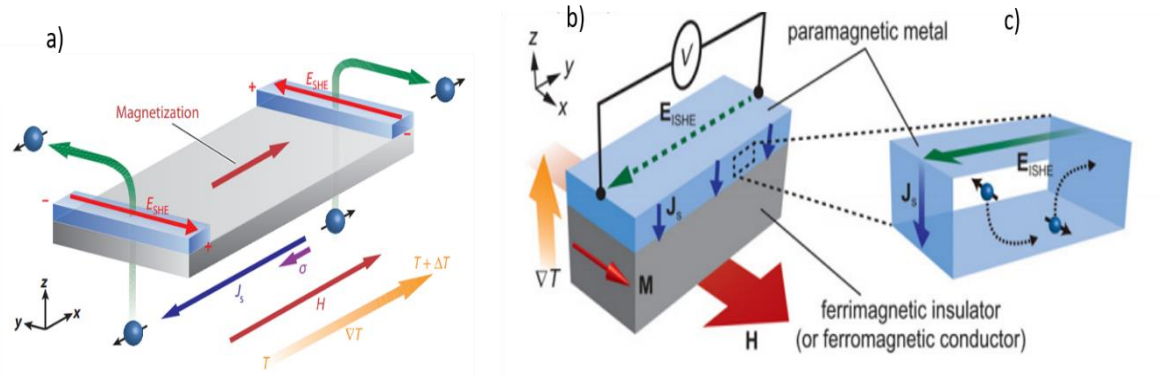

Figure 1- 4: Two schematic illustrations of SSE configurations and the inverse spin Hall mechanism. a) First experiment to demonstrate SSE in $Ni_{81}Fe_{19}$ in transverse configuration. b) Longitudinal spin Seebeck effect (LSSE). c) Schematic illustration of inverse spin Hall effect (ISHE). Here E_{ISHE} denote the electric field converted from spin current. ∇T, H, M, J_s and σ denote the temperature gradient, magnetic field (with magnitude H), magnetization vector, and spatial direction of the thermally generated spin current, the spin polarization vector of the spin current, lies along the magnetization axis respectively. Adapted from Nature 455, 778-781 (2008) and J. Phys.: Condens. Matter 26, 343202 (2014).

Research in spin caloritronics appears to be quite promising in future energy efficient technologies since it enables a simple and versatile generation of spin current and therefore electric current via ISHE from heat. Also, LSSE has simple structures that can be fabricated easily and therefore it is a promising technique for thermoelectric conversion applications.

1.2.5. Spin Dynamics

The classical description of magnetization dynamics is given by the Landau-Lifshitz-Gilbert (LLG) equation of motion which defines the time evolution of magnetization *M (r,t)* as [39]

$$\frac{\partial M}{\partial t} = -\gamma M \times H_{eff} + \alpha M \times \frac{\partial M}{\partial t}$$

where γ is the gyromagnetic ratio, α is the dimensionless Gilbert damping constant, H_{eff} is the effective magnetic field. The first term in the equation describes the steady-state precession of the local magnetization *M (r,t)* around the effective field H_{eff}, and the second term describes the magnetization relaxation where the magnetization vector relaxes to the direction of the effective field. γ defines as the ratio of magnetization per spin ($\frac{g\mu_B}{\hbar}$), and $H_{eff} = H_{ext} + H_K + H_{demag}$ where H_{ext} is external, H_K is anisotropy, and H_{demag} is demagnetization fields. In figure 1-5, the spin undergoes a spiral precession motion inwards along the trajectory ending up be aligned with effective field (H_{eff}) to minimize the energy. This precession motion should be relaxed to the energy

minimized state and this process is known as spin relaxation of magnetization which is described by the second term in the above LLG equation as the Gilbert damping term with the Gilbert damping coefficient α.[41]

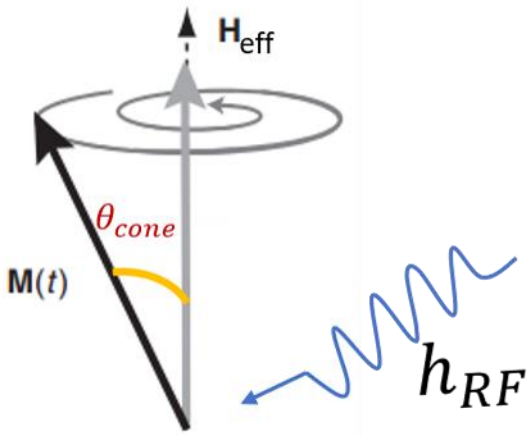

Figure 1- 5: Illustration of spin precession and decaying due to damping around the effective field (H_{eff}). Upon magnetic excitation using a radio-frequency (RF), magnetization vector M(t) spirals inward along precession trajectory and eventually point collinear with H_{eff}.

To characterize magnetization dynamics of magnetic materials, ferromagnetic resonance (FMR) technique is carried out using such as microwave cavities which have single resonance frequency, broadband with either stripline or coplanar waveguide (CPW) with ability of applying different radio- frequencies (RF) as can be seen in figure 1-6, (a). CPW role is to transmit efficiently a microwave signal from a RF source over a different range of frequencies. In such experiments, ac magnetic field is generated by RF source and perpendicular to the applied dc magnetic field with sample face down to

maximize coupling with CPW and improve signal-to noise ratio. Applied magnetic field is usually swept at a fixed RF frequency and when the resonance condition is fulfilled, the magnetization will start to precess by absorbing RF power. With AC modulation field, transmitted derivative is measured by RF diode and lock-in detection to amplify the signals. Resonance spectra contain the line position (resonance field H_{FMR},), linewidth (ΔH) which defines as peak-to-peak linewidth to determine the anisotropy H_{eff} , γ, and anisotropy from angular dependence of H_{FMR}. Gilbert damping (magnetic relaxation) plays a key role in the spin dynamics of magnetic systems and is determined from frequency dependence of the FMR spectrum linewidth. Damping characterization can be obtained in magnetic materials both metals and insulators. On the other hand, to detect spin dynamics parameters electrically in magnetic insulators where conduction electrons freeze, we often add a thin HM layer with strong SOC and this method is called FMR spin pumping.

The process of spin pumping in an FM/HM bilayer is clearly visualized in figure 1-6, (b) where the FM is resonantly excited allowing magnetization to precess under RF magnetic field (H_{RF}) with sweeping a DC magnetic field. This precession transfers spin angular momentum to the HM at the interface, generating a spin current J_s flowing into the conduction electrons in the HM layer, which is converted into a transverse charge current J_c via the ISHE.[42] Most important is the efficiency of spin transmission at the interface which is characterized by the interfacial spin mixing conductance $g_{\uparrow\downarrow}$. The combination of spin pumping and ISHE is a powerful approach to FM magnetic

properties and spin dynamics. From spin pumping, damping parameter can be measured and the spin mixing conductance $g_{\uparrow\downarrow}$ can be calculated through this relation: [42]

$$g_{\uparrow\downarrow} = \frac{4\pi M_S t_{FM}}{g\mu_B}(\alpha_{FM/HM} - \alpha_{FM}),$$

where M_s is saturation magnetization of FM layer, t_{FM} is the thickness of the FM layer, g is the Landé g factor, μ_B is the Bohr magneton, $\alpha_{FM/HM}$ and α_{FM} are the Gilbert damping constants of the FM/HM bilayer and the FM single layer, respectively and α measurement was discussed already above.

a) b)

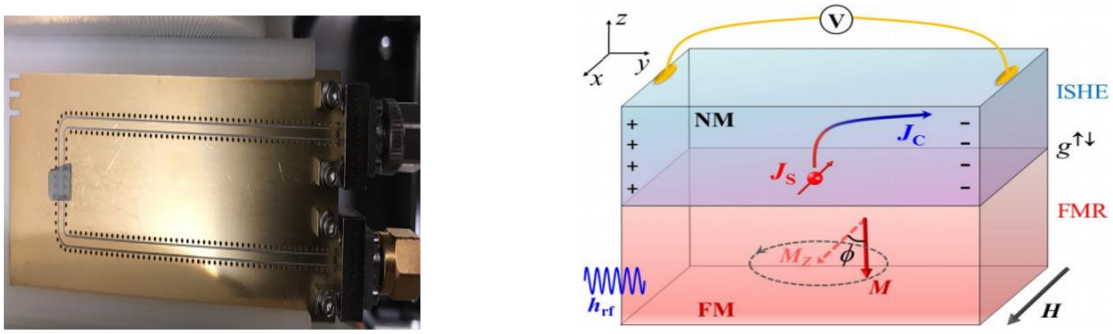

Figure 1- 6: Coplanar waveguide illustration and schematic of FMR spin pumping process in a FM/ HM bilayer. a) coplanar waveguide diagram with two connections, one is for RF source and the another one is connected to lock-in amplifier. b) Schematic of FMR spin pumping diagram where magnetization precesses in FM layer with a cone angle (ϕ) under RF excitation and this precession transfers the spin angular momentum into HM where it converts to DC voltage through ISHE. (b) is adapted from J. Phys. D: Appl. Phys. 51, 253001(2018).

1.3. Thin Film and Interface Engineering

After giving a brief introduction to magnetism and spintronics, in this sub-section, I will highlight the importance of magnetic thin films research which is the basis of modern magnetic sensors and memory elements. A unique property of these thin films is that the lateral dimensions (*x*-*y* direction) are much larger than the perpendicular dimension (*z*-direction). Matter behaves differently when the dimensions are down in nanoworld, from 1 nm up to 100 nm. Just as thin films of other materials, magnetic thin films can be deposited, and their properties can be controlled on the level of individual atomic layers, allowing artificial layers to be created with properties that are not found in nature.

Thus, in general, some intrinsic properties may differ in magnetic thin films from the bulk such as Curie temperature, anisotropy, magnetostriction and magnetic properties. Some special properties can be modified by controlling the surface, interface, atomic doping, and strain induced by the substrate. For example, interface effects can influence magnetic properties of these thin films such as spin-dependent scattering and exchange bias. In novel heterostructures constructed with magnetic insulator thin films and adjacent thin layer of heavy metal with strong SOC, the exchange interaction is expected to spin polarize the electronic states and modify band structure leading to exotic spin phenomena. Chapters two and three of this thesis contain thin film and heterostructure of garnet magnetic insulators and their interfaces. These magnetic thin films are commonly prepared by one or a combination of several following deposition methods: pulsed laser

deposition, molecular beam epitaxy, sputtering, and e-beam evaporation. During thin film deposition, the target of a chosen material is put away by certain distance from the substrate and then thin film is deposited on the substrate which may be heated to high temperature to promote the mobility of atoms arriving on the surface forming layers of thin films. Substrates quality and crystallinity (single, polycrystalline or amorphous) are very critical in thin films growth and they are chosen based on required and designed properties. An example of thin films growth is the epitaxial (means lattice registry is continuous above the interface without any strain, atomic-scale dislocations or relaxation) single crystal film growth method which gives rise to high thin film quality with desired structural and magnetic properties. Furthermore, thin-film heterostructures of dissimilar materials are needed to investigate new magnetic properties and magnetic coupling between the two layers.

References:

1. Stern and Gerlach: How a Bad Cigar Helped Reorient Atomic Physics. *Physics Today* **56**, 53-59 (2003).

2. Uhlenbeck, G.E. & Goudsmit, S. Spinning Electrons and the Structure of Spectra. *Nature* **117**, 264 (1926).

3. Coey, J.M.D. Magnetism and Magnetic Materials (Cambridge University Press, Cambridge, 2010).

4. Jean-Pau, E.B.H.B.F.S.K. Magnetism and Synchrotron Radiation Approach (ed. 1) (Springer Verlag, Berlin, Heidelberg, , New York, 2010), 2006).

5. Chikazumi, S. Physics of Ferromagnetism (Oxford University Press, Oxford, United Kingdom, 1997).

6. Witczak-Krempa, W., Chen, G., Kim, Y.B. & Balents, L. Correlated Quantum Phenomena in the Strong Spin-Orbit Regime. *Annual Review of Condensed Matter Physics* **5**, 57-82 (2014).

7. Shanavas, K.V., Popović, Z.S. & Satpathy, S. Theoretical model for Rashba spin-orbit interaction in d electrons. *Physical Review B* **90**, 165108 (2014).

8. Hellman, F. et al. Interface-induced phenomena in magnetism. *Reviews of Modern Physics* **89**, 025006 (2017).

9. O'Handley, R.C. Modern Magnetic Materials: Principles and Applications (Wiley-Interscience, 1999).

10. Johnson, M.T., Bloemen, P. J. H., den Broeder, F. J. A. & de Vries, J. J.. Magnetic anisotropy in metallic multilayers. *Rep. Prog. Phys* **59** (1996).

11. Sander, D. The magnetic anisotropy and spin reorientation of nanostructures and nanoscale films. *J. Phys.: Condens. Matter.* **16** (2004).

12. Hoffmann, A. & Bader, S.D. Opportunities at the Frontiers of Spintronics. *Physical Review Applied* **4**, 047001 (2015).

13. Pulizzi, F. Spintronics. *Nature Materials* **11**, 367 (2012).

13. Sinova, J. & Žutić, I. New moves of the spintronics tango. *Nature Materials* **11**, 368 (2012).

14. Bader, S.D. & Parkin, S.S.P. Spintronics. *Annual Review of Condensed Matter Physics* **1**, 71-88 (2010).

15. Lu, J.W., Chen, E., Kabir, M., Stan, M.R. & Wolf, S.A. Spintronics technology: past, present and future. *International Materials Reviews* **61**, 456-472 (2016).

16. Wolf, S.A., Chtchelkanova, A.Y. & Treger, D.M. Spintronics—A retrospective and perspective. *IBM Journal of Research and Development* **50**, 101-110 (2006).

17. Žutić, I., Fabian, J. & Das Sarma, S. Spintronics: Fundamentals and applications. *Reviews of Modern Physics* **76**, 323-410 (2004).

18. Saburo, T. & Sadamichi, M. Spin current, spin accumulation and spin Hall effect. *Science and Technology of Advanced Materials* **9**, 014105 (2008).

19. Pesin, D. & MacDonald, A.H. Spintronics and pseudospintronics in graphene and topological insulators. *Nature Materials* **11**, 409 (2012).

20. Chappert, C., Fert, A. & Van Dau, F.N. The emergence of spin electronics in data storage. *Nature Materials* **6**, 813 (2007).

21. Dyakonov, M.I. & Perel, V.I. Current-induced spin orientation of electrons in semiconductors. *Physics Letters A* **35**, 459-460 (1971).

22. Hirsch, J.E. Spin Hall Effect. *Physical Review Letters* **83**, 1834-1837 (1999).

23. Wang, X.-g. et al. Conversion of electronic to magnonic spin current at a heavy-metal magnetic-insulator interface. *Physical Review B* **95**, 020414 (2017).

24. Kato, Y.K., Myers, R.C., Gossard, A.C. & Awschalom, D.D. Observation of the Spin Hall Effect in Semiconductors. *Science* **306**, 1910-1913 (2004).

25. Valenzuela, S.O. & Tinkham, M. Direct electronic measurement of the spin Hall effect. *Nature* **442**, 176 (2006).

26. Mosendz, O. et al. Quantifying Spin Hall Angles from Spin Pumping: Experiments and Theory. *Physical Review Letters* **104**, 046601 (2010).

28. Yue, D. & Jin, X. Towards a Better Understanding of the Anomalous Hall Effect. *Journal of the Physical Society of Japan* **86**, 011006 (2016).

29. Nagaosa, N., Sinova, J., Onoda, S., MacDonald, A.H. & Ong, N.P. Anomalous Hall effect. *Reviews of Modern Physics* **82**, 1539-1592 (2010).

30. He, K., Wang, Y. & Xue, Q.-K. Quantum anomalous Hall effect. *National Science Review* **1**, 38-48 (2014).

31. Xue, Q., He, K. & Wang, Y. in 2016 IEEE 29th International Conference on Micro Electro Mechanical Systems (MEMS) 1-1 (2016).

32. Chang, C.-Z. et al. Experimental Observation of the Quantum Anomalous Hall Effect in a Magnetic Topological Insulator. *Science* **340**, 167-170 (2013).

33. Uchida, K. et al. Observation of the spin Seebeck effect. *Nature* **455**, 778 (2008).

34. Uchida, K. et al. Spin Seebeck insulator. *Nature Materials* **9**, 894 (2010).

35. Bauer, G.E.W., Saitoh, E. & van Wees, B.J. Spin caloritronics. *Nature Materials* **11**, 391 (2012).

36. Tikhonov, K.S., Sinova, J. & Finkel'stein, A.M. Spectral non-uniform temperature and non-local heat transfer in the spin Seebeck effect. *Nature Communications* **4**, 1945 (2013).

37. Qu, D., Huang, S.Y., Hu, J., Wu, R. & Chien, C.L. Intrinsic Spin Seebeck Effect in Au/YIG. *Physical Review Letters* **110**, 067206 (2013).

38. Uchida, K. et al. Longitudinal spin Seebeck effect: from fundamentals to applications. *Journal of Physics: Condensed Matter* **26**, 343202 (2014).

39. Mondal, R., Berritta, M. & Oppeneer, P.M. Relativistic theory of spin relaxation mechanisms in the Landau-Lifshitz-Gilbert equation of spin dynamics. *Physical Review B* **94**, 144419 (2016).

40. Scheck, C., Cheng, L., Barsukov, I., Frait, Z. & Bailey, W.E. Low Relaxation Rate in Epitaxial Vanadium-Doped Ultrathin Iron Films. *Physical Review Letters* **98**, 117601 (2007).

41. Hickey, M.C. & Moodera, J.S. Origin of Intrinsic Gilbert Damping. *Physical Review Letters* **102**, 137601 (2009).

42. Fengyuan, Y. & Hammel, P.C. FMR-driven spin pumping in Y 3 Fe 5 O 12 -based structures. *Journal of Physics D: Applied Physics* **51**, 253001 (2018).

Chapter 2

In-Depth Growth Development of Yttrium Iron Garnet ($Y_3Fe_5O_{12}$ or YIG) Thin Films

2.1 Introduction to Rare Earth Iron Garnets

As magnetic insulators, rare earth iron garnets ($R_3Fe_5O_{12}$) or (REIG) are prototype candidates in nanoscale spintronics research[1], particularly in novel spin transport phenomena such as induced ferromagnetism in adjacent non-magnetic thin layer through magnetic proximity effect (MPE)[2,3] , thermal generation of pure spin current known as spin Seebeck effect[4], and magnon spin dynamics[5,6,7,8], etc. To list here their unique properties: electrical insulators with large band gap [9] (~ 2.85 eV), high Curie temperature (~550 K), and high stability under the ambient environments. Therefore, as spintronics exploits extensively electron spin, REIG has many distinctive advantages. First, generation of pure spin current in different ways either thermally, resonantly or electrically[10] without a company of charge current or Joule heating dissipation. Secondly, magnon spin current in REIG propagates much longer distance[11] (many microns). Unlike ferromagnetic metals in which charge current drives spin-polarized electrons to generate spin current with a company of Joule heating and Gilbert damping is very large due to conduction-electron dominance near the Fermi level [12].

Nowadays, these complex oxide materials (REIG) based heterostructures in thin film form attract a lot of attention of researchers to discover interesting and useful

functional properties in spintronics[13]. In REIG- based heterostructure, attached thin layer of HM with strong SOC to gives rise to emerging new phenomena such as induced ferromagnetism by MPE, causing peculiar magnetoresistance[14], and quantum anomalous Hall effect in Dirac fermion systems. More importantly to mention is the effect of interface quality such as roughness on the exchange interaction across the interfaces.

In this chapter, I will begin with a description of garnet structure with a focus on YIG. Then, I will introduce state-of-the-art epitaxial growth of YIG films through layer-by-layer growth mode on GGG (110) orientation with engineering atomically flat terraces, and magnetic and structural property characterizations. Additionally, these growth conditions can be modified in order to meet the needs for different projects. For example, it is possible to obtain high-quality growth of YIG on GGG at room temperature followed by annealing in furnace to crystalline YIG. After description of YIG grown on GGG, I will present a complete study on the growth YIG on a compressively strained substrate ($Y_3Al_5O_{12}$ or YAG). At the end, I will discuss YIG thin films grown on amorphous Si/SiO_2 and their structural and magnetic properties. Single crystal growth of topological insulators (TI) on polycrystalline YIG will also be briefly discussed.

2.2 Rare Earth Iron Garnet Structure Overview

Chemical formula of garnet structure is $\{A_3^{3+}\}[B_2^{3+}](B_3^{3+})O_{12}$ where two sites here are occupied with the same cation ***B***. ***A*** and ***B*** cations are surrounded by different oxygen polyhedral.[15] The garnet structure has giant cubic unit cell with 160 atoms and belongs to space group *Ia3d* with eight formula unit per unit cell. For rare earth iron garnet (REIG), it becomes $\{R_3^{3+}\}[F_2^{3+}](Fe_3^{3+})O_{12}$ where R_3^{3+} occupies *24* dodecahedral (*c*) sites which are coordinated to eight oxygen ions, F_2^{3+} is at *16* octahedral (*a*) sites with coordination of to six oxygen ions and Fe_3^{3+} is at 24 tetrahedral (*d*) sites with coordination of to four oxygen ions as seen in figure 2-1, (b)[13,15]. Thus, each oxygen ion is coordinated by one (*a*) site of F_2^{3+}, one (*d*) site Fe_3^{3+} and two (*c*) sites of R_3^{3+} as seen in figure 2-1, (b). Coupling these ions to each other is by oxygen ions mediation through super- exchange interaction; between two of Fe^{3+} ions at *(a)* site and three of Fe^{3+} ions at *(d)* showing that they couple antiferromagnetically and the net magnetic moment becomes one Fe^{3+} ion per formula unit. With respect to rare earth ions at *(c)* sites, they are weakly exchange coupled ferromagnetically to the Fe^{3+} at *(a)* sites and antiferromagnetically to Fe^{3+} ions at *(d)* sites. According to Neel theory, the magnitude of super-exchange interaction depends strongly on the angle between *magnetic ion-oxygen ion-magnetic ion* bond with largest interaction at 180° and weakest at 90°. If the magnetization of Fe^{3+} at *(a)* sites and rare earth elements at *(c)* is the same as for the opposing magnetization of Fe^{3+} at *(d)* sites, then the total magnetization vanishes, and compensation occurs.[16]

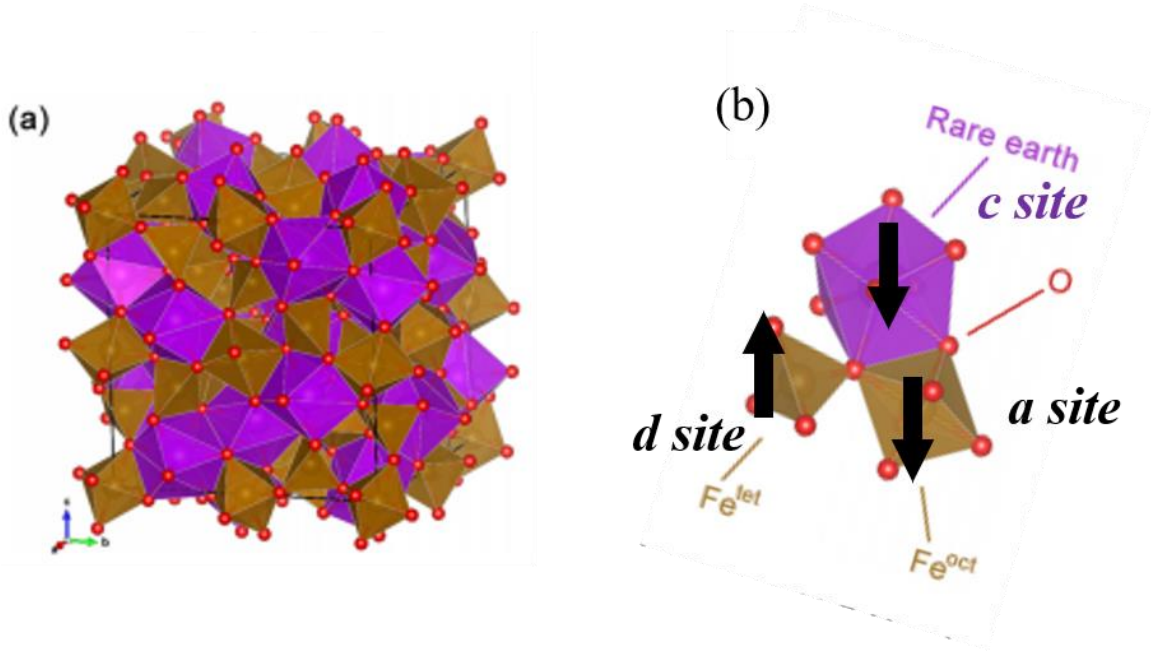

Figure 2- 1: The schematic draw of crystal structure of rare earth iron garnet (REIG) unit cell. a) Cubic unit cell. b) The Fe^{3+} ions occupy the tetrahedral and octahedral sites whereas the rare earth elements occupy the dodecahedral site. Adapted from Phys. Rev. B **95**, 024434 (2017).

2.3 State-of-Art Growth of YIG Films

Yttrium iron garnet ($Y_3Fe_5O_{12}$ or YIG) is a complex magnetic oxide insulator and prominent member of rare earth iron garnet family which has attracted the most attention in magnetic insulator-based spintronics for its extremely low damping [17] (~3×10^{-5}). Similar to other REIGs, YIG is not a ferromagnet, but ferrimagnet in which Y^{3+} ions are diamagnetic without any permanent magnetic moment and therefore the magnetization originates from sublattices of three Fe^{3+} ions in *(d)* sites and two Fe^{3+} ions in *(a)* site which are coupled antiferromagnetically through super-exchange interaction mediated by

oxygen ions. Compared with other magnetic insulators such as EuS (~18 K) and EuO (~ 69 K) which are ferromagnets, YIG has a high Curie temperature (~550 K) and a large band gap (~2.85 eV); therefore, it is an excellent room-temperature pure spin current source for spin Seebeck effect and spin pumping. With respect to YIG structure, it is the same as in other garnets and already discussed on the previous page. Based on spin structure, YIG magnetization comes from the net magnetic moment of one spin Fe^{3+} ion from *(d)* sites with a magnitude of $5\ \mu_B$ in principle per formula unit at 0 K.[18] The theoretical saturation magnetization ($4\pi M_s$) is 2470 G at 0 K and reported range from 1780 to 1730 G at room temperature.[16]

2.3.1 Layer-by-Layer Epitaxial Growth

Here, unlike in bulk crystal applications, performance of thin film devices in spintronics heavily rely on interactions across the interface; therefore, the surface and interface properties (e.g. morphology and magnetism) are extremely important. Several growth techniques are used for this study, including pulsed laser deposition (PLD) which is a common technique for nanometer-thick oxide thin film growth and recently RF sputtering. For micron-thick YIG, liquid phase epitaxy (LPE) is the technique of choice. As all REIG materials have been grown by PLD in this study, brief information about the homemade PLD system and growth procedure will be first introduced.

The physical process of the laser-target interaction can be divided into four phases; a) plasma plume creation from the target upon the laser ablation, b) dynamic evolution afterwards, c) plume carried particles and atoms be deposited on the hot substrate, d) how does the formation of these atoms sit over the substrate.[19] Therefore, in details, our home made PLD system as shown in figure 2-2, (b) includes two main parts; the laser and ultrahigh vacuum (UHV). The laser type is KrF coherent excimer laser (model: Coherent COMPexPro 102F) which is ultraviolet light with wavelength (λ= 248 nm) and used as source ablation. The repetition rate can be adjusted from 1 to 20 Hz and maximum laser power is 400 mJ/Pulse giving energy density of ~ 2J/cm^2. The second part of PLD system is UHV chamber as pictured in figure 2-2, (c) with base pressure of 4×10^{-7} Torr which includes leak valve to tune ambient pressure of ozone and materials targets as depicted in figure 2-2, (d) and the reflection high-energy electron diffraction (RHEED) to monitor growth mood and thickness.[20]

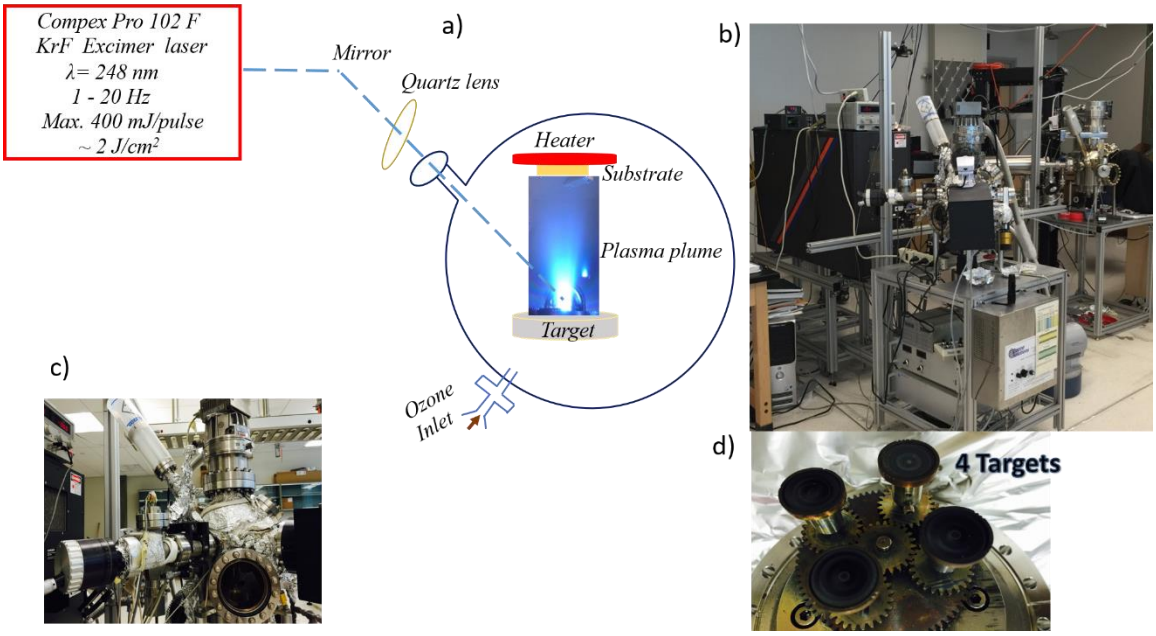

Figure 2- 2: The schematic draw of pulsed laser deposition system (PLD) parts, process and picture of two homemade PLDs in Prof. Shi lab. a) The schematic parts and mechanism of how PLD works with information about the excimer laser. b) The real picture of two homemade PLD systems in Prof. Shi lab. c) Zoom view of the main UHV chamber. d) Zoom view of the four real targets inside the chamber.

The growth of thin films as described in figure 2-2, (a) takes place in the following steps; the laser light focused with high energy density through quartz lens directly into the target to hit and then absorbed by the target. As consequence, plasma plume is created by ejecting ions, atoms, molecules and particles travelling towards the hot substrate in either vacuum or gas ambient. Once they reach the substrate, they diffuse over based on the thermal equilibrium forming the nice and thin layers. Different materials need different recipe of optimized growth conditions and parameters and in this thesis, these parameters will be optimized to obtain state of art growth quality to match

exactly the right chemical stoichiometry of the material with ultra-flat and smooth surface as required to investigate some transports of spin phenomena.

Highly densified YIG target was prepared by purchasing YIG powder (stoichiometric ≥99.9%) from Alfa Aesar and then it is either densified via the current activated pressure assisted densification (CAPAD) processing technique[21] at 950 °C with an applied load of 100 MPa for 5 mins. Or it is synthesized manually by pressed into pellets and sintered at 1200 °C for 72 hours in oxygen. The final relative density of the target from both methods is over 85%, and the crystal structure of YIG target is confirmed by x-ray diffraction. In sub-sections, comprehensive studies of YIG growth on different substrates and the structural and magnetic properties will be presented.

2.3.1.1 Substrate Treatment and Atomic Terrace Engineering

I focus here on gadolinium gallium garnet ($Gd_3Ga_5O_{12}$ or GGG) substrates. Other ones may be treated in the same way. GGG is very important for epitaxial growth of YIG because YIG lattice constant (a) is 12.376 Å and GGG 12.383 Å with very small lattice mismatch of 0.056 %. GGG substrates with (100), (110) or (111) orientations are commercially available from MTI. They were first cut into square shape pieces (5×5 mm^2) and then ultrasonicated in acetone bath for one hour followed sequentially by second cleaning of acetone gun, isopropyl alcohol, and DI water. After that, optical microscopy is used to check if they are clean or not and if not, the same cleaning procedures are repeated. Then, they are annealed in ambient oxygen gas inside a furnace

for specific temperature and time and this step will be to be discussed below. There are two reasons of annealing these substrates: first is to make their surfaces atomically smooth and flat and second is to achieve atomic terraces to ensure the high quality of the subsequent film growth. The surface quality is very essential to obtaining high-quality growth of epitaxial film on top.[22]

A wide range of annealing temperatures (from 400 to 1300 °C) has been explored on GGG (110) to study the effect of annealing and the results are summarized in figure 2-3, (a-c). Figure 2-3, (a) shows the surface morphology of a purchased GGG substrate right after complete cleaning but without annealing. The root-mean-square (RMS) roughness is 0.51 nm. After annealed in oxygen at 1000 °C for 6 hours, atomic terraces emerge as shown in figure 2-3, (b). Similar results were previously found on annealed STO substrates.[23] In the meantime, the RMS roughness is greatly reduced down to 0.15 nm. However, when the annealing temperature is increased to 1100 °C for the same amount of time, pits and cracks appear on the entire substrate as shown in figure 2-3, (c), even though the RMS roughness is only increased slightly. Figures 2-3 (a), (b) and (c) display the dramatic effect of annealing on the GGG substrate surface morphology. Annealing temperature needs to be sufficiently high to promote atomic mobility and reduce roughness but sufficiently low to keep the stoichiometry (preventing volatilization of ions) in the film. The optimized temperature, 1000 °C is 0.63 of the melting T_m. At this temperature one would expect volume diffusion to be active. It is likely that 1100 °C (T/T_m = 0.69) causes too much long-range diffusion or volatilization. For comparison, figure 2-3, (d) is the combination of GGG surface profile after annealing in oxygen at

1000 °C for 6 hours and then growth of a 30 nm thick YIG film showing extremely smooth atomic terraces with RMS roughness 0.067 nm. Therefore, because of this substrate treatment, atomically terraced GGG (110) surface emerges, enabling the subsequent ultra-flat terraced YIG film growth with ultra-smooth atomic terraces are obtained. [20]

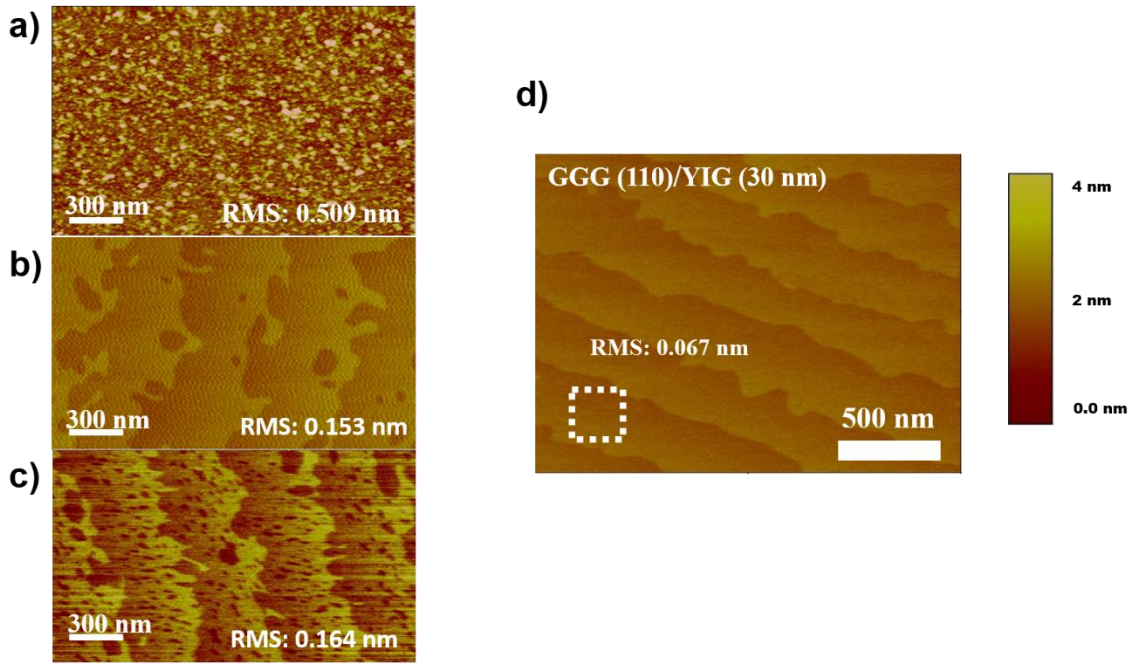

Figure 2- 3: AFM surface morphology of GGG (110) substrates after different surface treatments and YIG. a) Original purchased GGG substrates after ultra-sonicated in acetone and isopropanol for surface cleaning. b) Annealed GGG substrates at 1000 °C in O_2 environment for 6 hours. c) Annealed GGG substrates at 1100 °C in O_2 environment for 6 hours. d) AFM surface morphology of 30 nm thick YIG film on (110) GGG substrates for the area of 2μm×2μm.

Similar attempt has been carried out for GGG (100) and (111) and only atomically flatness of the surface is obtained. RMS roughness is also reduced down to 0.16 nm for (100) and 0.14 nm for (111). However, atomically terraces are not formed at any annealing temperature.

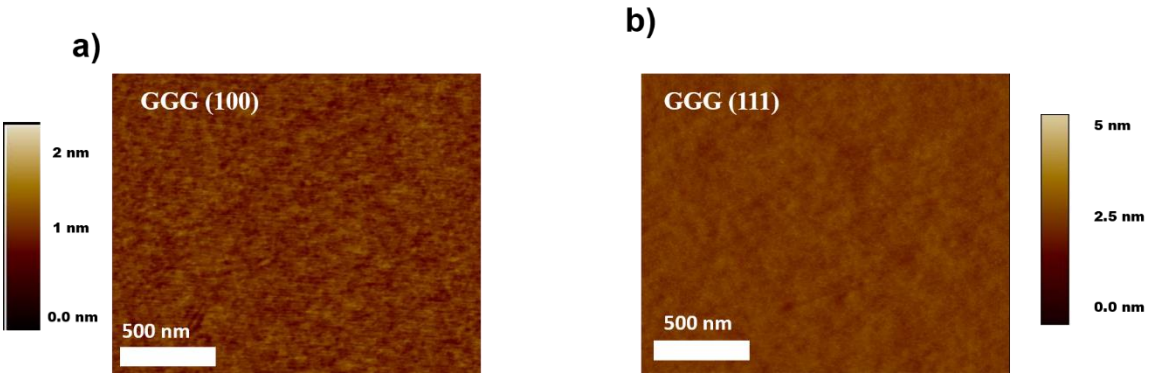

Figure 2- 4: AFM surface morphology of GGG with orientation of (100) and (111) substrates. a) AFM scan of surface profile of bare GGG (100) with RMS of 0.16 nm. b) AFM scan for GGG (111) with RMS of 0.14 nm. The area of each scan is 2μm×2μm and there is no any of atomic terraces formation for these orientations.

We have only achieved atomic terraces in GGG (110). Therefore, we need to know how these terraces grow and which crystallographic directions they grow in. We carried out the following study: five different pieces with marked substrate edge direction on each were placed in the furnace for 6 hours at 1000 $^{\circ}$C. These substrates are from different wafers, but they have the same edge directions. Then, we performed AFM imaging and track the <111> direction for all scans. The images are shown in figure 2-5. As an example, in (a), the terraces are completely parallel to <112>, whereas in (b), the terraces grow with 45° off the <111> direction. The conclusion here is that there is no specific crystallographic direction for terrace growth and the direction of the terrace growth may depend on the surface polish angle or mis-cut angle as well.

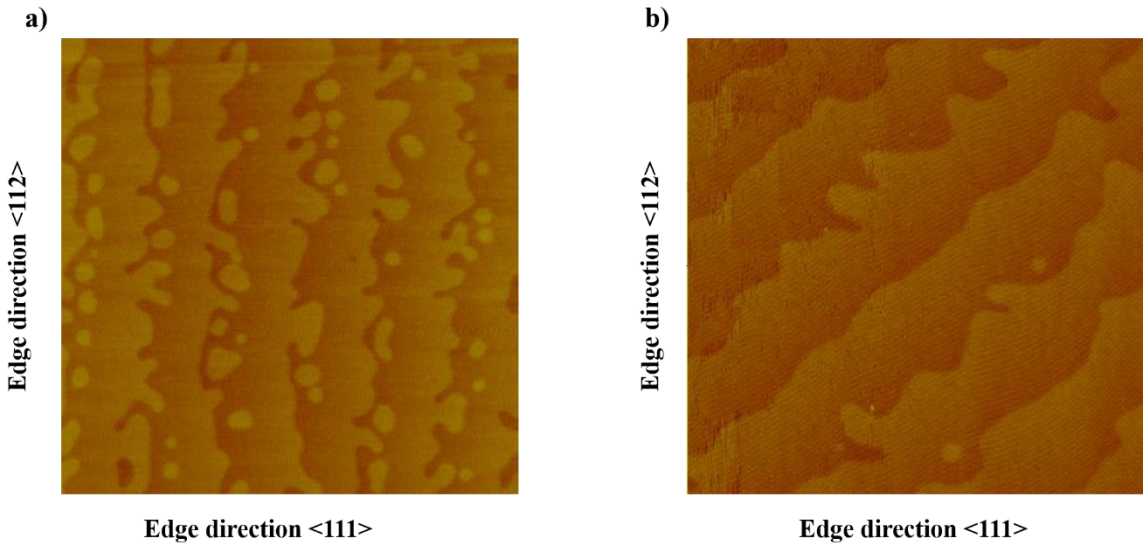

Figure 2- 5: AFM surface morphology for different two pieces of GGG with orientation of (110) to identify the crystallographic terraces formation directions. a) The AFM scan with the tip being parallel to <111> direction and terraces grow along <112>. b) AFM scan for another sample with the tip being parallel to <111> direction and terrace grow with 45° off from <111> and<112> directions.

We pay a great deal of attention to the annealing treatment of substrates because the quality of substrate surface is important for achieving layer-by-layer growth mode as will be shown in next sub-section. In addition, suitable substrate annealing cleans the particles and organic residues on the surface making the surface ultra-flat and smooth so that the subsequent REIG material grown on top will be flat. Thus, we can study the interface effect of interaction above YIG for different purposes. To increase the width of the terraces, we conducted another study on the effect of the time of annealing on terrace width. In figure 2-3, the typical width is from 150 to 300 nm and the aim is to enlarge it up to 1 μm. The motivation behind making the widest possible terraces is to achieve the strongest exchange coupling between REIG and another thin layer on the top without the effects from step edges and different terminations. For example, placing single graphene

sheet on one single atomic terrace of REIG surface could couple them with the maximum possible exchange strength. Therefore, the experiment had been carried out for 6, 12, 24, and 36 hours. Consequently, as seen in figure 2-6 from the AFM line profile of terraces, the maximum width obtained is ~ 500 nm for area of 2 µm×2 µm.

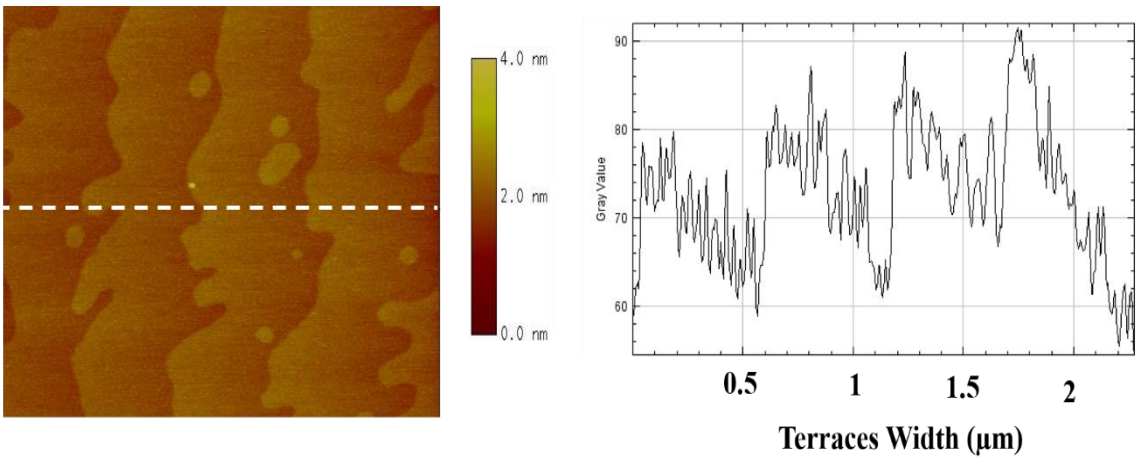

Figure 2- 6: AFM scan for GGG (110) terraces morphology after different annealing times. The terraces width is checked by line profile revealing that each terrace width is ~ 500 nm.

2.3.1.2 Layer-by-Layer Growth Monitored by RHEED Oscillations

The GGG (110) substrates are *in situ* baked with a base pressure around 5 x 10^{-7} Torr at ~200 ˚C for 5 hours. Before deposition, the substrates are then annealed at ~750 ˚C under a 1.5 mTorr oxygen pressure with 12 wt% ozone for 30 mins. During the pre-deposition annealing, the reflection high-energy electron diffraction (RHEED)[24] spots become sharper and brighter, and the intensity saturates after 30 mins annealing. Then, under the same condition of oxygen and temperature as the pre-deposition annealing, the

KrF excimer laser pulses of 248 nm in wavelength with power of 150 mJ strike the target at a repetition frequency of 1 Hz. The differentially pumped RHEED is kept on to monitor the growth of YIG layers *in situ*. As shown in figure 2-7, (a, b), RHEED intensity oscillations are observed, showing excellent layer-by-layer epitaxial growth of YIG before the termination of growth. Each oscillation has a period of 300 s, representing growth of one atomic layer along the (110) direction of the cubic cell of GGG with the lattice constant of 12.383 Å as indicated in figure 2-7, (a). Figure 2-7, (b) shows 277 continuous oscillations for the whole growth which corresponds to the film thickness of ~100 nm. The thickness is further confirmed by atomic force microscopy (AFM) and a Dektak profilometer. The layer-by-layer growth obtained with such a low repetition rate is below the threshold found in a previous report[25], and the growth rate is 0.09 nm/min for this 100 nm film. Inset in figure 2-7, (b) shows a few zoom-in RHEED oscillations out of 277 ones.[20] These oscillations are achieved in all GGG orientations (100), (110) and (111) with the same growth conditions.

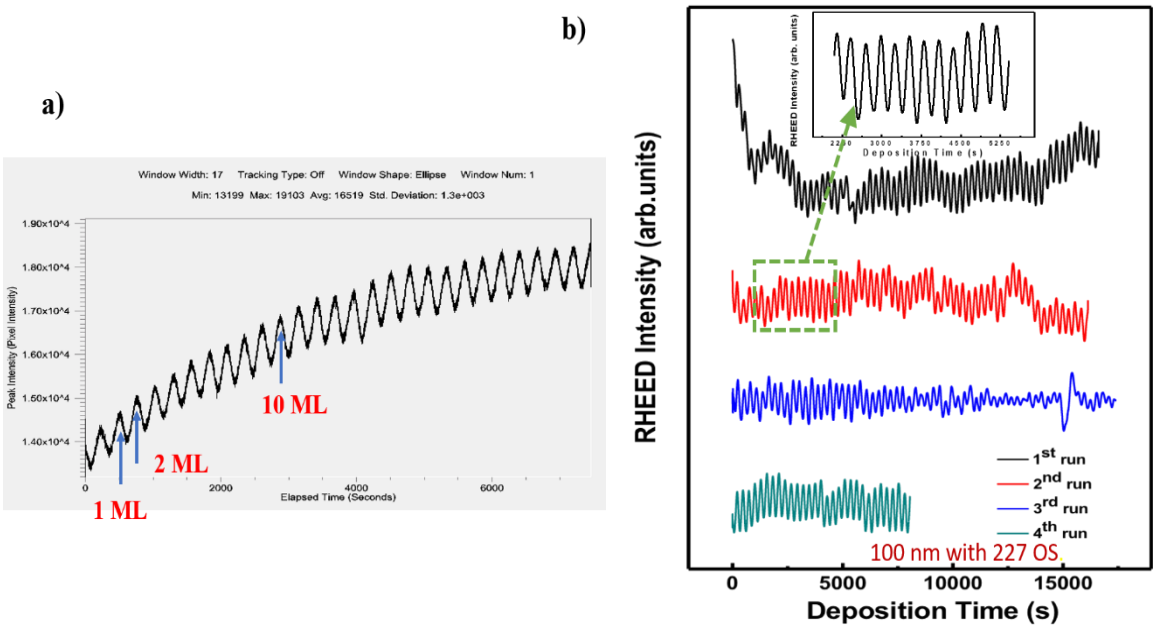

Figure 2- 7: RHEED oscillations for growth of YIG by pulsed laser deposition (PLD). a) RHEED oscillation for YIG grown layer by layer growth mood. From oscillation, each monolayer can be identified, and the thickness of the film can be calculated from the number of these oscillations. b) 227 layers (100 nm) thick YIG film of continuous layer by layer RHEED oscillations observed during the growth on (110) GGG substrate. Inset is some RHEED oscillations for a chosen time slot.

Figure 2-8, (a) is the RHEED pattern of an as-grown YIG film which shows the identical cubic crystalline structure to that of GGG with negligible lattice mismatch. The Kikuchi lines from the diffraction of diffusely scattered electrons[26] are also clearly resolved, confirming that the YIG film is of high crystallinity. Furthermore, Figure 2-8, (a) shows a transmission electron microscopy (TEM) image of the 30 nm YIG film grown on GGG (110), indicating a sharp interface with negligible mismatch between YIG and GGG. Atomically resolved YIG layers show the epitaxy, consistent with the previous RHEED results.

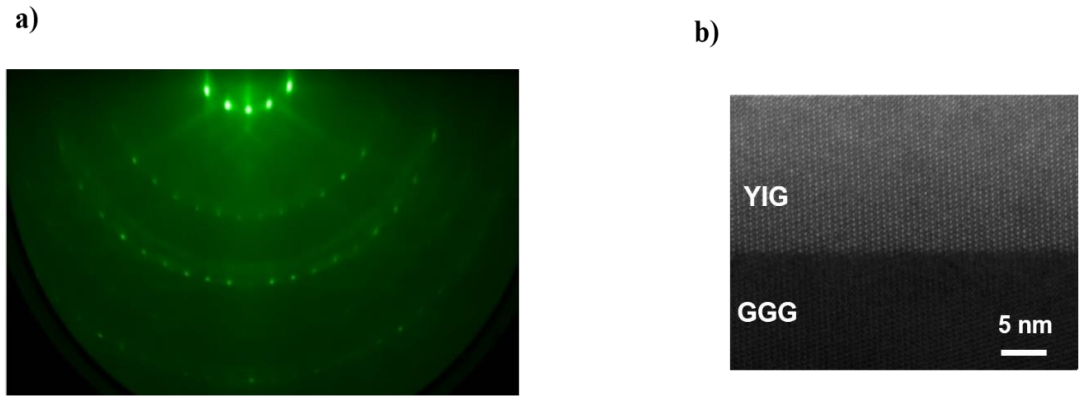

Figure 2- 8: Structure characterization of epitaxial growth of YIG on GGG (111), RHEED Pattern and TEM image. a) RHEED pattern of YIG film showing single crystalline structure of YIG after deposition. b) TEM image of 30 nm thick YIG thin film on (110) GGG substrate.

2.3.1.3 Magnetic and Damping Characterization

YIG hysteresis loops are measured using a vibrating sample magnetometer (VSM) with both out-of-plane and in-plane field orientations, as shown in figure 2-9 figure 2-9, (a) is a top view of the YIG sample marked with main crystallographic orientations. The two edges of (110)-orientated GGG substrate are confirmed to be along $[1\underline{11}]$ and $[1\underline{1}2]$. $[1\underline{1}1]$, another member of the ⟨111⟩ family, lies at an angle of 70° with respect to the $[1\underline{11}]$ *edge*. YIG films grown on GGG have the easy axis lying in the film plane shown by figure 2-9, (b), due to the dominance of shape anisotropy.[27] The saturation moment is found to be $3.5\mu_B$ per formula unit at room temperature and reaches approximately 5 μ_B at 10 K. Aside from the strong in-plane anisotropy, the (110)-oriented YIG film shows two-fold symmetry in the film plane, as indicated in figure 2-9,(c) and

(d). The azimuth angle φ is measured between the external field H and the $[1\underline{11}]$ edge. figure 2-9, (d) is the in-plane magnetic hysteresis loops for a few selected φ angles, showing an in-plane easy axis oriented at φ=30° and an in-plane hard axis along the orthogonal direction, i.e. φ=120°. The azimuth angular dependence of the coercive field is illustrated in figure 2-9, (c), showing clear in-plane uniaxial symmetry. The observed in-plane uniaxial anisotropy is obviously related to the crystalline structure of the (110)-oriented YIG film. In bulk YIG, ⟨111⟩ and ⟨1$\underline{1}$0⟩ are the easiest and hardest axes, respectively.[28] In the film plane of (110)-oriented YIG, there are two equivalent axes from the ⟨111⟩ family, and the [001] axis lies in between these two axes about 55° from each. As a consequence,[29] [001] becomes the in-plane easy axis, and $[1\underline{1}0]$, about 35° from the $[1\underline{11}]$ edge and perpendicular to $[1\underline{1}0]$, becomes the in-plane hard axis, which corresponds well to φ =30° found in experiments. The torque measurements on flux-grown magnetic garnets also exhibit similar noncubic anisotropy, which was interpreted in terms of a growth induced pair-ordering model.

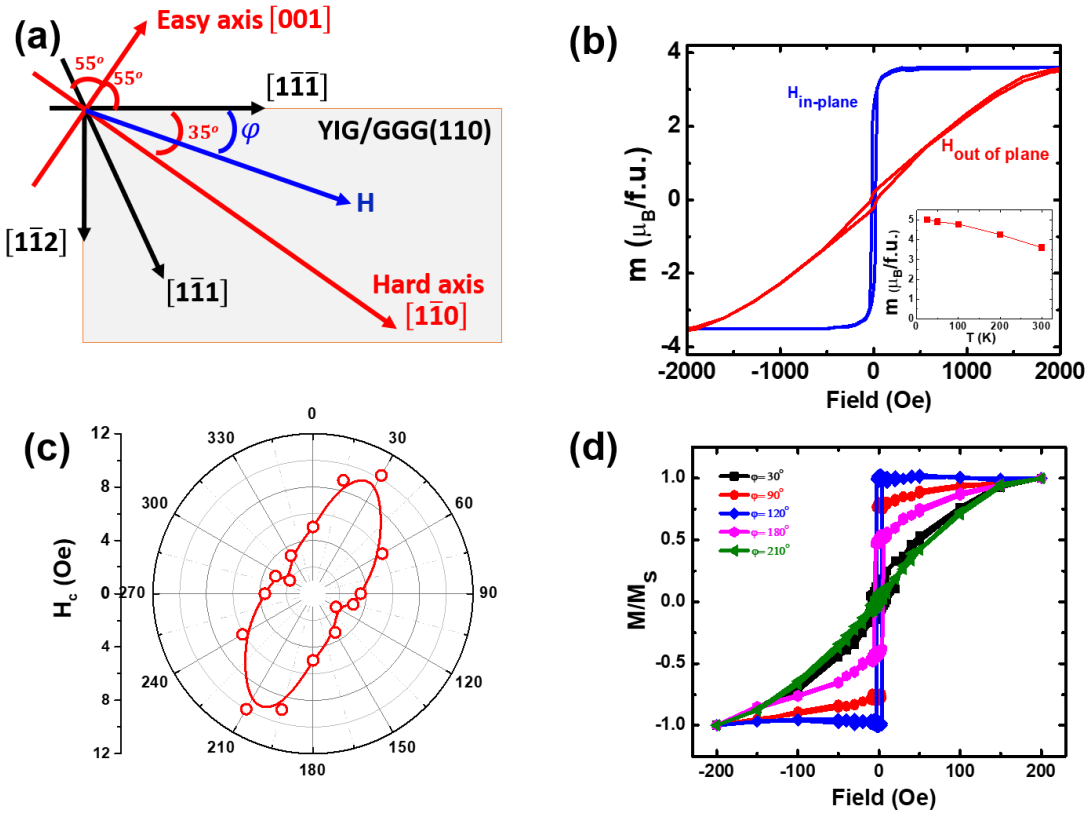

Figure 2- 9: Spontaneous magnetization characterization of 30 nm thick YIG grown on GGG (110) and determination of in-plane easy and hard axes directions. (a) Coordinate system of YIG film plane with the orientations of crystalline directions. (b) Magnetic hysteresis loop measurements of 30 nm thick YIG film on (110) GGG with field out of plane (red) and in film plane (blue) at 300K. Inset: A temperature dependence of saturation magnetization in unit of μ_B per formula unit. (c) Azimuth angle dependence of coercive field. (d) In-plane angle rotation of magnetic hysteresis loops showing in-plane two-fold symmetry of (110) oriented YIG film.

On the other hand, ferromagnetic resonance (FMR) is a powerful technique used to probe magnetization dynamics from which magnetic parameters such as saturation magnetization, magnetic anisotropy and Gilbert damping constant (α) can be extracted. It is important to mention here the magnetic properties are measured through detection of processional motion of the magnetization when it is oriented by an external static magnetic field. In this thesis, the measurements are carried out either by using FMR

cavity with single frequency (f = *9.32 GHz*) or coplanar waveguide (CPW) based broadband FMR with multi microwave frequencies. With respect to FMR cavity, the measurements are performed using a Bruker EMX EPR spectrometer on YIG films with different thicknesses. As shown in figure 2-10, (a) in the FMR, the resonance phenomenon occurs when the microwave frequency applied transversely to static magnetic field is equal to that of the magnetic moment precession determined by the effective field which is magnetic material dependent. Figure 2-10, (b) shows the typical absorption derivative spectrum with the single FMR peak and the Lorentzian fit [30] for 10 nm thick YIG with an in-plane magnetic field. The magnetic resonance appears at the magnetic field of 2405 Oe and the peak-to-peak linewidth is 8.5 Oe. Figure 2-10, (c) shows different absorption derivative spectra as the sample rotates from in-plane to out-of-plane geometry relative to the magnetic field. They all show single FMR peak profile and H_{res} is increased showing a hard axis behavior when the field is in out-of-plane geometry (θ_H= 0°). The resonance field (H_{res}) is smaller in-plane than out of plane indicating dominance of in-plane anisotropy. Also, we measure H_{res} as a function of polar angles (θ_H) and fit to FMR polar angle dependence equations to extract the effective magnetization ($4\pi M_{eff}$) value which is found to be equal to $2113\ Oe$. $4\pi M_{eff} = 4\pi M_s - H_\perp$ [30] and in YIG thin films on GGG, the out-of-plane magnetic anisotropy field $H_\perp$ is negligible and the equation should be $4\pi M_{eff} \approx 4\pi M_s \approx 2113\ Oe$and that is slightly larger than typical magnetization saturation value of YIG (~ 1750) Oe.

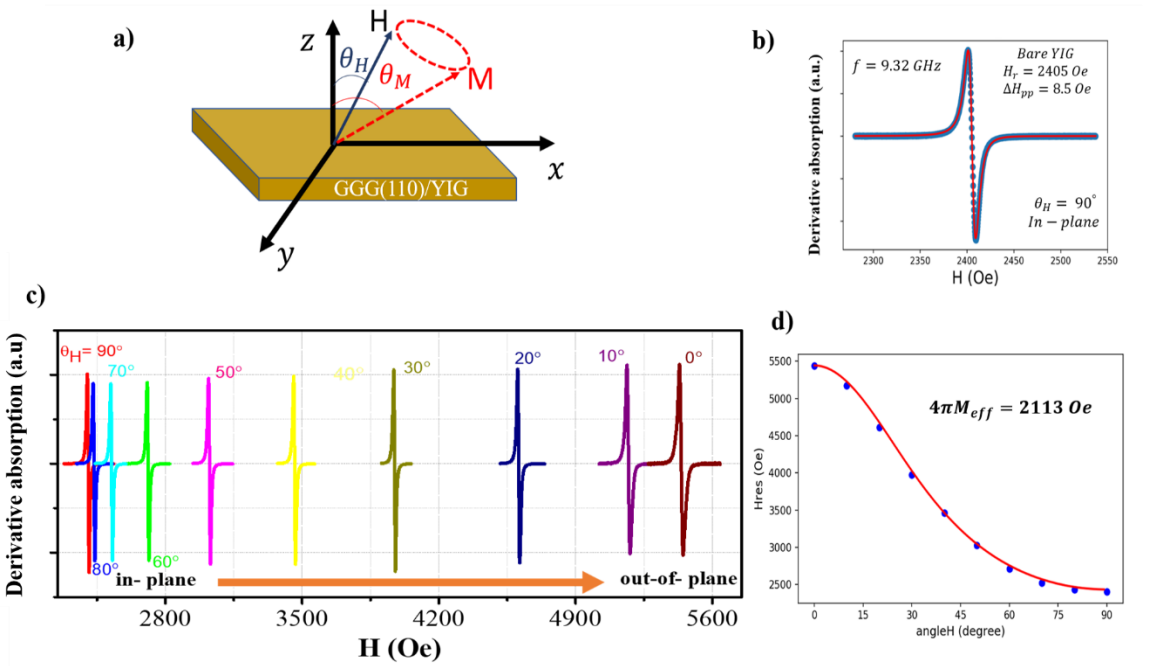

Figure 2- 10: Ferromagnetic resonance (*FMR*) measurements inside the cavity (*f = 9.32GHz*) of 10 nm thick YIG thin film. a) Spin precession of YIG magnetization under FMR excitation and general experimental setup. As seen in the illustration, the static field H is applied with θ_H measured with respect to z axis. b) The typical FMR derivative absorption spectrum in FMR cavity with frequency of *9.32GHz*. Measurement taken at in-plane ($\theta_H = 90^{\circ}$) and from Lorentzian fitting, Hres= 2405 Oe and linewidth (peak-to-peak distance) is 8.5 Oe are obtained. c) The polar angles θ_H dependences Vs. FMR spectra with sample being rotated from in plane ($\theta_H = 90^{\circ}$) to out of plane ($\theta_H = 90^{\circ}$). d) The polar angles (θ_H) dependence as a function of FMR resonance (H_{res}) for 10 nm thick YIG showing in-plane anisotropy dominance with $4\pi M_{eff} = 2113\ Oe$.

The second part of the analysis is to extract the intrinsic Gilbert damping constant (α), ΔH_0, and to fit the Kittle equation for in-plane geometry to obtain the effective saturation magnetization which contains magnetic anisotropy. In CPW based broadband FMR setup, the YIG sample is faced down at the center of CPW and one port of CPW is connected to a signal generator as a RF source and another port is for the transmitted signal to be detected through microwave diode. The result is shown in figure 2-11, part (a) shows the microwave frequency as a function of resonance field (H_{res}) for the in-plane

magnetic field geometry. By fitting the Kittle equation ($f = |\gamma| \sqrt{H_{res}\,(H_{res} + 4\pi M_{eff})}$), we calculate the effective saturation magnetization ($4\pi M_{eff}$) which is equal to 2013 Oe, the same as the result obtained by FMR cavity. $|\gamma|$ is the absolute gyromagnetic ratio ($|\gamma| = g\frac{\mu_B}{\hbar}$) and from fitting, g-factor can be calculated and equal to 2.031 for YIG. Furthermore, Figure 2-11, (b) shows the linear dependence of linewidth on microwave frequency, from which we obtain the intrinsic Gilbert damping constant α from the slope and the inhomogeneity linewidth (ΔH_0) from the intercept. From this relation ($\Delta H = \Delta H_0 + \frac{2\pi\alpha}{\gamma} f$), $\alpha = \frac{slope \times \gamma}{2\pi}$ and ΔH_0 is the inhomogeneity linewidth broadening and referred to as the linewidth at zero field frequency. Therefore, the damping constant α for 10 nm thick YIG is ~ 1.86 × 10^{-3}, and ΔH_0 = 0.69 Oe. Here, $\Delta H_\circ$ is very small which proves excellent homogeneity of the whole YIG thin film.

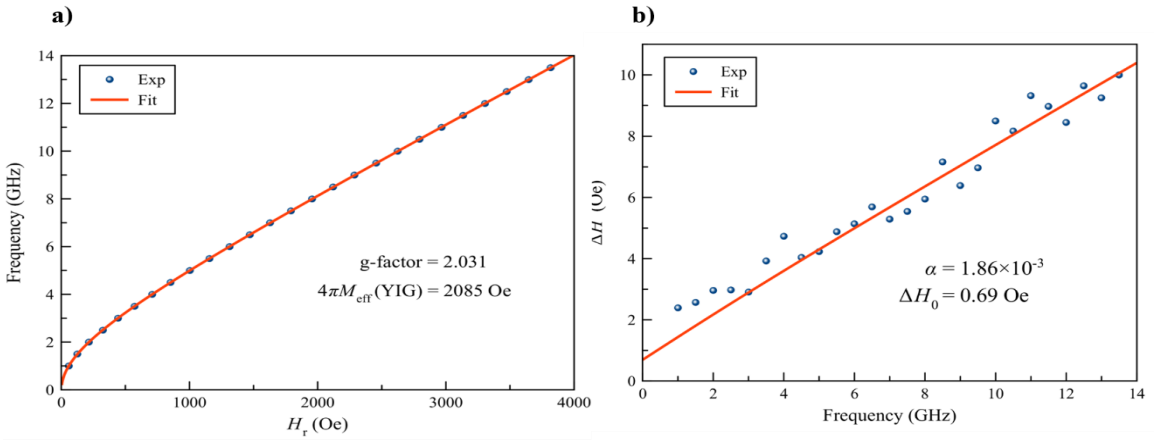

Figure 2- 11: The magnetic anisotropy and Gilbert damping constant of 10 nm thick YIG thin films from the broadband coplanar waveguide measurement with different microwave frequencies. a) The FMR magnetic resonance (H_{res}) as a function of different microwave frequencies for in-plane geometry with ($\theta_H = 90^\circ$) revealing the effective magnetic field value of 2085 Oe and Landé g-factor for YIG is 2.031. b) Linear dependence of FMR spectra linewidth (ΔH) as a function of microwave frequency of the coplanar waveguide giving the Gilbert damping constant (α) as low as 1.86×10^{-3} and inhomogeneity linewidth ($\Delta H_0 = 0.69\ Oe$).

To meet the needs of different projects for YIG films, we have also explored different growth conditions. YIG usually requires high temperature growth to crystallize and become magnetized without subsequent annealing. In some applications, the high growth temperature may not be preferred. To this end, I grow YIG films at room temperature and then explore post-growth annealing conditions. With the room temperature growth, YIG is amorphous as indicated by absence of any RHEED pattern. In this amorphous state, YIG does not show any ferrimagnetic order at room temperature as measured by VSM. We have found that by annealing the room temperature grown YIG in the furnace at 850 ˚C for 6 hours it crystalizes to single crystalline structure as monitored by RHEED. The annealed YIG films are magnetic at room temperature as characterized by VSM.

2.3.2 Growth of Strained YIG on $Y_3Al_5O_{12}$ (YAG) Substrate

The previous section shows growth and characterization of YIG on exactly lattice matched substrate (GGG) with layer by layer growth mode, long RHEED oscillations, excellent surface morphology, and very low damping constant. In this section, we show the epitaxial growth of YIG on mismatch (111) oriented ($Y_3Al_5O_{12}$ or YAG) substrate. The mismatch ratio is defined as $\eta = \frac{(a_s - a_f)}{a_f} \times \%$, where a_s = 12.003 Å and a_f = 12.376 Å are the lattice constants of the YAG substrate and unstrained YIG, respectively.[31] The η ratio is (-3%) which is compressive strain. The purpose of this study

here is to investigate any strain effect which can lead to magnetic property variations such as the magnetic anisotropy. Therefore, we grow 3.5, 7, and 30 nm thick YIG thin films on YAG (111) with optimized growth conditions as listed in previous section. Figure 2-12, (a) are the RHEED patterns for single crystal YAG (111) substrate and (b) is the RHEED pattern after the growth of 7 nm thick YIG. This stained YIG streaky pattern indicates single crystallinity phase. In the meanwhile, YIG growth is monitored by RHEED oscillations with 8 periods in (c) corresponding to 3.5 nm thick and 16 peaks in (d) for the total thickness of 7 nm YIG thin film. These results show that with the compressive strain of (-3%) pseudomorphic growth is possible even through layer-by-layer growth mode.

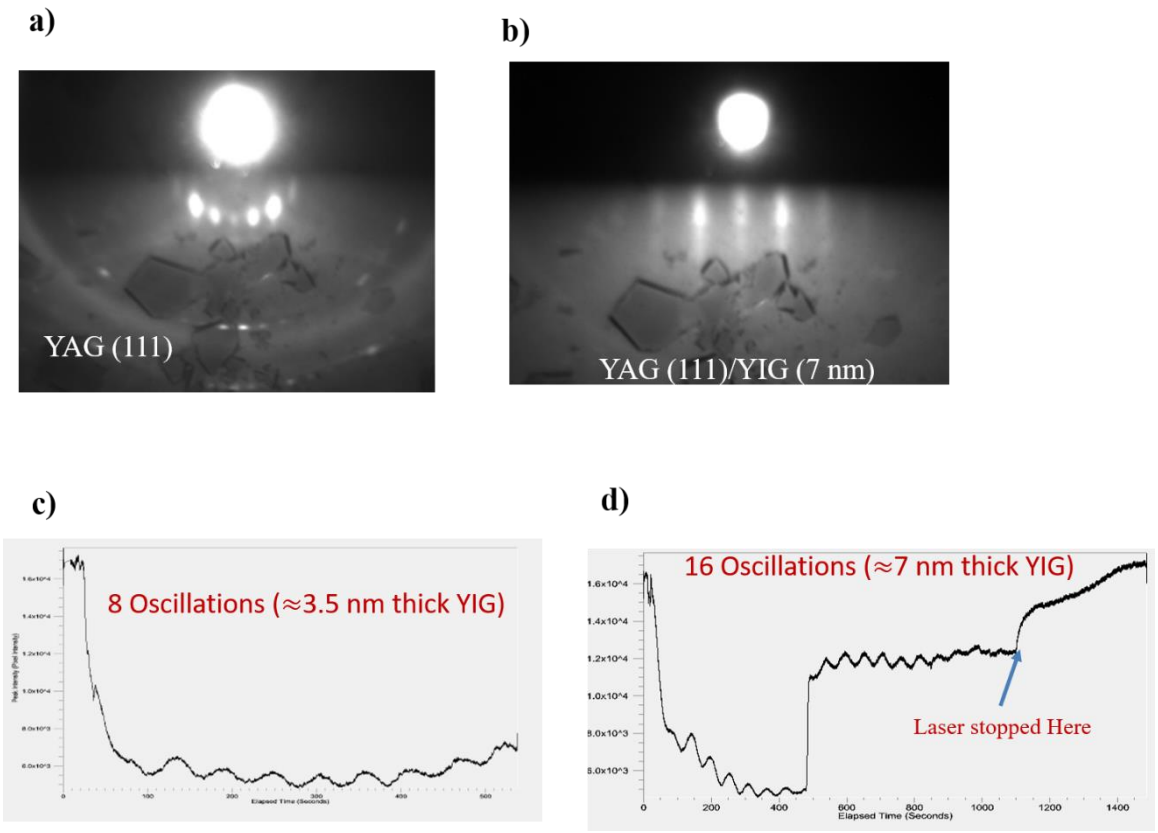

Figure 2- 12: RHEED pattern and oscillations for strained YIG on YAG with the thickness of 3.5 and 7 nm. a) RHEED pattern for YAG substrate. B) RHEED pattern for strained 7 nm thick YIG on YAG. C) Eight oscillations of RHEED corresponds to 3.5 nm thick YIG. D) Sixteen oscillations of RHEED corresponds to additional 3.5 nm thick YIG. Even there is strain, the growth is still layer by layer mood.

VSM measurements are performed at room temperature on three YAG/YIG films with different thicknesses 3.5, 7 and 30 nm. In figure 2-13, (a, b), magnetization measurements show similar hysteresis loop shape for in-plane and out of plane geometries, indicating that the magnetic anisotropy is affected by strain. For figure 2-13, (c), the result shows a similar behavior of unstrained YIG as in GGG/YIG shown in the

previous section in which the easy axis of YIG lies in plane. The squareness defined as (M_r/M_r), where M_r and M_r are the remanence and saturation magnetization, is calculated as a function of the YIG film thickness. It can be seen in figure 2-13, (d) that the squareness is the same for 3 nm between the in-plane and out of plane geometries, but shows some difference for 7 nm thick YIG in which the in-plane squareness is more pronounced than out of plane. For the 30 nm thick YIG, the squareness is ~0.7 for in plane and almost zero for out of plane. The trend in the squareness as a function of the YIG thickness clearly indicates magnetic anisotropy change. However, big surprise comes from FMR measurements for the thin 3.5 and 7 nm YIG on YAG whereas 30 nm sample shows similar behavior as YIG on GGG due to strain relaxation. In 3.5 and 7 nm thick samples, the magnetic resonance field (H_{res}) is shifted from typical value of unstrained YIG ($\approx$ 2300 Oe) down to 1275 Oe for in plane geometry ($\theta_H = 90^\circ$), which is a consequence of additional anisotropy that favors the magnetization in-plane. This large downshift in H_{res} is due to the strain effect and thereby magnetic anisotropy become more in-plane. There are two parameters, the strain type and magnetostriction coefficient (λ_{111}) sign, that are relevant if we want to control anisotropy to be either in or out-of-plane. More discussion on this point will be addressed in chapter seven. Calculated effective saturation magnetization ($4\pi M_{eff}$) for 7.5 nm thick YIG on YAG is 7750 Oe, which is three times as large as the reported value for YIG grown on GGG. The effective out-of-plane anisotropy field ($H_\perp$) is negative with value of 4354 Oe indicating that the anisotropy is strong and toward in-plane. As both the strain and λ_{111} are negative in

YAG/YIG, then the $H_{\perp}$ favors in-plane indicated by the negative sign as shown in table 2-1. More discussion of magnetostriction and $H_{\perp}$ will be presented in chapter seven.

	λ_{111} (10^{-6})	lattice constant (Å)	K_1 (10^{-3} erg·cm^{-3})	$4\pi M_s$ (G)	In-plane strain $\varepsilon_{\parallel}$ on GGG	In-plane strain $\varepsilon_{\parallel}$ on YAG	$H_{\perp}$ on GGG (111) (Oe)	$H_{\perp}$ on YAG (111) (Oe)
YIG	-2.4	12.376	-6.1	1780	0.056%	-3%	80	- 4354

Table 2- 1: Room temperature estimation of perpendicular magnetic anisotropy field ($H_{\perp}$) for YIG grown on GGG (111) and YAG (111).

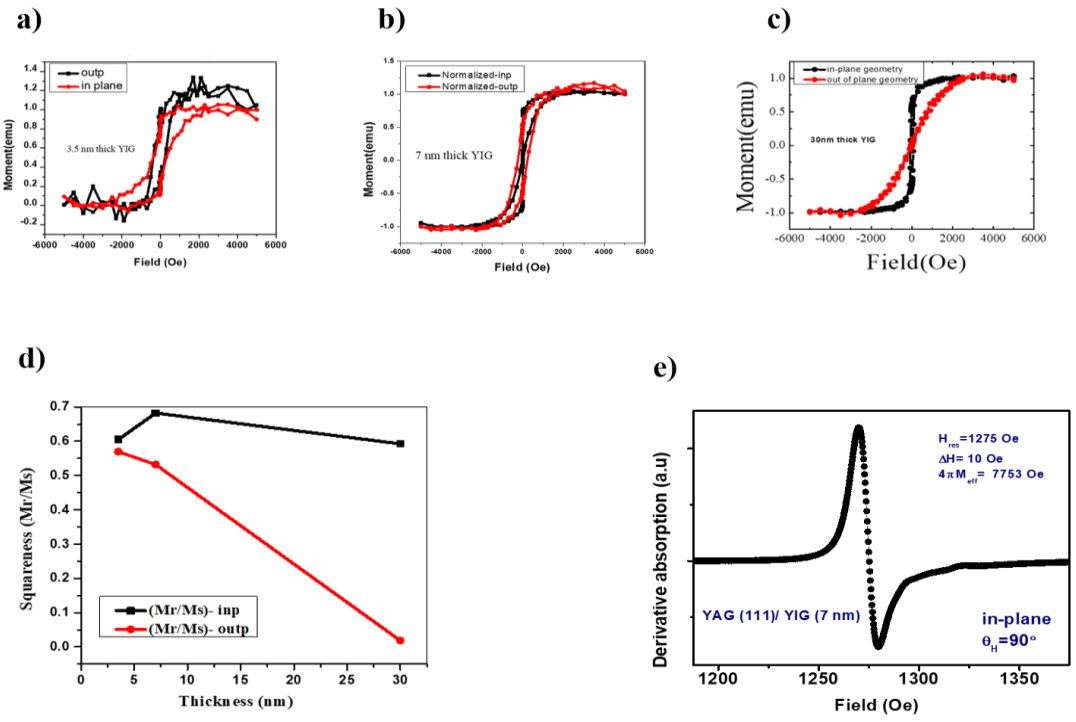

Figure 2- 13: Spontaneous magnetization measurements by VSM and squareness calculations and FMR profile for 7 nm thick YIG grown on YAG (111). a, b, c) VSM measurements for YIG grown on YAG (111) with the thickness of 3.5, 7, 30 nm. d) Calculation of squareness (M_r/M_s) for these three different thicknesses. e) FMR derivative of YIG grown on YAG (111) with thickness of 7 nm yielding single peak with huge shift of H_{res} down to 1275 Oe.

2.3.3 Growth of YIG on Amorphous SiO2/Si Substrate

Some spintronic applications will benefit from having a back-gating ability. If YIG can be grown on Si/SiO2, an external electric field can be applied to YIG. In addition, it would be attractive for industrial applications since the process would be compatible with the current Si technology. Here, we grow YIG on the top of amorphous Si/SiO2 utilizing the 300 nm thick SiO2 dielectric layer as the bottom (back) gate insulator. For example, in YIG/TI heterostructures, a top gate alone may not be effective to tune the chemical potential of bottom surface states to the Dirac point, but the dual gates are needed. However, there are concerns. First, YIG needs to be crystalline in order to be magnetic. Since SiO2 is amorphous, YIG grown on top may also be amorphous, and then it would not be ferrimagnetic. As seen in figure 2-14, (a) YIG grown on SiO2 under proper conditions is magnetic with a clear in-plane easy axis, implying that YIG is not amorphous. In addition, AFM shows that the YIG surface is flat and smooth as seen in figure 2-14, (b) with the RMS roughness of 0.18 nm.

Growth of TI on the top of polycrystalline YIG requires the MBE technique. Our collaborator, Dr. C.-Z. Chang at MIT has successfully grown high-quality $(Bi_xSb_{1-x})_2Te_3$ with different Bi/Sb ratios for different purposes. Despite no lattice match with YIG, $(Bi_xSb_{1-x})_2Te_3$ of five quintuple layers (~ 5 nm in thickness) showed good RHEED patterns. As each layer was deposited, a well-defined RHEED pattern can be seen in figure 2-15, which indicates excellent growth of a single crystal phase material. It is very surprising, but can be understood since the van der Waals interaction between the

quintuple layers of the TI crystal is relatively weak and it does not require atomic registry at the interface to establish its own lattice structure.

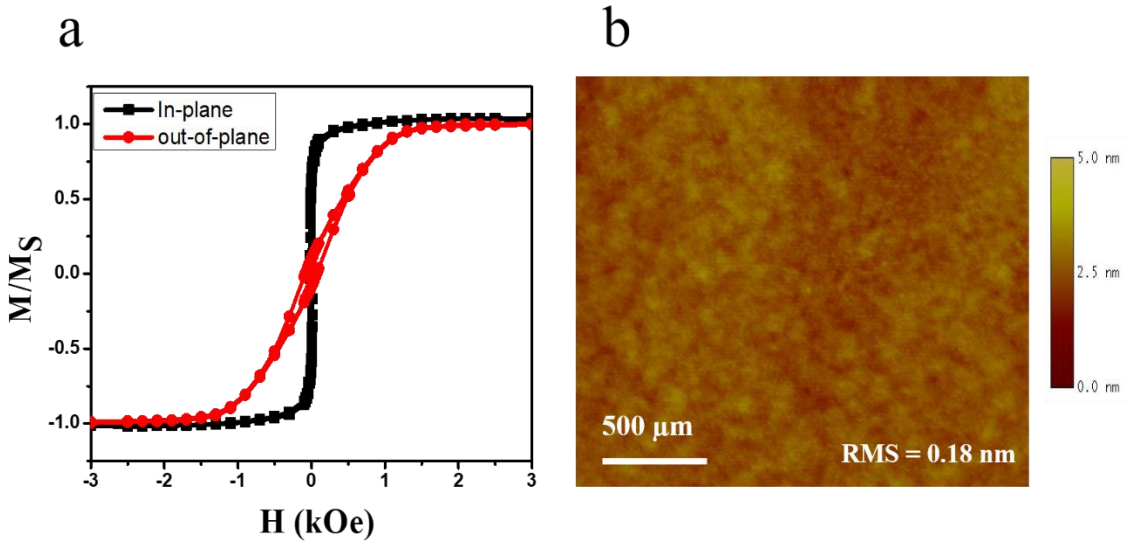

Figure 2- 14: Characterization of polycrystalline YIG grown on amorphous SiO2/Si. a) AFM scan for YIG morphology showing flat surface with roughness mean square (RMS) of 0.18 nm. b) Magnetic characterization carried out by VSM at room temperature showing typical in-plane easy axis and hard axis for out of plane.

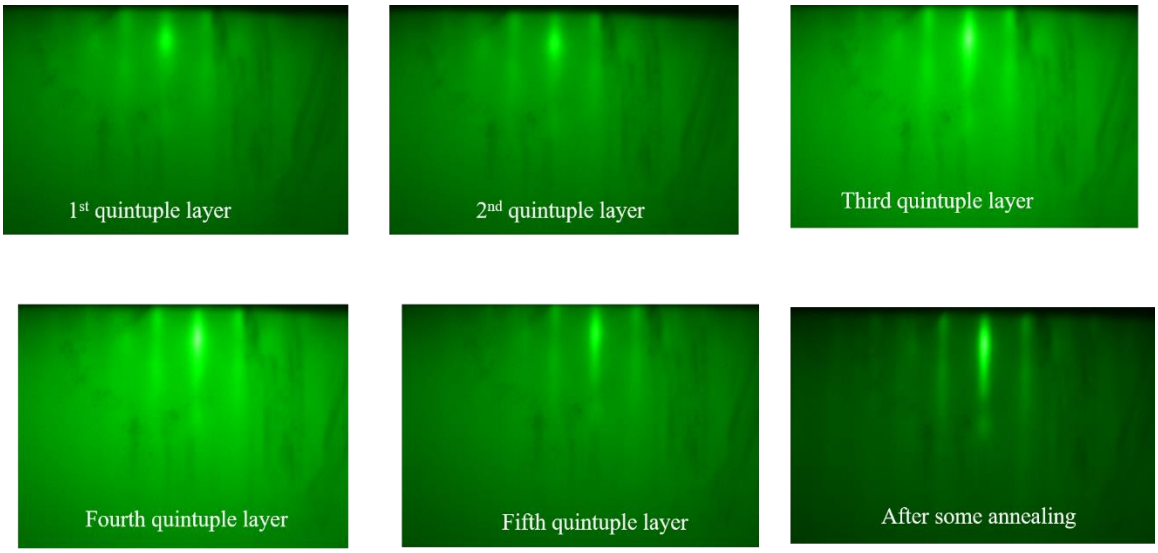

Figure 2- 15: RHEED pattern for growth of topological insulator (TI) with composition of $(Bi_xSb_{1-x})_2Te_3$. Here, it is obvious that TI grow in single structure above polycrystalline YIG. Growth of TI was done by our collaborator at MIT Dr. C. Chang**.**

In summary, we have demonstrated an exquisite control of YIG film growth using PLD. Single crystal YIG films have been epitaxially grown layer by layer up to 227 atomic layers continuously. Under the optimized sample treatment and growth, atomic terraces emerge in (110)-YIG films over a large range of thicknesses, thanks to the layer-by-layer growth mode. (110)-YIG films show well-defined uniaxial in-plane anisotropy. The extremely low damping constant and narrow inhomogeneity linewidth from FMR measurements confirm the superb quality of YIG films resulted from the distinct growth mode. Also, we investigate growth of YIG on mismatched single crystal YAG substrate to study the strained YIG in comparison with the YIG grown on GGG. Finally, we utilize the dielectric layer of SiO_2 on Si to do back gating experiments for graphene and TI by growing polycrystalline YIG on amorphous SiO2.

References:

1. Mallmann, E.J.J., Sombra, A.S.B., Goes, J.C. & Fechine, P.B.A. Yttrium Iron Garnet: Properties and Applications Review. *Solid State Phenomena* **202**, 65-96 (2013).

2. Huang, S.Y. et al. Transport Magnetic Proximity Effects in Platinum. *Physical Review Letters* **109**, 107204 (2012).

3. Lin, T., Tang, Chi and Alyahayaei, Hamad M. and Shi, Jing. Induced magneto-transport properties at palladium/yttrium iron garnet interface. *Applied Physics Letters* **103**, 132407 (2013).

4. Uchida, K. et al. Spin Seebeck insulator. *Nature Materials* **9**, 894 (2010).

5. Castel, V., Vlietstra, N., van Wees, B.J. & Youssef, J.B. Frequency and power dependence of spin-current emission by spin pumping in a thin-film YIG/Pt system. *Physical Review B* **86**, 134419 (2012).

6. Wang, H.L. et al. Scaling of Spin Hall Angle in 3d, 4d, and 5d Metals from $Y_3Fe_5O_{12}$/Metal Spin Pumping. *Physical Review Letters* **112**, 197201 (2014).

7. Heinrich, B. et al. Spin Pumping at the Magnetic Insulator (YIG)/Normal Metal (Au) Interfaces. *Physical Review Letters* **107**, 066604 (2011).

8. C. W. Sandweg, Y.K., K. Ando, E. Saitoh, and B. Hillebrands. Enhancement of the spin pumping efficiency by spin wave mode selection. *Applied Physics Letters* **97**, 252504 (2010).

9. Xingtao, J., Kai, L., Ke, X. & Gerrit, E.W.B. Spin transfer torque on magnetic insulators. *EPL (Europhysics Letters)* **96**, 17005 (2011).

10. Li, J. et al. Observation of magnon-mediated current drag in Pt/yttrium iron garnet/Pt(Ta) trilayers. *Nature Communications* **7**, 10858 (2016).

11. Cornelissen, L.J., Liu, J., Duine, R.A., Youssef, J.B. & van Wees, B.J. Long-distance transport of magnon spin information in a magnetic insulator at room temperature. *Nature Physics* **11**, 1022 (2015).

12. Liu, Y., Xie, L.-S., Yuan, Z. & Xia, K. Magnon-phonon relaxation in yttrium iron garnet from first principles. *Physical Review B* **96**, 174416 (2017).

13. Nakamoto, R., Xu, B., Xu, C., Xu, H. & Bellaiche, L. Properties of rare-earth iron garnets from first principles. *Physical Review B* **95**, 024434 (2017).

14. Nakayama, H. et al. Spin Hall Magnetoresistance Induced by a Nonequilibrium Proximity Effect. *Physical Review Letters* **110**, 206601 (2013).

15. Chenavas, J., Joubert, J.C., Marezio, M. & Ferrand, B. On the crystal symmetry of the garnet structurE. *Journal of the Less Common Metals* **62**, 373-380 (1978).

16. Sun, Y. & Wu, M. in Solid State Physics (eds. Wu, M. & Hoffmann, A.) 157-191 (Academic Press, 2013).

17. Haubenreisser, W. Physics of magnetic garnets. A. Paoletti (ed.). Proceedings of the International School of Physics „Enrico Fermi", Course LXX, Varenna on Lake Como, Villa Monastero, 27th June–9th July 1977. North-Holland Company, Amsterdam 1978 XIII, 542 Seiten, 271 Fig., 35 Tab., 898 Literaturzitate. Preis: US $ 73.25; Dfl 150.—. *Kristall und Technik* **14**, 1490-1490 (1979).

18. Dumont, Y. et al. Tuning magnetic properties with off-stoichiometry in oxide thin films: An experiment with yttrium iron garnet as a model system. *Physical Review B* **76**, 104413 (2007).

19. Christen, H.M. & Eres, G. Recent advances in pulsed-laser deposition of complex oxides. *Journal of Physics: Condensed Matter* **20**, 264005 (2008).

20. Tang, C. et al. Exquisite growth control and magnetic properties of yttrium iron garnet thin films. *Applied Physics Letters* **108**, 102403 (2016).

21. Garay, J.E. Current-Activated, Pressure-Assisted Densification of Materials. *Annual Review of Materials Research* **40**, 445-468 (2010).

22. Biswas, A., Yang, C.-H., Ramesh, R. & Jeong, Y.H. Atomically flat single terminated oxide substrate surfaces. *Progress in Surface Science* **92**, 117-141 (2017).

23. Ma, J.X. et al. Interface ferromagnetism in (110)-oriented La0.7Sr0.3MnO3 /SrTiO3 ultrathin superlattices. *Physical Review B* **79**, 174424 (2009).

24. Koster, G. in In Situ Characterization of Thin Film Growth (eds. Koster, G. & Rijnders, G.) 3-28 (Woodhead Publishing, 2011).

25. Krockenberger, Y. et al. Layer-by-layer growth and magnetic properties of Y3Fe5O12 thin films on Gd3Ga5O12. *Journal of Applied Physics* **106**, 123911 (2009).

26. Ichimiya, A. & Cohen, P.I. Reflection High-Energy Electron Diffraction (Cambridge University Press, Cambridge, 2004).

27. Onbasli, M.C. et al. Pulsed laser deposition of epitaxial yttrium iron garnet films with low Gilbert damping and bulk-like magnetization. *APL Materials* **2**, 106102 (2014).

28. Rosencwaig, A., Tabor, W.J., Hagedorn, F.B. & Van Uitert, L.G. Noncubic Magnetic Anisotropies in Flux-Grown Rare-Earth Iron Garnets. *Physical Review Letters* **26**, 775-779 (1971).

29. Cullity, B.D. (Addison-Wesley Pub. Co., Reading, Mass., 1972).

30. Yajun, W., Shin Liang, C. & Peter, S. On the frequency and field linewidth conversion of ferromagnetic resonance spectra. *Journal of Physics D: Applied Physics* **48**, 335005 (2015).

31. Wang, H., Du, C., Hammel, P.C. & Yang, F. Strain-tunable magnetocrystalline anisotropy in epitaxial Y3Fe5O12 thin films. *Physical Review B* **89**, 134404 (2014).

Chapter 3

Platinum/Yttrium Iron Garnet Inverted Structures for Pure Spin Current Transport

3.1 Introduction to Inverted Structure of GGG (110)/Pt/YIG

To form conventional bilayers, a thin polycrystalline metal layer is typically deposited on top of magnetic insulators, here is YIG, by sputtering, which results in reasonably good interfaces for spin current transport.[1,2] For some studies such as the magnon-mediated current drag,[3,4] sandwiches of metal/YIG/metal are required, in which YIG needs to be both magnetic and electrically insulating. However, high-quality bilayers of the reverse order, i.e. YIG on metal, are very difficult to be fabricated. A main challenge is that the YIG growth requires high temperatures and an oxygen environment[5] which can cause significant inter-diffusion, oxidation of the metal layer, etc. and consequently lead to poor structural and electrical properties in both metal and YIG layers.

Therefore, in this chapter, I will report the controlled growth of high-quality single crystal YIG thin films ranging from 30 to 80 nm in thickness on a 5 nm thick Pt layer atop $Gd_3Ga_5O_{12}$ or GGG (110) substrate. Combined with low-temperature growth which suppresses the inter-diffusion, subsequent rapid thermal annealing (RTA) and optimization of other growth parameters result in well-defined magnetism, atomically sharp Pt/YIG interface, and atomically flat YIG surface. In addition, despite the intermediate Pt layer that has a drastically different crystal structure from the garnets, the

top YIG layer shows desired structural and magnetic properties as if it were epitaxially grown on GGG (110).

3.2 Optimized Growth Conditions of YIG on Top of Pt

5×5 mm^2 of commercial GGG (110) single crystal substrates are first cleaned in ultrasonic baths of acetone, isopropyl alcohol, then deionized water, and dried by pure nitrogen gun. Subsequently, the substrates are annealed in a furnace at 900 °C in O_2 for eight hours which produces atomically flat surface. Atomic force microscopy (AFM) is performed to track the surface morphology of the annealed substrates. Figure 3-1, (a) shows the 2x2 μm^2 AFM scan of an annealed GGG (110) substrate. Flat atomic terraces are clearly present and separated with a step height of 4.4 ± 0.2 Å which is equal to ¼ of the face diagonal of the GGG unit cell or the (220) interplanar distances of 4.4 Å of GGG. The 4.4 Å distance is the separation between the GaO_6 octahedral layers parallel to (110) that might be defining the observed atomic step ledges. The root-mean-square (RMS) roughness on the terraces is ~0.74 Å. Then, the substrate is transferred into a sputtering chamber with a base pressure of 5 □ 10^{-8} Torr for Pt deposition. DC magnetron sputtering is used with the Ar pressure of 5 mTorr and power of 37.5 W. The sputtering deposition rate is 0.76 Å/s and sample holder rotation speed is 10 RPM. After the 5 nm thick Pt deposition, the surface of the Pt film is found to maintain the atomic terraces of the GGG (110) substrate, except that the RMS roughness on the Pt terraces is increased to 1.05 Å as shown in figure 3-1, (b). It is rather surprising that the 5 nm thick Pt layer does not smear out the terraces separated by atomic distances given that the

sputtering deposition is not particularly directional. Strikingly, terraces are still present even in 20 nm thick Pt (not shown). The substrates are then put in a PLD chamber which has a base pressure of 4 □ 10^{-7} Torr and are slowly heated to 450 °C in high-purity oxygen with the pressure of 1.5 mTorr with 12 wt% of ozone. The krypton fluoride (KrF) coherent excimer laser (λ = 248 nm, 25 ns/pulse) used for deposition has a pulse energy of 165 mJ/pulse, and repetition rate of 1 Hz. The deposition rate of ≈ 1.16 Å/min is achieved with a target to substrate distance of 6 cm. After deposition, the YIG films are *ex situ* annealed at 850 °C for 200 seconds using rapid thermal annealing (RTA) under a steady flow of pure oxygen.

3.3 Surface and Structure Characterizations

After RTA, the surface morphology is examined by AFM again. Figure 3-1, (c) shows the atomically terraced surface of a 40 nm thick YIG film with RMS of 1.24 Å on the terrace. In this study, the thickness of YIG ranges from 30 – 80 nm and all samples exhibit clear atomic terraces. Even though YIG is annealed at such a high temperature, with the short annealing time, the flat and smooth YIG surface is maintained. To track the structural properties of YIG, we use RHEED to characterize the YIG surface at every step of the process. Figure 3-1, (d) shows the RHEED pattern of the as-grown YIG surface. It clearly indicates the absence of any crystalline order. After the *ex situ* RTA, the sample is introduced back to the PLD chamber for RHEED measurements again. A streaky and sharp RHEED pattern is recovered as displayed in Figure 3-1, (e) which

suggests a highly crystalline order. This result is particularly interesting since it shows the characteristic RHEED pattern of YIG grown on GGG.

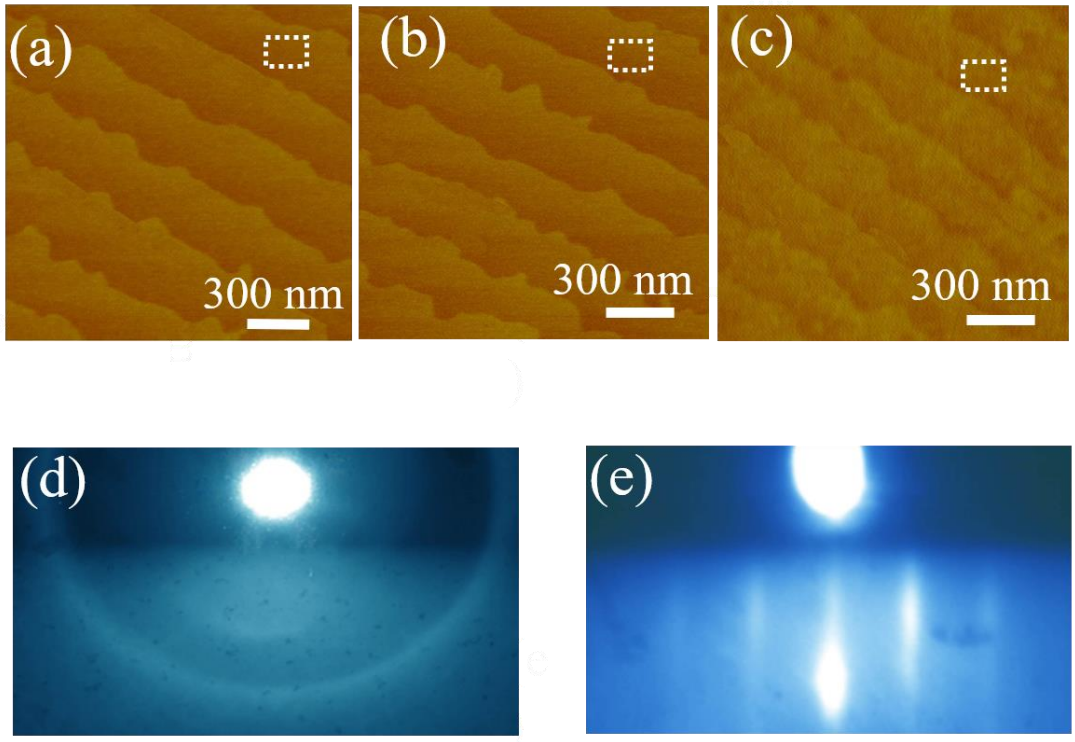

Figure 3- 1: Surface characterization of YIG thin film grown on GGG (110)/Pt (5 nm). (a)–(c) 2 μm × 2 μm AFM scans of GGG (110) substrate, GGG (110)/Pt (5 nm), and GGG/Pt (5 nm)/YIG (40 nm), respectively. RHEED patterns of as-grown (d) and annealed (f) GGG (110)/Pt (5 nm)/YIG (40 nm).

To further confirm its crystalline structure, x-ray diffraction (XRD) using the Cu Kα1 line has been carried out over a wide-angle range (2θ from 10 to 90°) on the GGG/Pt/YIG sample discussed in Figure 3-2, (a). Because of the close match in lattice constants between YIG and GGG substrate, weak YIG peaks are completely overlapped with strong peaks of GGG so that they are indistinguishable. Three main Bragg peaks of YIG and GGG are observed: 220, 440, and 660, which suggests the (110) growth

orientation of both YIG and GGG. No individual weak YIG peaks can be found. It is striking that the YIG film adopts the crystallographic orientation of GGG despite the intermediate Pt layer. By comparing with the spectra of YIG grown directly on GGG, we can identify a new peak ($2\theta \approx 40.15°$) which is better seen in the zoom-in view in the figure 3-2, (b). We determine this as the 111 peak of the 5 nm thick Pt film that suggests the (111) texture of the Pt layer. It is not clear whether the (111) texture in the intermediate Pt layer is required for YIG to develop the same crystallographic orientation as that of the GGG substrate.

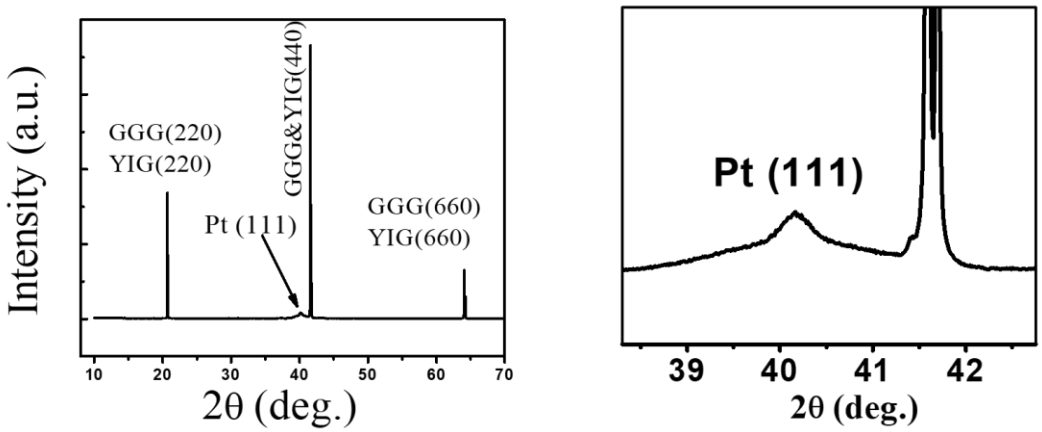

Figure 3- 2: XRD for Structure characterization of GGG/Pt/YIG heterostructure. (a) XRD of YIG film (40 nm) grown on GGG (110)/Pt (5 nm). b) Zoom-in plot of Pt 111 peak ($2\theta = 40.15°$).

3.4 High-Resolution TEM Result

The locking of the (110) orientation in both YIG and GGG is further investigated by the high-resolution transmission electron microscopy (HRTEM) in real space. Figure 3-3, (a) first reveals sharp and clean interfaces of Pt/YIG and GGG/Pt. No amorphous phase or inclusions are visible at these two interfaces. Furthermore, the (110) atomic planes of YIG and GGG are parallel to each other and show very closely matched inter-planar spacing. Despite the Pt layer in between, the crystallographic orientation of YIG is not interrupted as if it were epitaxially grown on GGG directly. In the selected area electron diffraction pattern shown in figure 3-3, (b), taken along the zone axis in garnet from an area that includes all three phases, YIG and GGG diffraction spots overlap with each other, consistent with the XRD results. There is minor splitting of the 110 type reflections from the two garnet phases due to a slight rotation of the two garnet lattices of less than 0.5°. Surprisingly, the diffraction spots from the 5 nm Pt layer show a single crystal pattern with minor streaking parallel to 111 in Pt. The diffuse character of the Pt reflections suggests that Pt is essentially a single crystal consisting of small (few nanometers) structural domains with minor misalignments. The contrast variation in different regions of Pt shown in figure 3-3, (a) is consistent with such small structural domain misalignments in Pt crystal grain orientations. Furthermore, the 111 reciprocal vector of Pt and the 110 reciprocal vector of YIG/GGG are both perpendicular to the interfaces, indicating that the (111) Pt layers are parallel to the (110) layers of both GGG and YIG. Figure 3-3, (c) is a HRTEM image with high magnification of the three layers.[6]

It further reveals atomically sharp interfaces, interlocked (110) crystallographic orientations between GGG and YIG, and single crystal (111)-oriented Pt.

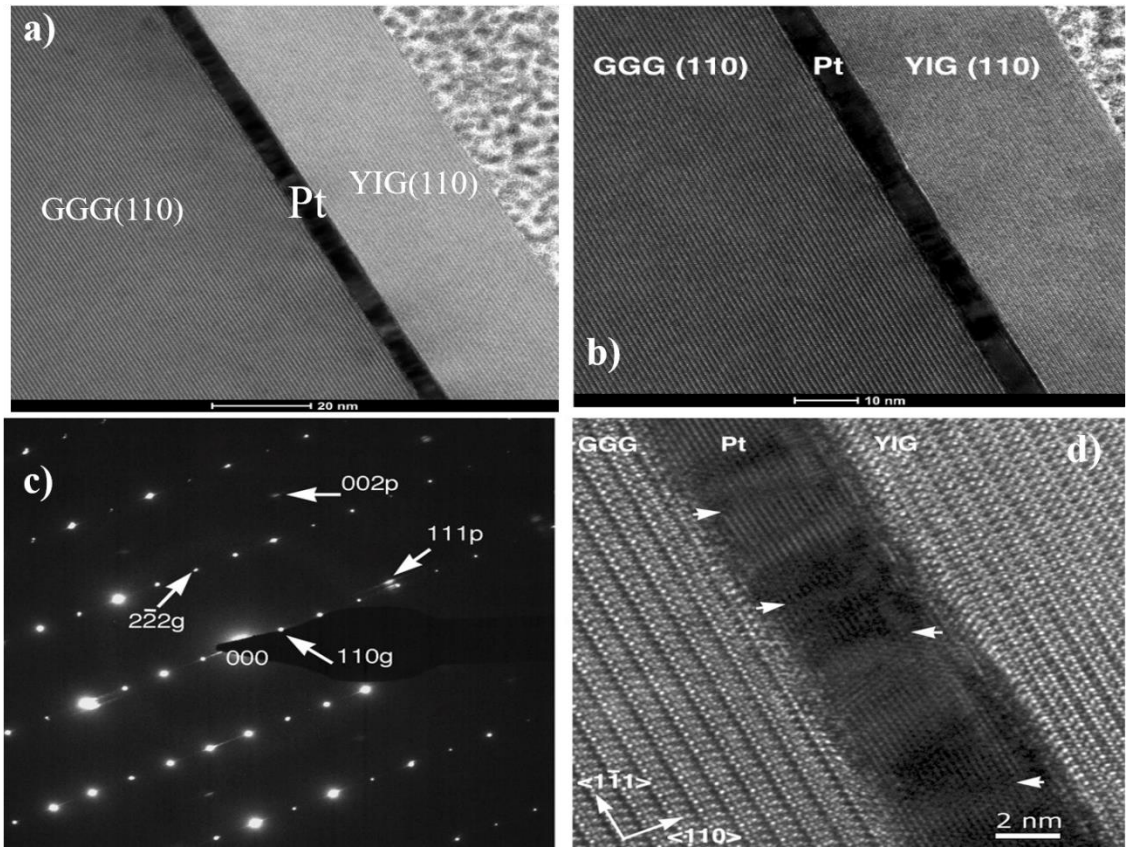

Figure 3- 3: HR-TEM images for lower and higher magnifications for GGG/Pt/YIG heterostructure. a) TEM image of GGG (110)/Pt (5 nm)/YIG (110) (40 nm) heterostructure for lower magnification. b) TEM image of GGG (110)/Pt (5 nm)/YIG (110) (40 nm) heterostructure for higher magnification. The <1$\underline{1}$1> and <110> directions in GGG are shown for reference. (c) Selected area electron diffraction pattern along [$\underline{1}$12] zone axis in GGG obtained from an area containing all three layers showing diffraction spots of YIG, GGG and Pt. The garnet reflections are labeled with subscript "g" and Pt ones with "p". (d) HRTEM lattice image along the [$\underline{1}$12] zone axis in garnet shows that (110) planes in both YIG and GGG are parallel to the interface with the Pt film, and the latter is composed of nanometer size crystalline domains oriented with their (111) lattice planes parallel to the interface as well. Slight bending and disruption of the (111) lattice fringes between adjacent Pt domains are visualized.

3.5 Magnetic Properties of Pt/YIG Inverted Structure

To investigate the magnetic properties of the GGG/Pt/YIG inverted heterostructure, vibrating sample magnetometry (VSM) measurements are carried out at room temperature. As-grown YIG films do not show any well-defined crystalline structure as indicated by the RHEED pattern. In the meantime, the VSM measurements do not show any detectable magnetization signal. Upon RTA, single crystal YIG becomes magnetic as shown by the hysteresis loops in Figure 3-4, (a) for magnetic fields parallel and perpendicular to the sample plane. GGG's paramagnetic contribution has been removed by subtracting the linear background from the raw data. The easy axis of all YIG films with different thicknesses lies in the film plane due to the dominant shape anisotropy. The coercivity falls in the range of 15 - 30 Oe for different thicknesses, which is larger than the typical value (0.2 to 5 Oe) for YIG films grown on lattice-matched GGG. The inset of Figure 3-4, (a) shows a coercive field of 29 Oe for a 40 nm thick YIG film. The saturation magnetic field in the perpendicular direction is ~1800 Oe which corresponds well to 4□Ms for bulk YIG crystals (1780 Oe). Magnetic hysteresis loops are measured along different directions in the film plane. Figures 3-4, (b & c) show the polar angular dependence of both the coercive field (H_c) and squareness (M_r/M_s) where M_r is the remanence and M_s is the saturation magnetizations, respectively. In the film

plane, there is clear uniaxial magnetic anisotropy, with the in-plane easy and hard axes situated along at $\varphi = 145°$ and at $\varphi = 55°$, respectively. This two-fold symmetry indicates that the magneto-crystalline anisotropy is the main source of the anisotropy since it coincides with the lattice symmetry of (110) surface of the YIG films, which is also consistent with the magnetic anisotropy property of YIG epitaxially grown on GGG (110).[6,7] On the other hand, for YIG (111) either grown directly on GGG (111) or on Pt/GGG 111), there is no in-plane uniaxial anisotropy or any kind of fold symmetry as seen in figure 3-4, (d, e) for azimuth angular dependence of the coercive field and squareness as a function of magnetic field.

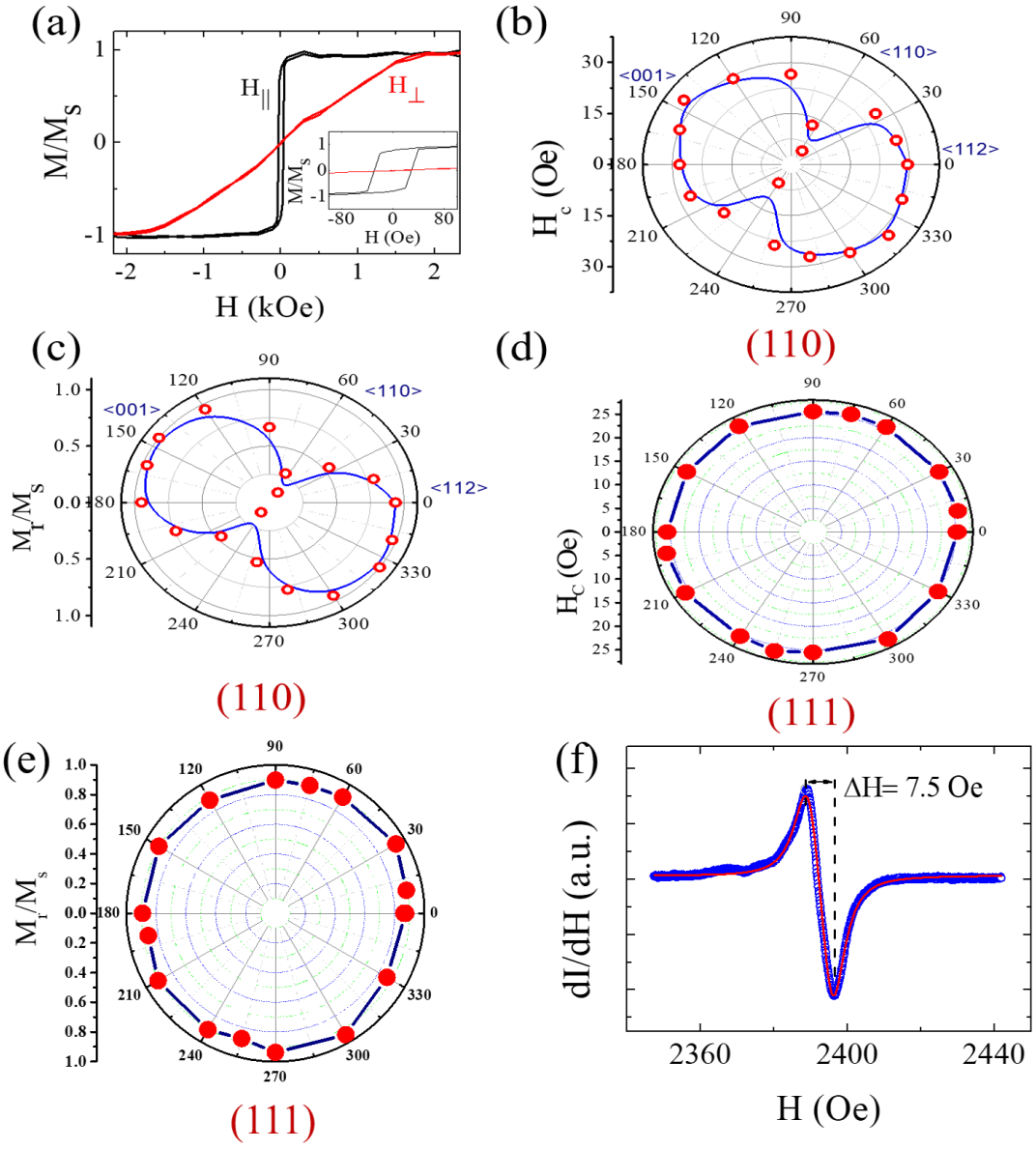

Figure 3- 4: Magnetic properties of GGG(110) and GGG(110)/Pt(5 nm)/YIG (40 nm). (a) Room temperature normalized magnetic hysteresis loops of YIG (40 nm)/ Pt (5nm)/GGG (110) with magnetic field applied in-plane and out-of-plane. Inset: in-plane hysteresis loop at low fields. Polar plots of coercive field H_c (b) and squareness M_r/M_s (c) as the magnetic field H is set in different orientations in the (110) plane (H // at 0°) for (110). Polar plots of coercive field H_c (c) and squareness M_r/M_s (d) as the magnetic field H for (111) orientation. (f) FMR absorption derivative spectrum of YIG/Pt/GGG at an excitation frequency of 9.32 GHz. Lorentzian fit (red line) shows a single peak with a peak-peak distance of 7.5 Oe.

Ferromagnetic resonance (FMR) measurements of YIG films are carried out using Bruker EMX EPR (Electron Paramagnetic Resonance) spectrometer with an X-band microwave cavity operated at the frequency of f = 9.32 GHz. A static magnetic field is applied parallel to the film plane. Figure 3-4, (f) shows a single FMR peak profile in the absorption derivative. From the Lorentzian fit, the peak-peak linewidth (ΔH_{pp}) and resonance frequency (H_{res}) are 7.5 Oe and 2392 Oe, respectively. In literature, both the linewidth and the saturation magnetization vary over some range depending on the quality of YIG films. These values are comparable with the reported values for epitaxial YIG films grown directly on GGG.[7,8] The FMR linewidth here seems to be larger than what is reported in the best YIG films grown on GGG. Considering the excellent film quality, it is reasonable to assume that the same YIG would have similar FMR linewidth, e.g., 3 Oe. In the presence of Pt, increased damping in Pt/YIG occurs due to spin pumping.[9,10] This additional damping can explain the observed FMR linewidth (7.5 Oe) [6] if a reasonable spin mixing conductance value of $g_{eff}^{\uparrow\downarrow} \approx 5 \times 10^{18}\ \ m^{-2}$ is assumed.

3.6 Magneto-Transport Measurements

3.6.1 Spin Hall Magnetoresistance (SMR) Measurements

The Pt layer underneath YIG allows for pure spin current generation and detection just as when it is placed on top. It is known that the interface quality is critical to the efficiency of spin current transmission.[11,12] To characterize this property, we perform spin Hall magnetoresistance (SMR) and SSE measurements in GGG/Pt/YIG inverted heterostructures. SMR is a transport phenomenon in bilayers of heavy metal/magnetic insulator.[13,14] A charge current flowing in the normal metal with strong spin-orbit coupling generates a spin current orthogonal to the charge current via the spin Hall effect. The reflection and absorption of this spin current at the interface of the normal metal/magnetic insulator depends on the orientation of the magnetization (*M*) of the magnetic insulator. Due to the spin transfer torque mechanism, when M is collinear with the spin polarization σ, reflection of the spin current is maximum. In contrast, when *M* is perpendicular to σ, absorption is maximum; therefore, the resistance of the normal metal is larger than that for $M||\sigma$ since the absorption behaves as an additional dissipation channel. Metal/magnetic insulator interface quality affects the SMR magnitude. As illustrated in figure 4(a, b and c), we carry out angle-dependent magnetoresistance (MR) measurements by rotating a constant magnetic field in the(xy) with (H=2000 Oe), (xz) with (H=1 T), or yz-plane with (H=1 T), while the current flows along the x-axis. The angular dependence of the MR ratio, $\frac{\Delta\rho}{\rho}$ (%) = $\frac{\rho(angle)-\rho\,(angle=\frac{\pi}{2})}{\rho\,(angle=\frac{\pi}{2})}$ × 100, for Pt film at

room temperature is summarized in figure 4(d). According to the SMR theory, the longitudinal resistivity reads $\rho = \rho_0 + \rho_1 m_y^2$ where ρ_0 and ρ_1 are magnetization-independent constants, and m_y is the y-component of the magnetization unit vector. The red solid curves in figure 4(b) can be well described by equation (1). Here, the magnitude of SMR in xy- and yz- scans is on the same order as that in normal YIG/Pt bilayer systems. Therefore, we demonstrate that the SMR mechanism dominates in our devices, which indicates excellent interface quality for spin current transport.

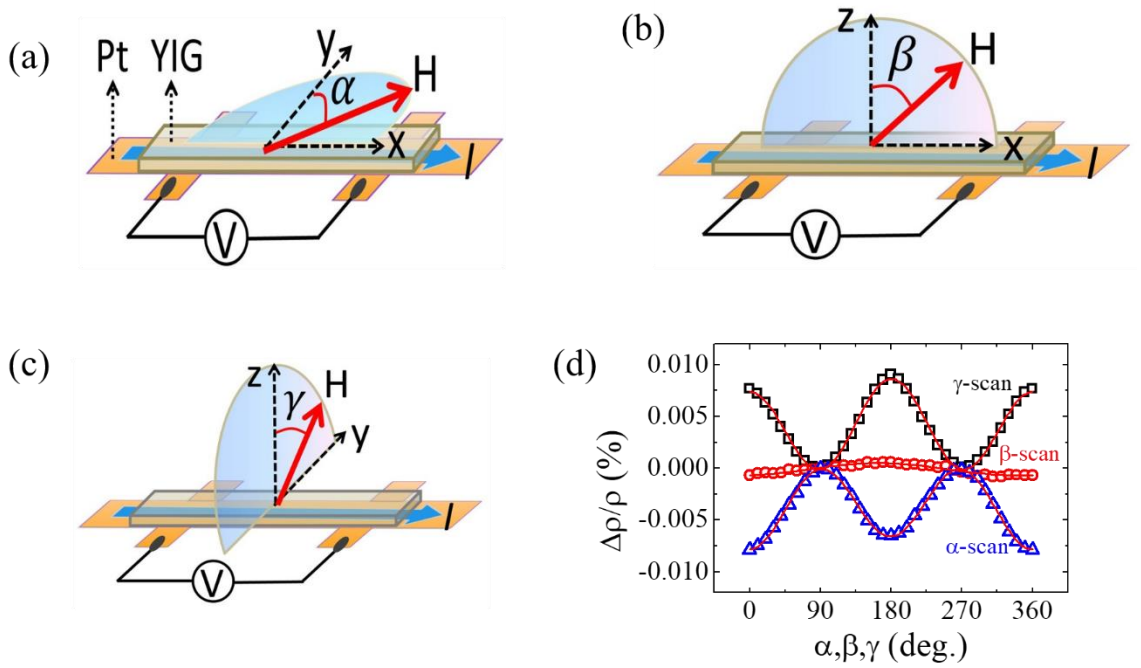

Figure 3- 5: SMR of GGG(110)/Pt(5 nm)/YIG(40 nm). (a) Illustrations of measurement geometry of SMR. α, β **and** γ are angles between H and y, z and z, axes, respectively. The magnitude of $\boldsymbol{H}$ is 2000 Oe, 1T, and 1T for $\boldsymbol{\alpha}-$, $\boldsymbol{\beta}-$, **and** $\boldsymbol{\gamma}-$and scans, respectively. (d) Angular dependence of SMR ratios for three measurement geometries at 300 K.

3.6.2 Longitudinal Spin Seebeck Effect (SSE) Measurements

SSE, on the other hand, is related to the transmission of thermally excited spin currents through the heavy metal/YIG interface.[15,16,17] As illustrated in figure 3-6(a), we first deposit a 300 nm thick Al2O3 layer atop GGG(110)/Pt(5 nm)/YIG(40 nm), and a top heater layer consisting of 5 nm Cr and 50 nm Au. When an electrical current (50 mA) flows in the Cr/Au layer, a temperature gradient is established along the z-direction by joule heating, which generates a spin current in YIG. As the spin current enters the Pt layer, it is converted into a charge current or voltage due to the inverse spin Hall effect as depicted in figure 3-6, (b). A magnetic field is applied in the y-direction while the voltage is detected along the x-direction. In Figure 3-6, (c), we plot the field dependence of the normalized SSE signal at different temperatures ranging from 300- 20 K, which is consistent with the SSE magnitude reported in YIG/Pt bilayers. Also, we plot normalized SSE magnitude as a function of temperature indicating smaller signals at lower temperature as a magnons suppress. Therefore, we have confirmed the excellent interface quality for transmitting thermally excited spin currents.

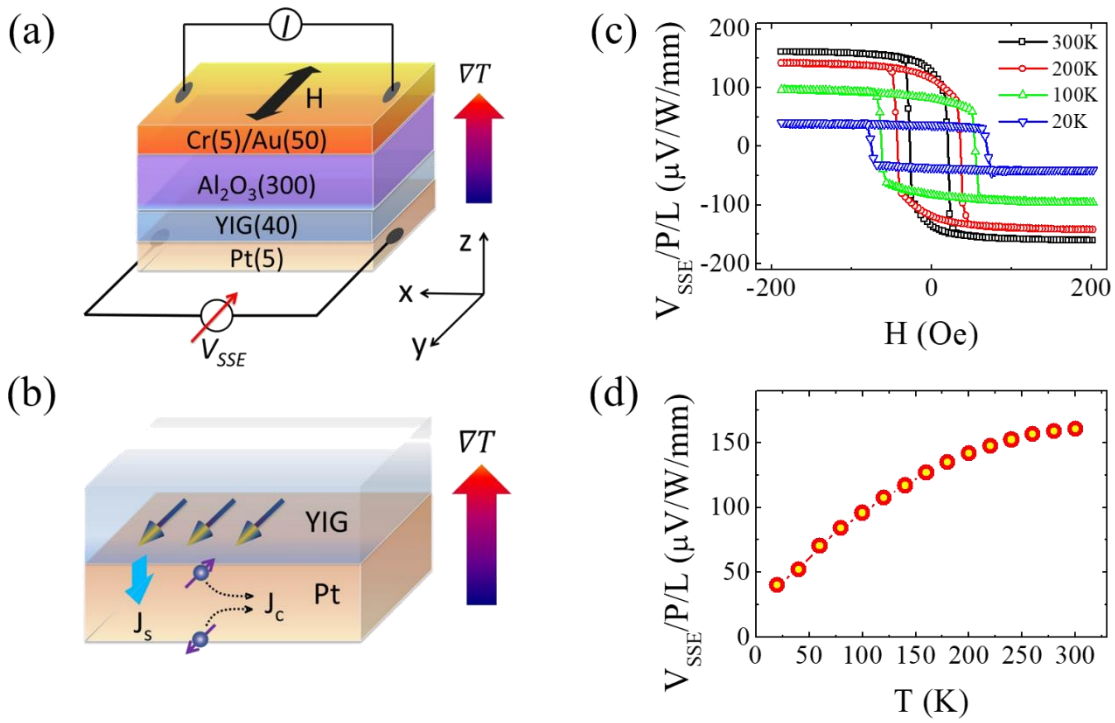

Figure 3- 6: Longitudinal SSE of GGG(110)/Pt(5 nm)/YIG(40 nm). (a) The sample structure and measurement geometry of longitudinal SSE. The heater current I is 50 mA and H is applied along the y direction. All the thicknesses are denoted in nanometers (nm). (c) Field dependence of room temperature SSE signal, which is normalized by the heating power P and detecting length L.

In summary, single crystal YIG thin films have been grown on Pt film which is sputtered on GGG (110) substrate. RHEED and AFM show excellent YIG surface quality and morphology. XRD and HRTEM further reveal an intriguing crystal orientation locking between YIG and GGG as if no Pt were present. These YIG films exhibit similar excellent magnetic properties to those of the YIG films grown epitaxially on GGG (110). Both SMR and SSE results confirm that the superb structural and magnetic properties lead to excellent spin current transport properties.

References:

1. Lin, T., Tang, C., Alyahayaei, H.M. & Shi, J. Experimental Investigation of the Nature of the Magnetoresistance Effects in Pd-YIG Hybrid Structures. *Physical Review Letters* **113**, 037203 (2014).

2. Heinrich, B. et al. Spin Pumping at the Magnetic Insulator (YIG)/Normal Metal (Au) Interfaces. *Physical Review Letters* **107**, 066604 (2011).

3. Zhang, S.S.L. & Zhang, S. Magnon Mediated Electric Current Drag Across a Ferromagnetic Insulator Layer. *Physical Review Letters* **109**, 096603 (2012).

4. Li, J. et al. Observation of magnon-mediated current drag in Pt/yttrium iron garnet/Pt(Ta) trilayers. *Nature Communications* **7**, 10858 (2016).

5. Krockenberger, Y., Matsui, H., Hasegawa, T., Kawasaki, M. & Tokura, Y. Solid phase epitaxy of ferrimagnetic Y3Fe5O12 garnet thin films. *Applied Physics Letters* **93**, 092505 (2008).

6. Aldosary, M. et al. Platinum/yttrium iron garnet inverted structures for spin current transport. *Applied Physics Letters* **108**, 242401 (2016).

7. Tang, C. et al. Exquisite growth control and magnetic properties of yttrium iron garnet thin films. *Applied Physics Letters* **108**, 102403 (2016).

8. Onbasli, M.C. et al. Pulsed laser deposition of epitaxial yttrium iron garnet films with low Gilbert damping and bulk-like magnetization. *APL Materials* **2**, 106102 (2014).

9. Lustikova, J. et al. Spin current generation from sputtered Y3Fe5O12 films. *Journal of Applied Physics* **116**, 153902 (2014).

10. Burrowes, C. et al. Enhanced spin pumping at yttrium iron garnet/Au interfaces. *Applied Physics Letters* **100**, 092403 (2012).

11. Weiler, M. et al. Experimental Test of the Spin Mixing Interface Conductivity Concept. *Physical Review Letters* **111**, 176601 (2013).

12. Lu, Y.M. et al. Hybrid magnetoresistance in the proximity of a ferromagnet. *Physical Review B* **87**, 220409 (2013).

13. Nakayama, H. et al. Spin Hall Magnetoresistance Induced by a Nonequilibrium Proximity Effect. *Physical Review Letters* **110**, 206601 (2013).

14. Chen, Y.-T. et al. Theory of spin Hall magnetoresistance. *Physical Review B* **87**, 144411 (2013).

15. Schreier, M. et al. Magnon, phonon, and electron temperature profiles and the spin Seebeck effect in magnetic insulator/normal metal hybrid structures. *Physical Review B* **88**, 094410 (2013).

16. Rezende, S.M., Rodríguez-Suárez, R.L., Lopez Ortiz, J.C. & Azevedo, A. Thermal properties of magnons and the spin Seebeck effect in yttrium iron garnet/normal metal hybrid structures. *Physical Review B* **89**, 134406 (2014).

17. Meier, D. et al. Longitudinal spin Seebeck effect contribution in transverse spin Seebeck effect experiments in Pt/YIG and Pt/NFO. *Nature Communications* **6**, 8211 (2015).

Chapter 4

Observation of Magnon-Mediated Current Drag Effect in Pt/Yttrium Iron Garnet/Pt(Ta) Heterostructures

4.1 Introduction to Magnon-Mediated Current Drag Effect

Pure spin current, a flow of spin angular momentum without flow of any companying net charge, is generated in two common ways. One makes use of the spin Hall effect in heavy metals (HM) with strong spin-orbit coupling, such as Pt or Ta. The charge current carried by conduction electrons is converted into a pure spin current in the transverse direction. The other utilizes the collective motion of magnetic moments in magnetic materials or spin waves with the quasi-particle excitations called magnons. Recently, a theoretical model has been proposed by Zhang *et al.*[1,2] for observing magnon mediated electric current drag across a ferrimagnetic insulator layer in a heavy metal (HM)/ ferrimagnetic insulator (MI)/ heavy metal (HM) structure as shown in figure 4-1, (a). in this model.[1] by applying electric current in one layer of HM, due to spin Hall effect (SHE) the spin current will be generated in transverse direction. At the boundary between HM and FM, nonequilibrium spin are accumulated due to *s-d* exchange interaction creating magnons at the interface. Those magnons current propagate through FM layer and diffuse to another interface in which they convert back to electron spin current leading to charge current through inverse spin Hall effect (ISHE). Rather than exciting a coherent precession of magnetization in the MI, at one interface, electrons in the HM

create or annihilate magnons in the MI which then carry the spin current as seen in figure 4-1, (b&c). The reverse process at the other interface occurs which consequently converts the spin current entering the other HM into a charge current via the ISHE. The individual magnon creation/annihilation does not need to overcome any threshold; therefore, the interconversion takes place at any current. Due to the long magnon decay length in MI, this effect couples two remote electrical currents, which is called the magnon mediated current drag. From material point of view, a popular material for this purpose is yttrium iron garnet (YIG), a magnetic insulator (MI) and Pt and Ta as HM layers.

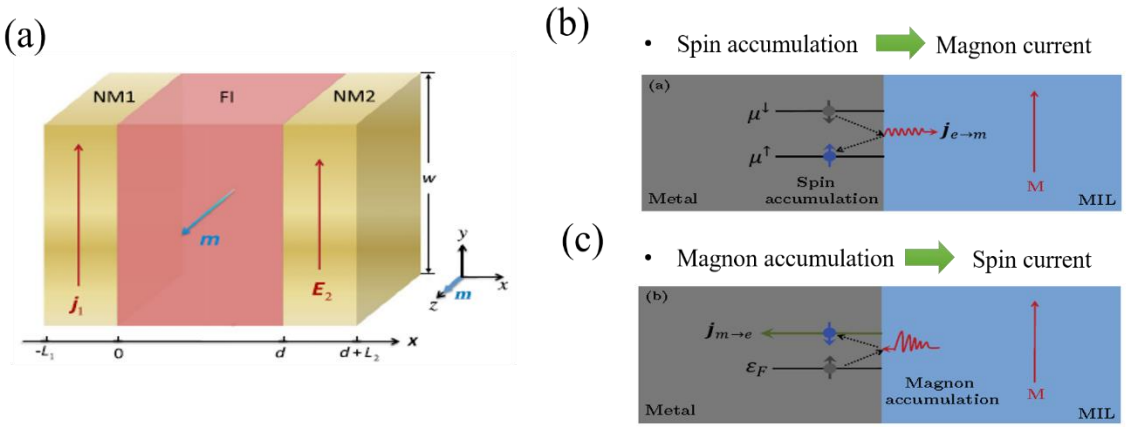

Figure 4- 1: Schematic illustration of magnon mediated electric current drag heterostructures. a) Schematics of the HM/FI/HM trilayer structure. b) Spin and magnon accumulation chart at the interface. Adapted from PRL. **109**, 096603 (2012) and PRB. **86**, 214424 (2012).

In this chapter, we demonstrate experimentally in a HM/MI/HM sandwich structure that these two types of pure spin currents are interconvertible across the interfaces,[2] realizing the magnon-mediated current drag effect.[1] The combined effects

allow transmitting an electrical signal across the MI. We show experimentally that the current drag signal can be switched "on" or "off" by controlling the magnetization orientation of MI with respect to the polarization of the spin current, analogous to conventional spin valves for spin-polarized charge current. The magnitude of the current drag signal scales linearly with the driving current without any threshold. Furthermore, the current drag signal follows the power-law T^n with *n* ranging from 1.5 to 2.5, which supports the magnon mediated mechanism in MI.

4.2 Physical Picture of Nonlocal Spin Transport

Our HM/MI/HM sandwich device structure is schematically shown in figures 4-2, (a and b). The MI is a thin YIG film sandwiched by either two identical HM films or dissimilar HM films. Via the SHE, a charge current ($J_{injected}$) injected in the bottom HM layer along the x-direction generates a pure spin current flowing in the z-direction with the spin polarization ($\boldsymbol{\sigma}$) parallel to the y-direction. The conduction electrons in the bottom HM interact with the localized moments of the MI via the *s-d* exchange interaction at the interface. The interaction can result in the creation or annihilation of magnons in the MI accompanied by spin-flips of conduction electrons in the bottom HM layer. Due to the nature of the *s-d* exchange interaction,[2,3] that is. $H_{sd} = -J_{sd} \sum \sigma . M$ where J_{sd} is exchange coupling strength, when the magnetization of the MI ($\boldsymbol{M}$) is collinear with $\boldsymbol{\sigma}$, magnons are created or annihilated depending on whether $\boldsymbol{M}$ is parallel

or anti-parallel to $\boldsymbol{\sigma}$. As such, the interaction creates a non-equilibrium magnon population and spin accumulation in the MI which drives magnon diffusion. In our devices, the YIG film thickness is much shorter than the magnon decay length, which leads to a significant non-equilibrium magnon population buildup at the top interface. The excess/deficient magnons are then converted to a conduction electron spin current in the top HM layer by the reverse process. The spin current is converted to a charge current $J_{induced}$ again in the top HM layer via the ISHE. When $\sigma \perp M$, there is no non-equilibrium magnon population or spin accumulation and the spin current is absorbed by the MI. Consequently, there is no induced spin or charge current in the top HM layer (figure 4-2, b). Remarkably, one can switch "on" or "off" the magnon creation/annihilation process by controlling the relative orientation between M and σ. Conceptually, this structure functions as a valve for pure spin current.

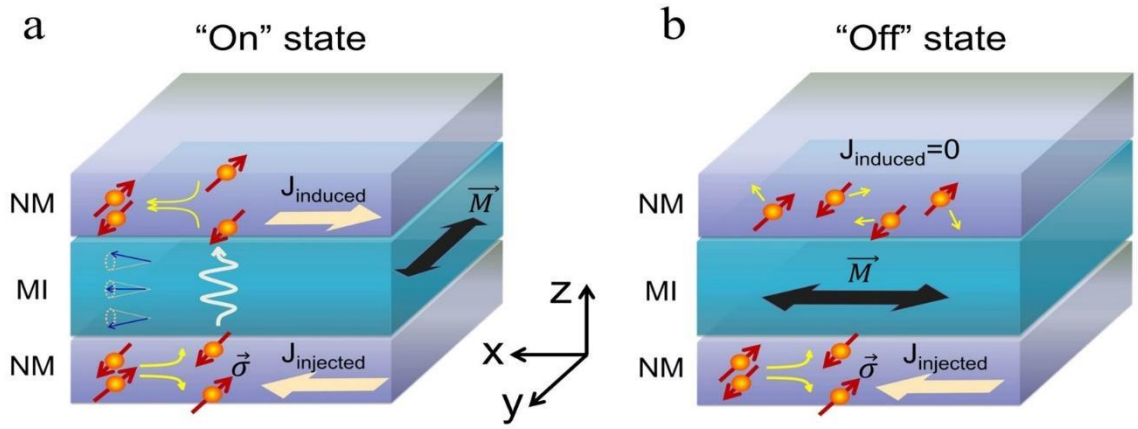

Figure 4- 2: Schematic illustration of magnon-mediated current drag effect heterostructures. a) The transmission of spin current is switched on. Magnetization (M) of magnetic insulator (MI) oriented collinearly with the spin polarization σ (//y) of the pure spin current in the bottom heavy metal (HM) layer generated by the spin Hall effect with an electric current ($J_{injected}$). The spin-flip scattering of conduction electrons at the bottom HM/MI interface can create ($M||-\sigma$) or annihilate ($M||-\sigma$) magnons. A non-equilibrium magnon population extends to the top MI/HM interface, and the spin angular momentum carried by magnons is transferred to conduction electrons in the top HM layer. The pure spin current flowing perpendicular to the HM layer is then converted to a charge current ($J_{induced}$) via the inverse spin Hall effect. (b) The transmission of spin current is switched off. M is perpendicular to the spin polarization σ of the spin current. In this geometry, the *s–d* exchange interaction between conduction electrons and local magnetic moments does not excite magnons in the MI. Consequently, there is no spin accumulation at the top MI/HM interface or induced charge current in the top HM layer.

4.3 Technical Procedure for Transport Measurement

For all transport measurements, the current was fed to the devices using a Keithley 2,400 d.c. current source, and the voltage was measured by a Keithley 2182A nano-voltmeter. The field dependence measurements were carried out using a closed-cycle system, while the angular dependent measurements were performed by a physical property measurement system equipped with a rotatory sample holder. For the nonlocal measurements, the excitation current in the bottom Pt is usually no more than 2 mA; for

the local magnetoresistance measurements, the current applied in top Pt and Ta was 1 mA, while the current used in bottom Pt is 10 mA. For the SSE measurements, the heating current applied in the top Au layer is 30 mA. In all the measurements, extra precaution was taken to ensure the correct polarity of both current and voltage.

4.4 Leakage Current Experiment of Trilayer Structures

Now, the physical picture and theoretical background is clear and the growth of GGG (110)/Pt/YIG/Pt(Ta) is prepared. Before we perform the experiment, we need to test the current leakage between two HM layers to make sure the middle layer of YIG is insulating. In this sandwich structures, we measured the resistance between top and bottom heavy metals (HMs). As illustrated in the inset of figure 4-3, we measured the resistance by applying a voltage between the top and bottom HMs and detecting the leakage current as a function of temperature. The voltage applied is 0.04 V, 0.7 V and 1.4 V from high to low temperatures. The voltage value at a given temperature was adjusted to avoid irreversible damage to the device. In figure 4-3, we found that the junction resistance increases rapidly with decreasing temperature and exceeds 20 GΩ for $T \leq 220K$, which is even larger than the input impedance of the nano-voltmeter (> 10 $G\Omega$ for Keithley 2182A), indicating that the shunting current in leakage produces a negligible voltage in the top HM layer via the magnetoresistance during the nonlocal measurements.

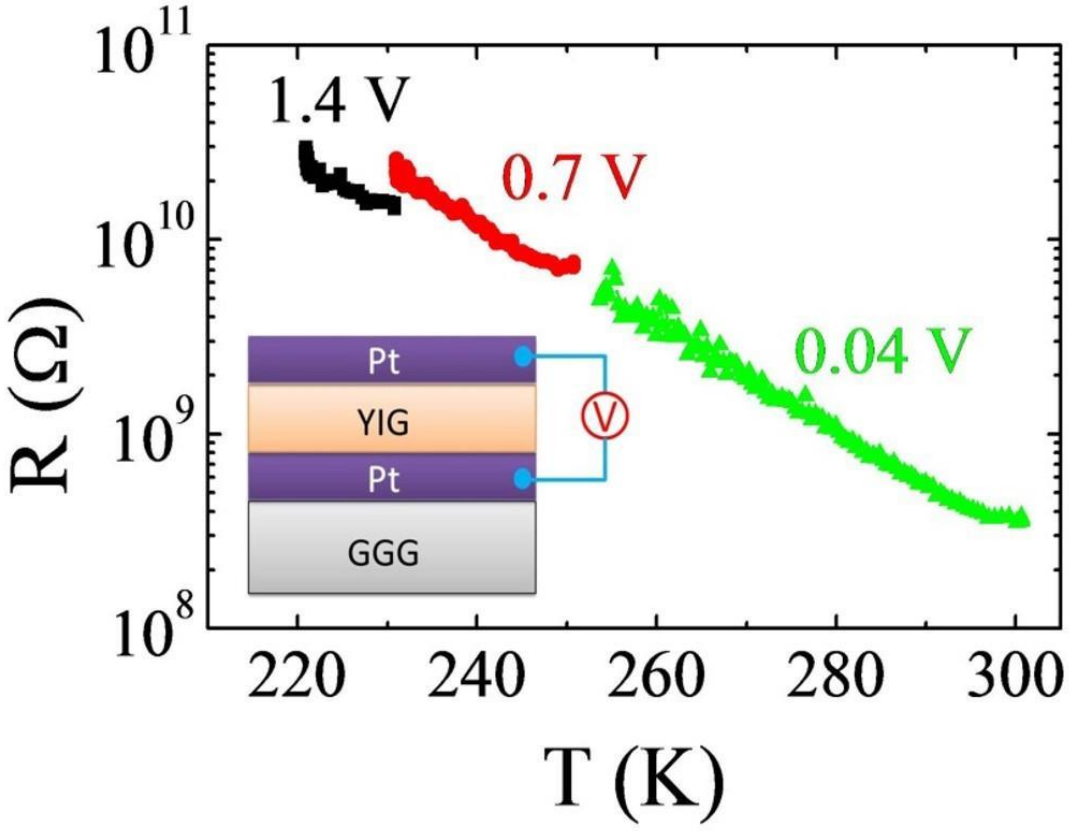

Figure 4- 3: Temperature dependence of the resistance between the top and bottom Pt layers. The thickness of YIG is 80 nm. The green, red and black curves are results taken under 0.04 V, 0.7 V, and 1.4 V bias voltages applied to the sandwich, as shown in the inset.

4.5 Field-Dependent Nonlocal Response in Trilayer Devices

Since both Pt and Ta have strong spin–orbit coupling with opposite signs in their spin Hall angle,[4,5,6] we have fabricated three Pt (5 nm)/YIG (80 nm)/Pt (5 nm) devices and two Pt (5 nm)/YIG (80 nm)/Ta (5 nm) reference samples, which were deposited on (110)-oriented $Gd_3Ga_5O_{12}$ (GGG) substrates (see chapter three for complete structure

growth by PLD and sputtering).[7, 8] As illustrated in figure 4-4, (a), the bottom Pt layer is used to inject current I_b, while the top layer, either Pt or Ta, functions as a detector to measure the induced current or the nonlocal voltage V_{nl}. An in-plane H is either swept in a fixed direction or rotated with a continuously varying angle of θ measured from the y-direction. We find that the high-quality YIG/Pt interface is essential to the observation of the spin current transmission. The excellent interface quality is verified by both the and the spin Hall magnetoresistance (SMR) in the same devices. The 80-nm-thick YIG films are nearly insulating but have small leakage at high temperatures. However, the resistance between the top and bottom HM layers increases exponentially as the temperature (T) decreases as shown in previous sub-section. Therefore, all the nonlocal measurements were performed below 220 K to avoid any parasitic signal from the small leakage current. In V_{nl}, we remove a non-zero background signal that exists even at $I_b = 0$. Figure 4-4, (b), optical image for the real device and Hall bar dimensions with specified connection of either current or voltage. Therefore, we use standard photolithography process to pattern a Hall bar with the channel width of 20 μm and the distance between two electrodes of 300 μm. Then the bottom Pt layer is deposited on the patterned Hall bar area by DC magnetron sputtering with 5 nm thick. For the top layer, we use standard e-beam lithography to define strip for the top Pt and Ta patterns right on top of the bottom Pt Hall bar channel with width of 2μm and length of 90 μm.

Figure 4-4, (c and d) plot the field dependence of V_{nl} at 220 K. When H is swept along I_b, that is, $\theta = 90^\circ$ (figure 4-4, c), V_{nl} is a constant at $I_b = 0$ (red). However, at I_b =+ 1.5 mA, V_{nl} shows a clear hysteresis with two positive peaks tracking the coercive fields

of the YIG film, indicating that V_{nl} is closely related to the magnetization state of YIG. As the I_b is reversed, V_{nl} also reverses the sign. In principle, a sign reversal can occur if there is a finite leakage current flowing in the top layer. Through the magnetoresistance, this current can produce a hysteretic voltage signal. Estimating from the leakage current, we find that the relative change in V_{nl} due to this effect is at least three orders of magnitude smaller than the observed nonlocal voltage signal. Note that V_{nl} (±1.5 mA) is the same as V_{nl} (0 mA) at the saturation state (H >200 Oe) when $\sigma \perp M$, suggesting that magnon creation/annihilation is totally suppressed. For the field sweeps with $\theta = 0$ (figure 4-4, d), $\boldsymbol{\sigma}$ is collinear with $\boldsymbol{M}$ at high fields, interface magnon creation/ annihilation results in a full current drag signal. Clearly, V_{nl} (+ 1.5 mA) is different from V_{nl} (0 mA) at the saturation fields and reverses the sign when I_b reverses. It is interesting to note that V_{nl} (±1.5 mA) differ from V_{nl} (0 mA) at the coercive fields. One would expect them to be the same since the average magnetization should point to the x-direction at the coercive fields, which would correspond to the saturation states for $\theta = 90^\circ$ in figure 4-4, (c). This discrepancy can be explained by the multi-domain state of YIG in which the actual $\boldsymbol{M}$ is distributed over a range of angles around $\theta = 90^\circ$, and the collinear component of $\boldsymbol{M}$ turns on the magnon channel and yields a nonzero V_{nl}. To investigate the phenomenon in the single-domain state, we perform the following experiments as explained in next sub-section.[8]

On the other hand, we need to distinguish the V_{nl} signal from longitudinal magnetoresistance. Therefore, we perform the measurement of Spin Hall magnetoresistance (SMR)[9,10,11] for the top Pt. In details, a charge current flowing in the

normal metal with strong spin-orbit coupling is converted into a spin current via SHE. The reflection and absorption of this spin current at the interface of the normal metal/magnetic insulator depends on the orientation of the magnetization (***M***) of the magnetic insulator. When ***M*** is collinear to the spin polarization ***σ,*** most of the spin current is reflected back and Pt resistance becomes smaller; in contrast, when ***M*** is perpendicular to the spin polarization of the spin current ($M \perp \sigma$), most of the spin current is absorbed by the insulator and the resistance becomes larger in Pt layer. This behaves as a dissipation channel; therefore, the resistance of the normal metal is larger than that for $M \parallel \sigma$. As a result, the degree of reflection or absorption of the spin current at the normal metal/magnetic insulator interface indicate excellent interface quality for spin current interconversion.

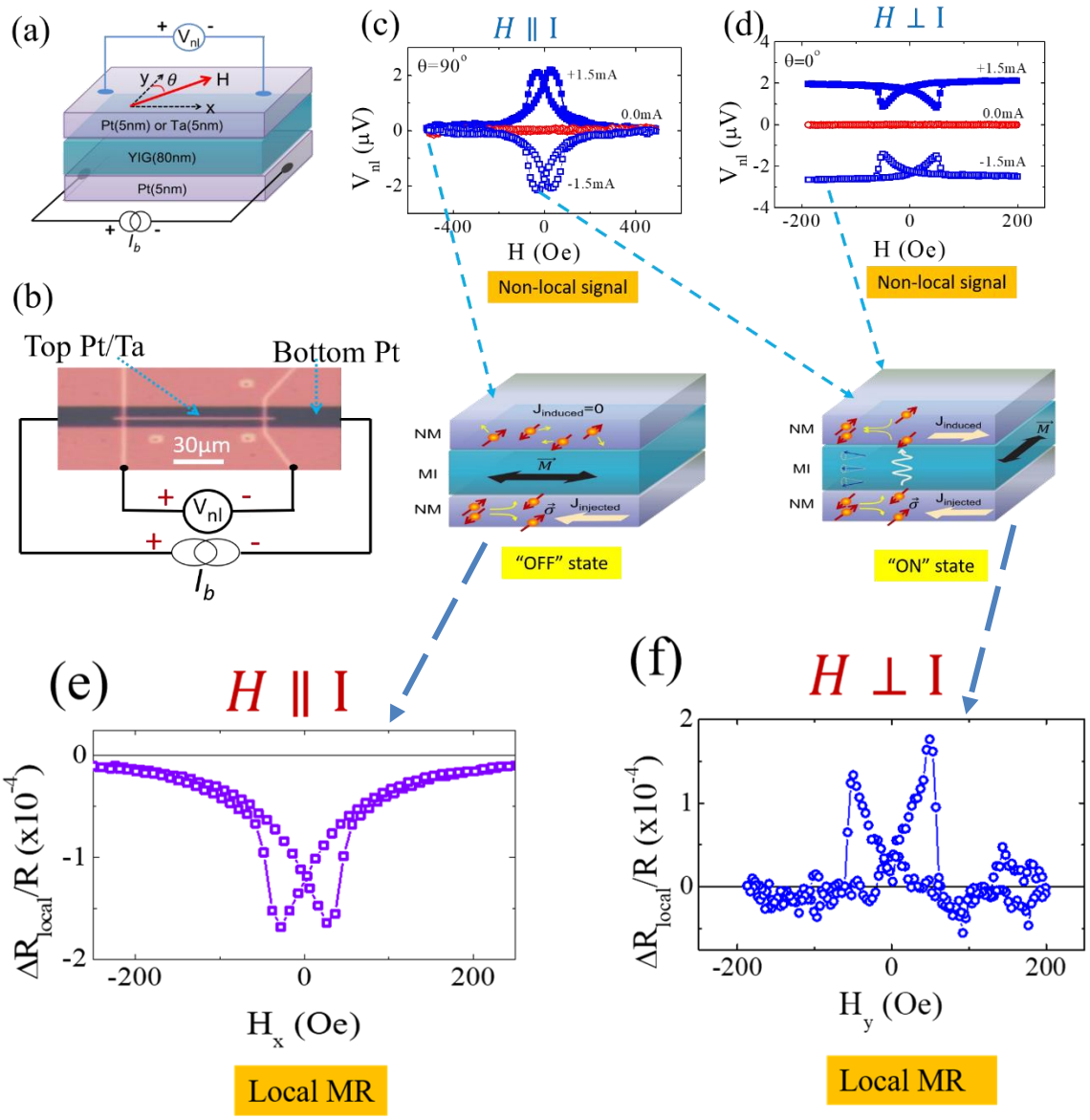

Figure 4- 4: Measurement geometry and field dependent nonlocal signal result. a) Schematic illustration of the experimental set-up. b) Optical image for the real device of both bottom Pt layer and top layer of either Pt or Ta. I_b is the current applied to the bottom Pt layer, and V_{nl} is the nonlocal voltage measured at the top layer along the I_b direction. The applied in plane magnetic field H makes an angle θ with the y-axis which is in plane and perpendicular to the current direction (x-axis). c) The field dependence of the nonlocal signal for H along I_b;i.e. θ = 90◦. d) The field dependent nonlocal signal with H perpendicular to I_b, i.e. θ = 90◦. e) SMR signal when magnetization M is collinear with spin polarization σ. f) SMR signal when magnetization M is perpendicular to spin polarization σ.

4.6 Angle-Dependent Nonlocal Response of Single Domain YIG

Figure 4-5, (a) presents V_{nl} in GGG/Pt/YIG/Pt as a function of θ between **M** and σ at 220 K, as illustrated in figure 4-5, (a). The 80 nm (110)-oriented YIG grown on Pt has a well-defined uniaxial anisotropy with an anisotropy field < 200 Oe. The applied magnetic field (1000 Oe) is sufficiently strong not only to set YIG into a single-domain state, but also to rotate **M** with it. For all positive I_b (solid symbols), V_{nl} exhibits maxima at θ = 0º and 180º (**M** collinear with σ), but minima at $\theta = 90^o$ and 270^0 ($M \perp \sigma$). V_{nl} changes the sign as I_b is reversed (empty symbols). At $\theta = 90^o$ and 270^0, the nonlocal signal for $\pm I_b$ coincides with V_{nl} (0 mA), further validating that the spin current is in the off state when $M \perp \sigma$. Similar angular dependent measurements are also taken on a GGG/Pt/YIG/Ta device and the results are depicted in figure 4-5, (d). For the same measurement geometry and the same polarity of I_b, we find that V_{nl} of GGG/Pt/YIG/Ta has the opposite sign to that of GGG/Pt/YIG/Pt, which is just expected from the opposite signs in their spin Hall angle. The V_{nl} sign difference here is another piece of critical evidence for the magnon mediated mechanism, as opposed to other extrinsic ones such as leakage.

An interesting feature to note here is that V_{nl} at $\theta = 0^o$ and 180^o shows a slight but reproducible difference which is independent of the current polarity but increases with the increasing magnitude of I_b. We attribute this phenomenon to the SSE contribution since the joule heating in the bottom Pt layer unavoidably generates a small vertical temperature gradient, which in turn launches an upward spin current in YIG entering the

top Pt (or Ta) layer. As **M** reverses, so does the spin polarization, which consequently produces two different SSE signal levels between $\theta = 0^o$ and 180^o. Combining these two effects, we can fit the angular dependence data using:

$$V_{nl} = V_0 + V_{SSE}\cos\theta + V_{Drag}\cos^2\theta \quad (1)$$

where V_0 is an offset voltage insensitive to the magnetization orientation, V_{SSE} is the SSE voltage amplitude, and V_{Drag} represents the amplitude of the current drag signal. The solid red curves in figures 4-5, (a) and 4-5, (d) fit the experimental data remarkably well, and the extracted fitting results are plotted in figures 4-5, (b) and 4-5, (e) for GGG/Pt/YIG/Pt and GGG/Pt/YIG/Ta devices, respectively. Two conclusions can be evidently drawn from these results. [8] First, the magnitude of the current drag signal (red cycles) scales linearly with the driving current, i.e. $V_{Drag} \propto \mathrm{I}_b$. This is in stark contrast with the highly nonlinear behavior. Second, the weak current dependence of the SSE contribution follows $V_{SSE} \propto I_b^2$ (as shown in figures 4-5, (b) and 4-5, (e)), which is characteristic of thermoelectric effects.

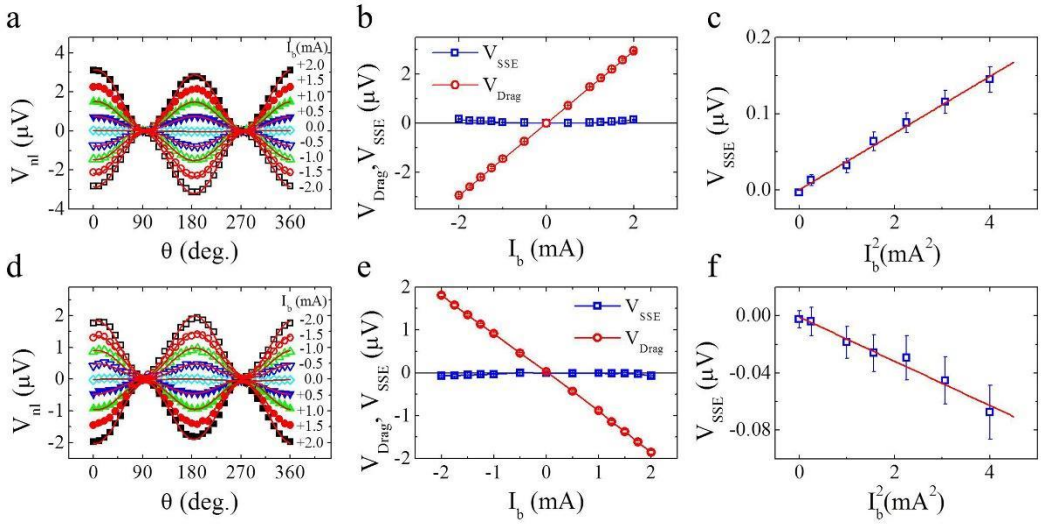

Figure 4- 5: Angular and current dependence of nonlocal signal. a) and d) are angular dependence of nonlocal signal at different currents in the bottom Pt layer for GGG/Pt/YIG/Pt and GGG/Pt/YIG/Ta, respectively. The magnetic field is fixed at 1000 Oe and rotated in plane. In a) and d), solid symbols indicate positive I_b, and empty symbols indicate negative I_b. Red curves are the fits using equation (1). b) and e) show the I_b- dependence of the current drag signal (V_{Drag}) and the spin Seebeck signal (V_{SSE}) for GGG/Pt/YIG/Pt and GGG/Pt/YIG/Ta, respectively. c) and f) are the spin Seebeck signal as a function of I_b^2 for GGG/Pt/YIG/Pt and GGG/Pt/YIG/Ta, respectively, the red curves are the linear fits. The error bars are from fitting using equation (1) in a) and d).

4.7 Temperature Dependence of Nonlocal Responses

According to Zhang, *et al.*,[2] the temperature dependence of the injection interface spin convertance G_{em} is $\left(\frac{T}{T_c}\right)^{3/2}$, where T_c is the Curie temperature of the MI; for the detection interface, the spin convertance G_{me} is proportional to $\frac{T}{T_F}$, where T_F is the Fermi temperature of the HM layer. In the most simplified picture which is strictly applicable only for very thick films, the current drag signal should be proportional to the

product of the two spin current convertances, i.e. $V_{Drag} \propto G_{em} \cdot G_{me} \propto T^{5/2}$. The representative angular dependence measurements below 220 K are shown in figures 4-6, (a) and 4-6, (c) for GGG/Pt/YIG/Pt and GGG/Pt/YIG/Ta devices, respectively. For both samples, I_b is set at +2 mA and H is held at 1000 Oe. The magnitude of the current drag signal decreases progressively with decreasing temperature for both devices. By fitting V_{nl} using Equation (1), we extract the magnitude of V_{Drag} and V_{SSE} shown in figures 4-6, (b) and 4-6, (d). Apart from the expected sign difference, the magnitude of V_{Drag} in both devices monotonically decreases with decreasing temperature. In fact, both data sets can be well fitted by a power-law $V_{Drag} = V_{Drag}^{0} T^{n}$ (red solid curves in figures 4-6, (b) and 4-6, (d)), where V_{Drag}^{0} is a pre-factor. The extracted exponent n is 2.21 for GGG/Pt/YIG/Pt and 1.88 for GGG/Pt/YIG/Ta, falling in the range between 1.5 and 2.5. It should be pointed out that the full picture described in Ref. 24 actually contains other quantities that have weak temperature dependence. The deviation of the exponent from 2.5 is fully expected if these factors are considered. On the other hand, the V_{SSE} is found to be relatively insensitive to temperature, suggesting a completely different mechanism.

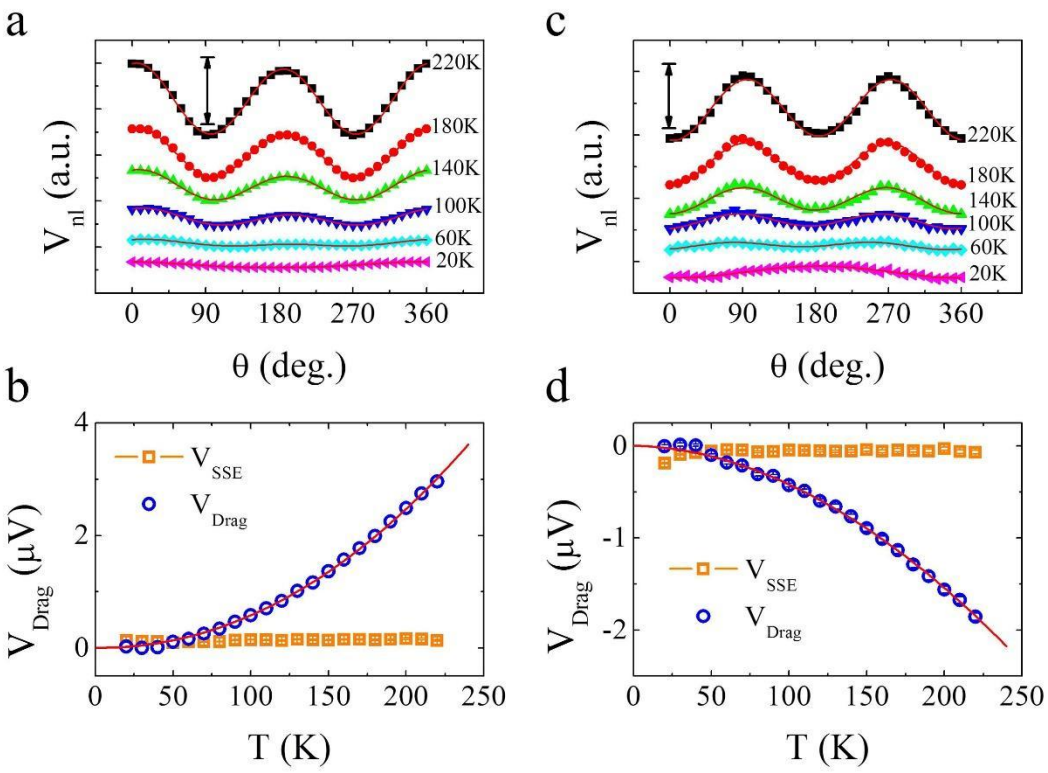

Figure 4- 6: Temperature dependence of nonlocal signal. a) and c) are angular dependence of the nonlocal signal at different temperatures for GGG/Pt/YIG/Pt and GGG/Pt/YIG/Ta, respectively. During the measurements, I_b was fixed at +2 mA. The curves are vertically shifted for clarity, the black arrows in a) and c) represent the magnitude scale of 2.80 $\boldsymbol{\mu V}$ and 1.98 $\boldsymbol{\mu V}$, respectively. Red solid curves in a) and c) are the fits using equation (1). b) and d) are the temperature dependence of the extracted current drag signal (V_{Drag}) and spin Seebeck signal (V_{SSE}) for GGG/Pt/YIG/Pt and GGG/Pt/YIG/Ta, respectively. Red solid curves in b) and d) are the fits using $V_{Drag} = V_{Drag}^{0} T^{n}$, here, n=2.21 for the GGG/Pt/YIG/Pt device, and n=1.88 for the GGG/Pt/YIG/Ta device.

4.8 Longitudinal Spin Seebeck Effect (SSE)

We confirmed the transmission of thermally excited spin currents through the HM/YIG interface by performing the longitudinal spin Seebeck effect (SSE [12]) in our sandwich structures. On top of the sandwich structures, we first deposited 300 nm Al_2O_3, used to electrically insulate the device, and the top heater layer consists of 5 nm Cr and 50 nm Au. When a charge current (30 mA) is applied to the Cr/Au layer, a temperature gradient is established in the z-direction by joule heating, as shown in figure 4-7, (a). During the SSE measurements, a magnetic field was applied in the y-direction while the voltage is detected along the x-direction. We plot the field dependence of the longitudinal spin Seebeck signal at 220 K, which is normalized to the device length as seen in figure 4-7, (b). First, all three metal layers show strong SSE signals. Second, we found that the magnitude of the SSE signal from the bottom Pt is on the same order as that from the top Pt layer. Third, we notice that the SSE signal from the top Ta shows the opposite sign to that from Pt, which can be accounted for by the fact that Pt and Ta have opposite spin Hall angles. Therefore, we have confirmed the excellence interface quality for transmitting thermally excited spin currents.

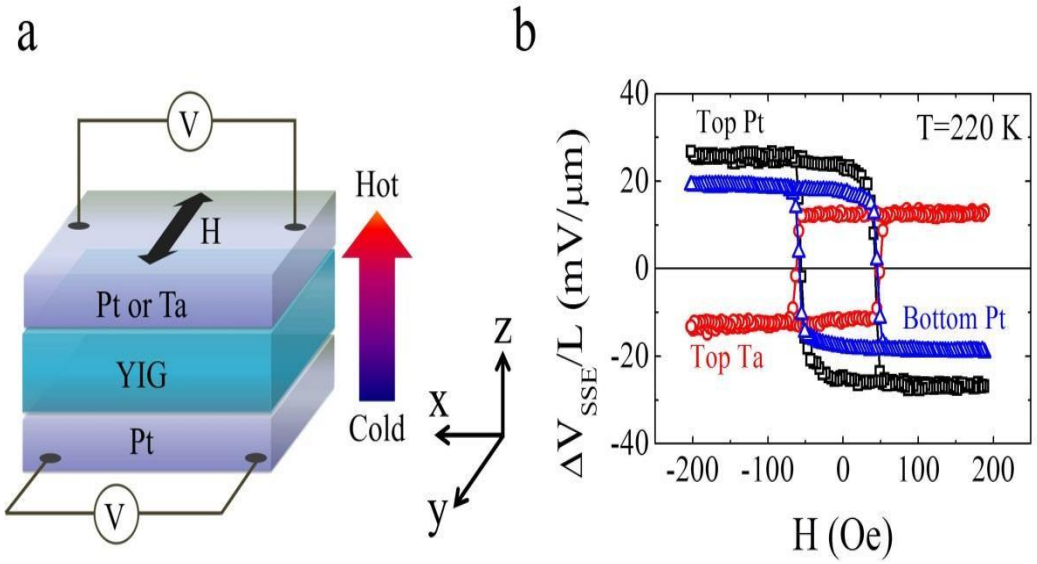

Figure 4- 7: Longitudinal spin Seebeck effect in our devices. a) Schematic illustration of longitudinal spin Seebeck effect measurement set-up. A temperature gradient was generated along the z-direction by a heater on top. Voltages of the top layer and bottom layers were measured in the x-direction with the magnetic field sweeping in the y-direction. b) SSE signals, normalized to the detecting stripe length L of the top Pt, top Ta and bottom Pt layers as a function of the magnetic field at T=220 K.

References:

1. Zhang, S.S.L. & Zhang, S. Magnon Mediated Electric Current Drag Across a Ferromagnetic Insulator Layer. *Physical Review Letters* **109**, 096603 (2012).

2. Zhang, S.S.L. & Zhang, S. Spin convertance at magnetic interfaces. *Physical Review B* **86**, 214424 (2012).

3. Takahashi, S., Saitoh, E. & Maekawa, S. Spin current through a normal-metal/insulating-ferromagnet junction. *Journal of Physics: Conference Series* **200**, 062030 (2010).

4. Liu, L. et al. Spin-Torque Switching with the Giant Spin Hall Effect of Tantalum. *Science* **336**, 555-558 (2012).

5. Tanaka, T. et al. Intrinsic spin Hall effect and orbital Hall effect in $4d$ and $5d$ transition metals. *Physical Review B* **77**, 165117 (2008).

6. Morota, M. et al. Indication of intrinsic spin Hall effect in $4d$ and $5d$ transition metals. *Physical Review B* **83**, 174405 (2011).

7. Aldosary, M. et al. Platinum/yttrium iron garnet inverted structures for spin current transport. *Applied Physics Letters* **108**, 242401 (2016).

8. Li, J. et al. Observation of magnon-mediated current drag in Pt/yttrium iron garnet/Pt(Ta) trilayers. *Nature Communications* **7**, 10858 (2016).

9. Nakayama, H. et al. Spin Hall Magnetoresistance Induced by a Nonequilibrium Proximity Effect. *Physical Review Letters* **110**, 206601 (2013).

10. Chen, Y.-T. et al. Theory of spin Hall magnetoresistance. *Physical Review B* **87**, 144411 (2013).

11. Lin, T., Tang, C., Alyahayaei, H.M. & Shi, J. Experimental Investigation of the Nature of the Magnetoresistance Effects in Pd-YIG Hybrid Structures. *Physical Review Letters* **113**, 037203 (2014).

12. Uchida, K. et al. Spin Seebeck insulator. *Nature Materials* **9**, 894 (2010).

Chapter 5

Giant Magnetoresistance (GMR) Effect Study in Magnetic Insulator Thin Films

5.1 Brief Background of GMR

Giant magnetoresistance (GMR), discovered in 1988 in independent and simultaneous work of both Fe/Cr superlattices structure and Fe/Cr/Fe trilayers,[2,3] is one of the most intriguing discoveries in both nanoscale magnetism and thin film deposition techniques as it combines fundamental physics with practical uses in technology.[1] Within a decade of its discovery, commercial technologies had become available in the market such as magnetic memory, magnetic sensors and hard-disk read-heads.[4] This effect is so important that for its discovery the shared 2007 Noble prize for physics was awarded to Albert Fert and Peter Grunberg.

GMR defines as a drastic change in electrical resistance with response to an applied magnetic field that arises when the relative magnetization orientations of successive ferromagnetic (FM) layers, with non-magnetic metal (NM) layers as spacers between each FM later, are in an anti-parallel configuration.[5] With increasing magnetic field, this anti-parallel configuration changes gradually as the magnetization in every layer rotates towards the magnetic field direction until reaching saturation with all the layers aligned resulting in a drop in resistance. Another important factor here is the coupling which can be either ferromagnetic or antiferromagnetic, between the (FM)

multilayers and (NM) spacers as the interlayer exchange coupling is mediated by itinerant electrons although it is not a necessary condition for GMR to occur.[1] An important condition for GMR to occur is the NM spacer thickness. It needs to be thick enough to decouple the two magnetic layers in order to create an anti-parallel state; however, to maximize the GMR effect, it must be thinner than the mean free path (average distance an electron travels before being scattered) of conduction electrons. This anti-parallel alignment of magnetization can also be engineered through different coercivities of the alternating magnetic layers or by introducing spin valve geometry when one layer is pinned with adjacent antiferromagnetic layer whereas the magnetization of the other layer is free to rotate with magnetic field.[6]

To distinguish GMR from other magnetoresistances (MR), GMR is larger by at least two orders of magnitude than other types of MR such as (AMR). Addition to that, GMR arises from magnetic orientation configuration rather than from the orientation of magnetic field with respect to the electric current direction.[7]

The first experimental observation of GMR was in single crystalline (100)-oriented Cr/Fe multilayers and (100)-oriented Fe/Cr/Fe sandwiches structures with antiferromagnetic interlayer exchange by Baibich *et al.* and Binasch *et al.* respectively with current in-plane (CIP) geometry.[2,3] These films were grown by molecular beam epitaxy (MBE). As seen in figure 5-1, (a) for Cr/Fe superlattices, the normalized GMR ratio is highest when the neighboring Fe layers are coupled anti-parallel at zero magnetic field with a decrease of ~ 50% at 4.2 K in the saturation state at ~ 20 kOe for a device with 60 repeats with the unit of Fe (3 nm)/Cr (0.9 nm). For Fe/Cr/Fe trilayers, when the

thickness of Fe layers is 25 nm and Cr is 1 nm, the GMR ratio is ~ 1.5% at room temperature as seen in figure 5-1, (b). This ratio can be increased to 3% as Fe layers thickness is decreased to 8 nm. Further research showed that GMR can be realized in different ferromagnetic materials such as polycrystalline Fe/Cr and Co/Cu multilayers grown by D.C. sputtering.[8,9] Based on that, GMR appears to be a general phenomenon which occurs in many combinations of the FM/NM structures..

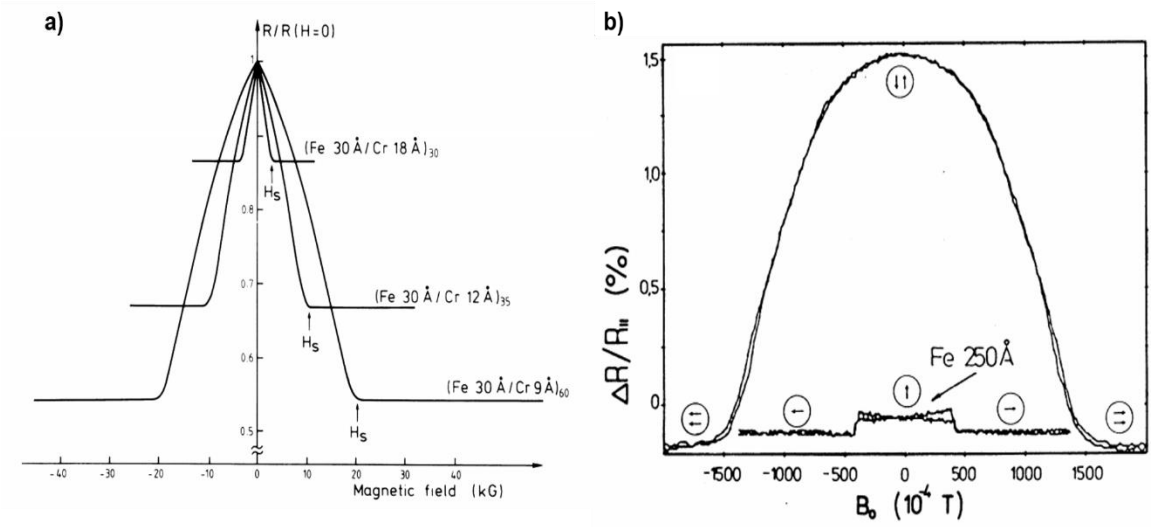

Figure 5- 1: Normalized GMR resistance versus applied magnetic field for several Fe/Cr multilayers and Fe/Cr/Fe trilayers. a) GMR ratio for Fe/Cr multilayers with several thicknesses of antiferromagnetic coupling at 4.2K. Arrows indicate the saturation field HS, which is required to overcome the antiferromagnetic interlayer coupling between the Fe layers and align their magnetizations parallel. b) GMR ratio for Fe/Cr/Fe trilayers at room temperature. Adapted from Phys. Rev. Lett. 61, 2472 (1988) and Phys. Rev. B 39, 4828(R) (1989).

The main physical process that is responsible for GMR is spin-dependent scattering of the conduction electrons.[1] Due to the density of states in ferromagnetic metals, scattering rates for spin-up and spin-down are quite different, and therefore, the resistance for each configuration is different. To understand the GMR mechanism, we

need to map the trajectories of both the spin-up ($s_z = +\frac{1}{2}$) and spin-down ($s_z = -\frac{1}{2}$) electrons for the two different relative magnetization configurations based on the spin-dependent scattering. For the case when the magnetizations of all the FM layers are parallel to the magnetic field, as depicted in figure 5-2, (a), the spin-up electrons pass through the structure unscattered since their spin is parallel to the magnetization of the layers whereas for spin-down electrons, spin is anti-parallel to magnetization and therefore those electrons scatter strongly in both FM layers.[4] In this two spin channel model, the resistance in parallel geometry is determined mainly by spin-up electrons providing low value. On the contrary, for the second case of antiferromagnetic magnetization, both spin-up and spin down electrons are strongly scattered as seen in figure 5-2, (b) in one of the FM layers due to their spin is opposite to that layer's magnetization. As a result, the total resistance of the multilayers is high.

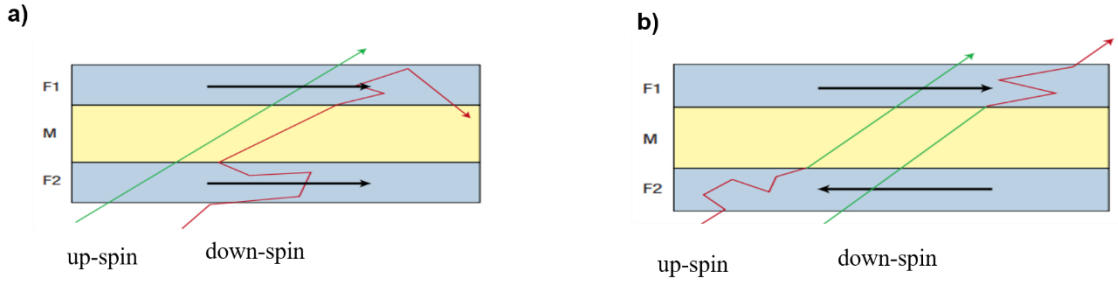

Figure 5- 2: Spin valve structure with schematic representation of GMR effect mechanism in two identical ferromagnetic (FM) layers denoted as F1 and F2 separated by non-magnetic metal spacer layer M with current in-plane (CIP) geometry. a) Schematic illustration of electron transport for parallel magnetization direction as indicated by black arrows. Up-spin electrons can travel through the both FM layers almost without scattering because they are parallel to the magnetization of the layers. Whereas the down-spin electrons are strongly scattered in both FM layers.in this case, the total resistance for both layers is low due to conduction occurrence in parallel for the two spin channels. b) Both up-spin and down-spin electrons are strongly scattered with one of FM layers giving rise to a higher overall resistance in the multilayers structure. Adapted from *Nature Materials* **6**, 813–823 (2007).

In this chapter, we present a GMR study in a spin valve-like structure consisting of a thin film of two identical layers of magnetic insulating YIG separated by a NM spacer layer of either Pt or Au. The first half will briefly mention the growth procedure for the trilayer structures consisting of two layers of 20 nm thick YIG by a Pt layer with varying thickness. It turns out that for the YIG/Pt/YIG structure, we could not achieve GMR due to different reasons as they will be explained through the chapter. On the other hand, the second half will focus on the YIG/Au/YIG structure where GMR is observed. It is also confirmed by spin Seebeck measurements as the contribution from each layer is observed.

5.2 Spin Valve Structure in thin films of YIG/Pt/ YIG

Background introduction for GMR is dedicated to ferromagnetic metals (FM). Different FM combinations can be used with also different non-magnetic metal layer(NM). Furthermore, for those FM materials, the transport measurements can be carried out through current-in-the-plane (CIP) and current perpendicular-to-the-plane (CPP) geometries. In this section, we investigate GMR in a magnetic insulator YIG thin film in which the applied current is confined to a conductive NM providing a clean experiment to study the interface scattering effect of conduction electrons. Another important difference with this system vs. structures that utilize metallic FM is that we can

only do the electrical measurements via CIP geometry but not CPP because the current cannot propagate in perpendicular direction due to the insulating behavior of YIG.

5.2.1 Growth and Magnetization of YIG/Pt/YIG

The spin valve structure use in this study is shown in figure 5-3, (a) and consists of two identical ferrimagnetic layers (YIG) separated by NM layer (Pt). As explained in chapter two, YIG grown on lattice constant matched GGG is epitaxial with layer-by-layer growth mode. We choose GGG, with orientation of (110), as substrate to grow the spin valve structure. To grow the bottom YIG layer, we stick with the recipe in chapter two to obtain high quality thin film with ultra-smooth surface morphology. It is also known from chapter two that YIG grown under these conditions is single crystalline as confirmed by RHEED pattern and HRTEM.[11] For the NM layer, we use D.C. sputtering to deposit different thickness of Pt using the same recipe described in chapter three. Pt thickness of 2, 3, 5, and 10 nm are examined in different samples in order to satisfy the necessary conditions required to achieve GMR. After that, we insert the sample again into the PLD chamber to grow the second layer of YIG. The growth is carried out at ~ 450 ˚C and subsequent annealing using RTA with temperatures between 800 and 850 ˚C for 200 s is implemented in order to crystalize and acquire magnetic order. More details of the growth procedure is discussed in chapter three.[12] The thickness of either the bottom or top YIG layer is fixed to 20 nm. After annealing, we put it back into the PLD chamber to probe the crystallinity of the three layers. As shown in figure 5-3, (b), the RHEED beam

is directed parallel to <111> direction of the substrate providing a clear streaky pattern confirming that all bottom YIG, Pt and top YIG layers are in the single crystal phase. The Pt thickness is 5 nm for this sample.

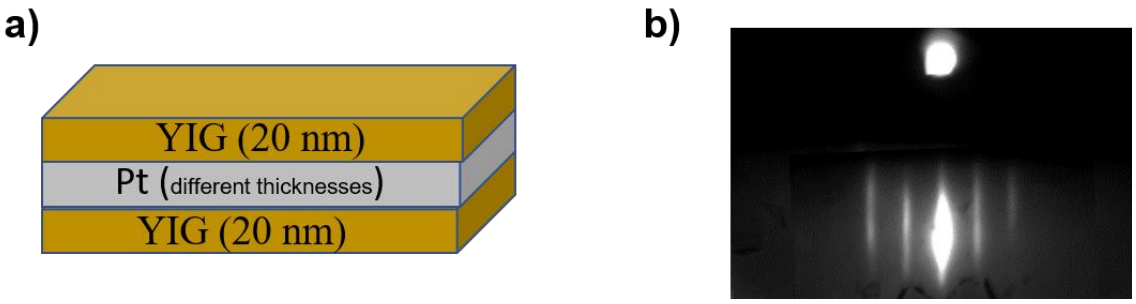

Figure 5- 3: Spin valve structure and RHEED pattern for the whole multilayers. a) Spin valve structure consists of bottom layer of YIG thin film with 20 nm thick, Pt layer with varying the thickness to satisfy GMR effect conditions and top layer of YIG with again 20 nm thick. b) RHEED pattern for three layers giving clear streaky pattern confirming high quality growth of this spin valve structure.

After confirming the high growth quality for each layer, VSM measurement is performed at room temperature as a first step towards realization of different magnetization behavior between the bottom and top layer of YIG. Three conditions are required for GMR: magnetic order in the bottom and top YIG layers, very weak interlayer coupling and an anti-parallel state of the magnetization in different layers. Growth of YIG directly on GGG yields an in plane magnetic anisotropy showing easy axis hysteresis loop with coercive field between 1 to 5 Oe as depicted in figure 5-4, (a).[11] Magnetization of YIG grown on 5 nm thick Pt as discussed in detail in chapter three shows similar behavior as YIG on GGG, but with a coercive field increased by six times as shown in figure 5-4, (b).[12] In principle, based on this result, the bottom and top YIG

layers should have different coercivities and indeed they have as seen in figure 5-4 (c). This difference creates the anti-parallel state of magnetization with coercive field from ~ 25 to ~ 40 Oe satisfying first prerequisite condition towards GMR. However, Pt thickness is critical for decoupling the two YIG layers, otherwise, they will switch together at the same field. After testing different thicknesses of the Pt spacer, we find that below 5 nm the interlayer coupling is large with YIG layers switching together until the thickness is 5 nm which is the minimum thickness for decoupling.

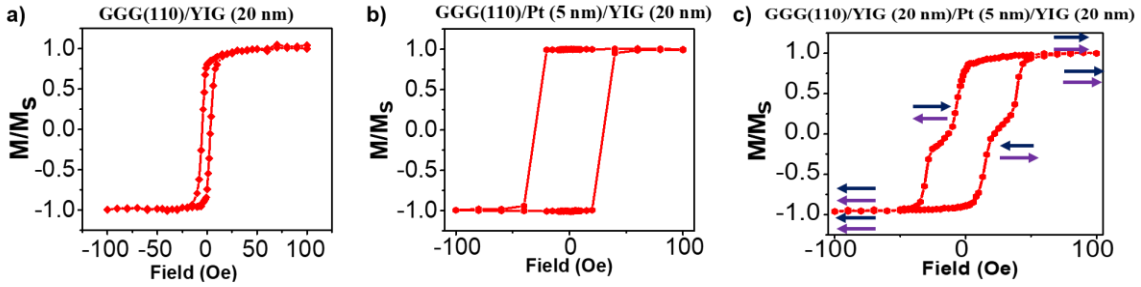

Figure 5- 4: VSM measurements for spontaneous magnetization for YIG grown directly on YIG, on Pt and on Pt/YIG. a) YIG grown directly on GGG (110) showing soft magnetization behavior with average coercive field of ~ 4 Oe. b) YIG grown on 5 nm Pt and showing soft magnetization in plane configuration with larger coercive field of ~ 40 Oe. c) Trilayers magnetization behavior where the anti-parallel magnetization state is observed between the bottom and top layers of YIG.

5.2.2 Magneto-Transport Measurements

Based on VSM results confirming that both 5 and 10 nm thick Pt as spacer show anti-parallel magnetization state, I will present longitudinal magnetoresistance (MR) measurements for 5 nm thick Pt. Also, 10 nm Pt shows similar behavior and results of MR as 5 nm, therefore, I will not include it in this thesis. With respect to the MR measurements, we can only use CIP geometry and do both current perpendicular (I $\perp$ H)

and parallel (I // H) to the magnetic field to measure the resistance in the Pt layer as a function of magnetic field. Let's remind ourselves that the simple test of GMR is to observe high resistance behavior within the antiparallel state and then a decrease towards the minimum value obtained when both YIG magnetizations are fully aligned with high magnetic field.

Before doing the electrical measurements, we etch the top YIG and Pt layers into Hall-bar geometry with well-defined width and length using inductively coupled plasma (ICP) etching. As depicted in figure 5-5, (a), we apply charge current in x-direction, magnetic field in y-direction and measure the response in resistance to the changing magnetic field. After that, we rotate the sample 90° to apply current and magnetic field in x-direction as seen in figure 5-5, (b). The MR ratio ($\Delta R/R$) for the perpendicular geometry (I $\perp$ H) at room temperature is shown in figure 5-6, (b) with two peaks resembling the YIG coercivities with resistance higher than at saturation giving a good indication of GMR behavior. However, by rotating the sample 90°, the MR is reversed with two dips as shown in figure 5-6, (c) which excludes GMR since we should see higher resistance when the anti-parallel magnetization state is achieved. The explanation of what we see is related to spin Hall magnetoresistance (SMR) and anisotropic magnetoresistance not GMR. The signal depends on spin polarization $\boldsymbol{\sigma}$ being either perpendicular to magnetization ($\sigma \perp M$) and therefore the spin current is absorbed by the magnetic moments in the YIG layers leading to a higher resistance at the coercive field as seen in figure 5-6, (b), or ($\sigma // M$) in which the spin current is reflected back at the interface providing more charge current and thus a smaller resistance at the coercive field as seen

in figure 5-6, (c).[13] Moreover, we track the MR response as a function of the magnetic field for both geometries at lower temperatures of 200 150, and 100 K. And the result is still peaks for the (I ⊥ H) geometry and dips for the (I // H) geometry at the coercive field. The conclusion the YIG/Pt/YIG spin-valve for 5 and 10 nm Pt thicknesses is that we did not observe GMR even though we were able to confirm the necessary anti-parallel magnetization state is obtained by VSM. We believe the reason behind this is that the spin diffusion length in Pt is small (~ 1.5 nm at room temperature) and thus the electron spin loses its status it obtains from being scattered from one YIG/Pt interface before reaching the other.

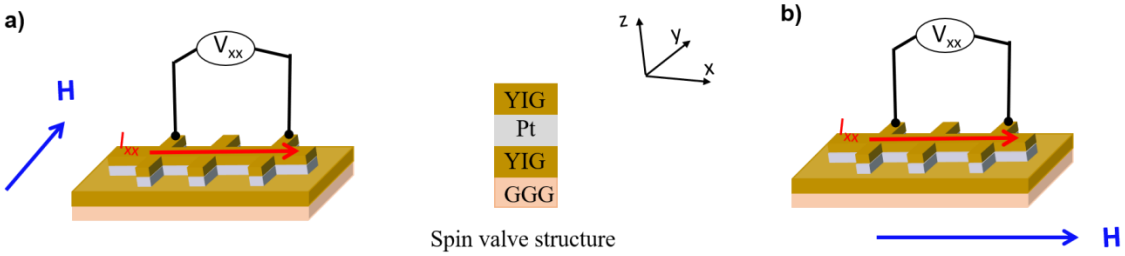

Figure 5- 5: Systematic drawing of the longitudinal magnetoresistance (MR) measurement geometries in spin valve structure with the top layer of YIG and Pt etched by ICP without etching the bottom layer of YIG. a) Illustration of MR measurement geometry with current applied in x-direction and magnetic field applied in y-direction. b) Illustration of MR measurement geometry with current and magnetic field applied in x-direction. MR is detected between two electrodes in x-directions.

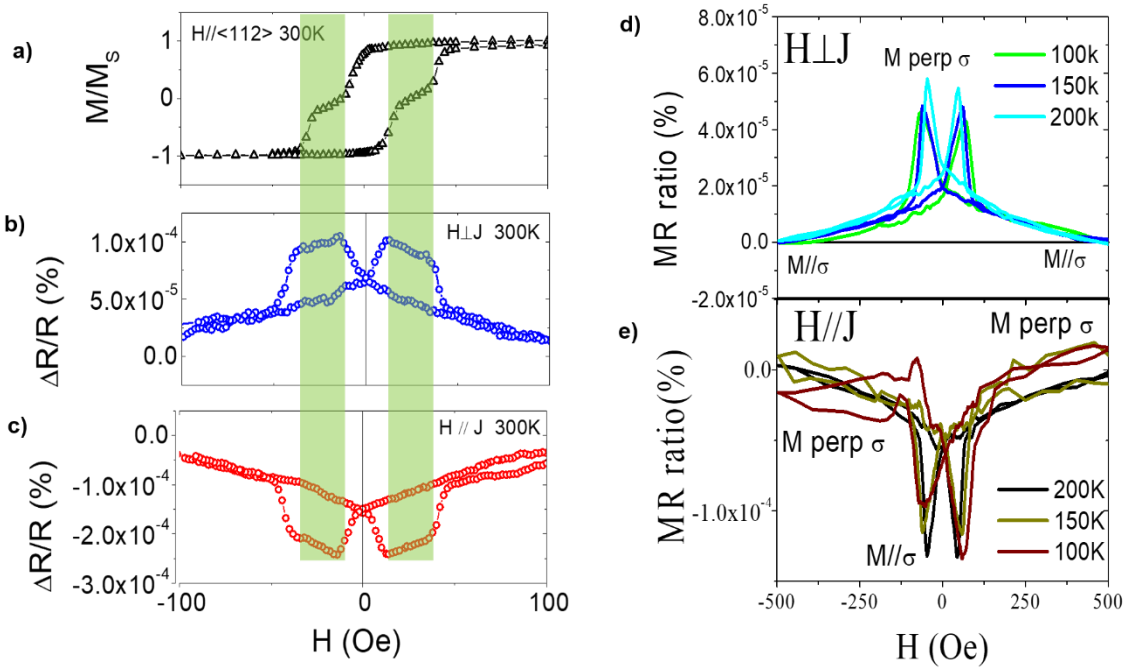

Figure 5- 6: Longitudinal magnetoresistance ratio (*ΔR/R*) for both current perpendicular and parallel to the applied magnetics geometries for different temperatures. a) Magnetic hysteresis loop measured by VSM at room temperature showing anti-parallel magnetization state between the bottom and top YIG layers. b) *ΔR/R* ratio as a function of applied magnetic field for current perpendicular to magnetic field at room temperature. c) *ΔR/R* ratio as a function of applied magnetic field for current parallel to magnetic field at room temperature. d) *ΔR/R* ratio as a function of applied magnetic field for current perpendicular to magnetic field at 200, 150, 100 K. e) *ΔR/R* ratio as a function of applied magnetic field for current parallel to magnetic field at 200, 150, 100 K.

5.2.3 Longitudinal Spin Seebeck Effect

We perform LSSE measurements to determine whether the results agree or disagree with our longitudinal MR results from the previous section in terms of identifying separate contribution from each YIG layer. Besides that, we need to confirm the quality of the two interfaces via the thermal excitation of spin currents generated through each YIG layer as consequence of the vertical temperature gradient (∇T). In the LSSE experiment, the spin value structure is YIG (20 nm)/Pt (5nm)/YIG (20 nm) and, on

top of the that, we deposited 300 nm Al_2O_3, used to electrically insulate the device followed by the top heater layer which consists of 5 nm Cr and 50 nm Au as shown in figure 5-7, (a). When a charge current (100 mA) is applied to the Cr/Au layer, a temperature gradient is established in the z-direction by joule heating, as shown again in figure 5-7, (a). During the SSE measurements, a magnetic field is applied in the y-direction while the voltage is detected along the x-direction. We plot the field dependence of the LSSE signal at room temperature and 50 K to identify if there is any behavior difference such as obvious contribution from each layer. To be clearer, it might be difficult to see the different contributions at room temperature (RT) as the two coercivities merge whereas the coercive fields become larger at low temperature such that the anti-parallel state can be resolved. From the result shown in figure 5-7, (b and c), there exists a strong SSE signal without observing the individual contribution from each layer. Comparing the signal at 300K to 50K, the magnitude is smaller as expected and coercivity is larger due to the anisotropy being increased for YIG layers. From our LSSE study we confirmed that the thermally excited spin currents are detected via ISHE supporting excellent interface quality. Moreover, the SSE signal is similar to longitudinal MR data as we did not observe an anti-parallel magnetization state between the two YIG layers. To mention again, the same structure with 10 nm Pt thickness in between shows the same results as for the device with 5 nm Pt as we did not identify the contribution from each YIG layer.

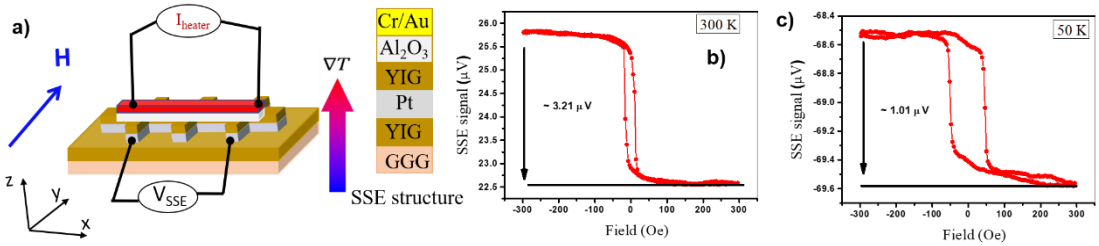

Figure 5- 7: Longitudinal spin Seebeck effect (LSSE) in spin valve structure with Pt as a 5 nm spacer. a) The conventional LSSE geometry for spin valve with additional Al_2O_3 as insulating layer and Cr/Au as heater on the top. b) SSE voltage as a function of magnetic field at room temperature. c) SSE voltage as a function of magnetic field at 50K.

5.3 Spin Valve Structure in thin films of YIG/Au/ YIG

5.3.1 Growth and Magnetization of YIG/Au/YIG

Growth of two YIG layers is similar as for YIG/Pt/YIG which is explained well in previous section. As was shown in previous section, Pt is not a good candidate to realize GMR since its spin diffusion length is smaller than the minimum Pt thickness required to decouple the YIG layers, so we chose next to use gold (Au) as its spin diffusion length is ~ 30 nm which is more than enough to decouple the two YIG layers. After growth of the bottom YIG layer, we use e-beam evaporation to grow Au with thicknesses between 6 and 10 nm at a rate of 1 Å/s to achieve uniform and flat surface. We need to keep in mind that dealing with Au is different from Pt, which is explained in chapter three. For our growth of YIG on top of Au, we must tune the annealing conditions for the top YIG layer to find the optimized parameters for annealing temperature and duration. After testing

many recipes, we found the optimized annealing temperature to be between 700 to 800 ˚C for a duration of time between 100 and 150 s.

The most important point is to achieve single crystal YIG layers and make them magnetized, otherwise, the growth and annealing conditions need to be reexamined. Right after the growth of the bottom YIG layer, we characterize its own magnetic properties by VSM measurement which shows a typical magnetic hysteresis loop with easy axis in the film plane as shown in figure 5-8, (a) and a coercive field H_c of ~ 4 Oe. At the same time, we need to test the growth of YIG on Au to make sure it is magnetic as well. It turns out the YIG is magnetic with the same behavior as YIG on Pt where H_c is larger with value of ~ 35 Oe as shown in figure 5-8, (b). For the whole spin valve structure with thicknesses YIG(20nm)/Au (10 nm)/YIG (20 nm), both YIG layers show magnetic properties with a clear anti-parallel magnetization state observed via VSM measurements as seen in figure 5-8, (c) which is again a first step towards GMR realization. In figure 5-8, (d), I plot all the different cases together to distinguish the magnetic hysteresis loop for individual layer and for spin valve structure.

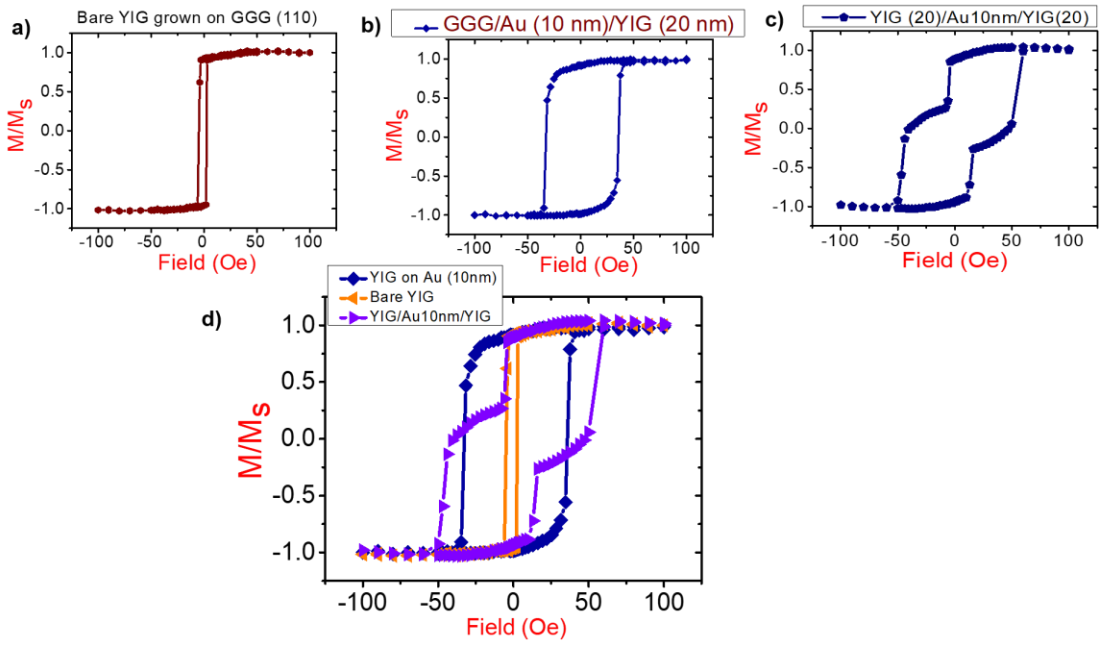

Figure 5- 8: Room Temperature magnetic characterization measured by VSM for bare YIG, YIG grown on Au (10 nm) and multilayers of YIG with Au in between as spacer. a) Magnetic hysteresis loop of bare YIG grown on GGG (110) showing in-plane magnetic anisotropy with $H_c \sim 4$ Oe. b) Magnetic hysteresis loop for YIG grown on Au(10 nm) with $H_c \sim 35$ Oe. c) Magnetic hysteresis loop of YIG/Au/YIG spin valve with 10 nm Au spacer layer showing anti-parallel magnetization state. d) plot for all previous case together to match H_c of two YIG layers in spin valve by bare YIG and YIG grown on Au.

5.3.2 Observation of GMR Effect

We then etch the top layer of YIG and Au into a Hall-bar geometry by ICP to define the width and length during electrical measurements while leaving the bottom YIG unetched as seen in figure 5-5. We perform the same set of room temperature measurements as was done for YIG/Pt/YIG in which we expect the resistance(R) to be higher during the anti-parallel state and decrease to its minimum value at the saturation point. Our first configuration for CIP measurement is to apply current in the x-direction while sweeping the magnetic field in the y-direction and monitoring the response in the

resistance. The resistance increases at the anti-parallel state matching exactly the same position observed from the magnetic hysteresis loops obtained via VSM as seen in figure 5-8, (a and b) and reaches its minimum value when each of the parallel states are reached. We then need to confirm this result by changing the measurement geometry such that the applied current and magnetic field are aligned along the x-direction. The result shows higher resistance during anti-parallel state as seen in figure 5-9, (c) which becomes minimum at magnetic saturation consistent with current perpendicular to field case. This result confirms the realization of GMR since it indicates that the mechanism responsible for this behavior is spin-dependent scattering of the conduction electrons during the anti-parallel state of magnetization.

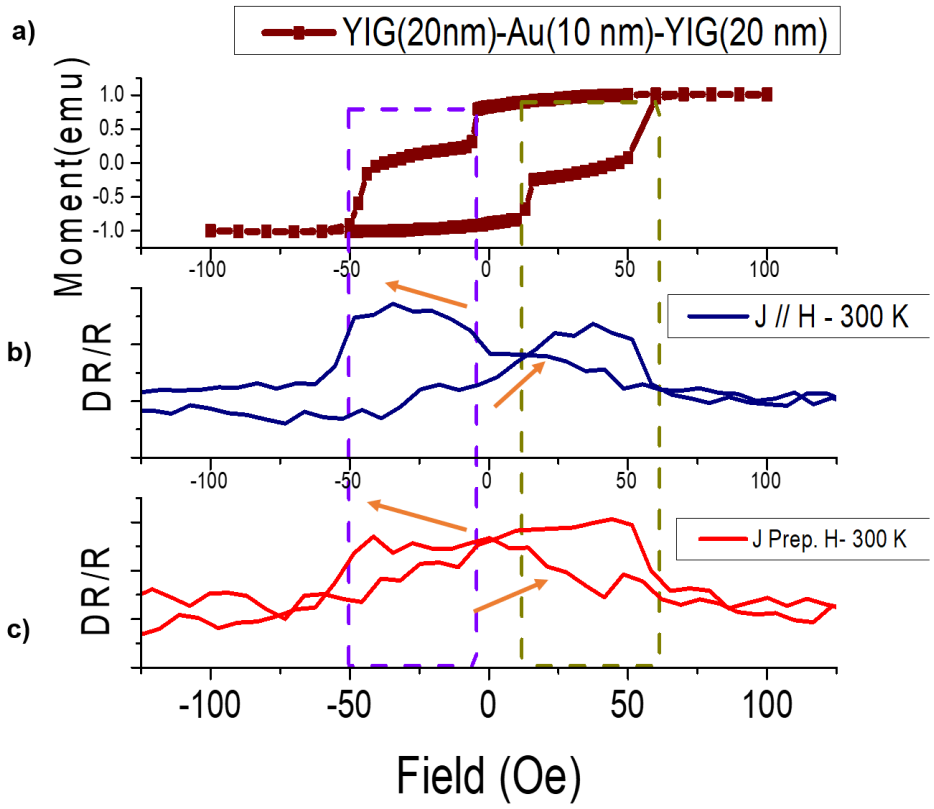

Figure 5- 9: Longitudinal magnetoresistance (MR) measurements for both measurement geometries: current is either perpendicular or parallel to the applied magnetic field. a) The magnetic hysteresis loop in spin valve structure showing anti-parallel state of magnetization. b) The MR ratio (*ΔR/R*) measurement as a function of magnetic field for current is perpendicular to magnet field geometry. c) The MR ratio (*ΔR/R*) measurement as a function of magnetic field for current is parallel to magnet field geometry.

Another test we can perform to confirm that the signal we obtained is truly GMR is to perform a temperature dependence where we would expect the MR signal to increase with decreasing temperature if it is truly GMR. The MR ratio $\frac{\Delta R}{R}$ (%) is defined as $(\frac{R-R_{||}}{R_{||}} \times 100)$ where R is the resistance and $R_{||}$ is the resistance when the magnetization is parallel to magnetic field. For the geometry with current perpendicular to applied magnetic field (I ⊥ H), the result of the MR ratio *ΔR/R (%)* we obtain is plotted

for different temperatures (300, 200, 100, 3) K as a function of magnetic field in figure 5-10, (a). As a result, the signal increases by one order of magnitude as the temperature decreases from 300K to 3K. The result we obtain for our other geometry where the magnetic field is swept parallel to the current direction (I //H) is similar to the (I ⊥ H) results where the MR ratio increases by one order of magnitude as the temperature is decreased from 300 K to 3K. This result shows that the signal we measure is GMR in this spin valve structure which proves that its mechanism is related to spin-dependent scattering at the interface during the anti-parallel state of magnetization.

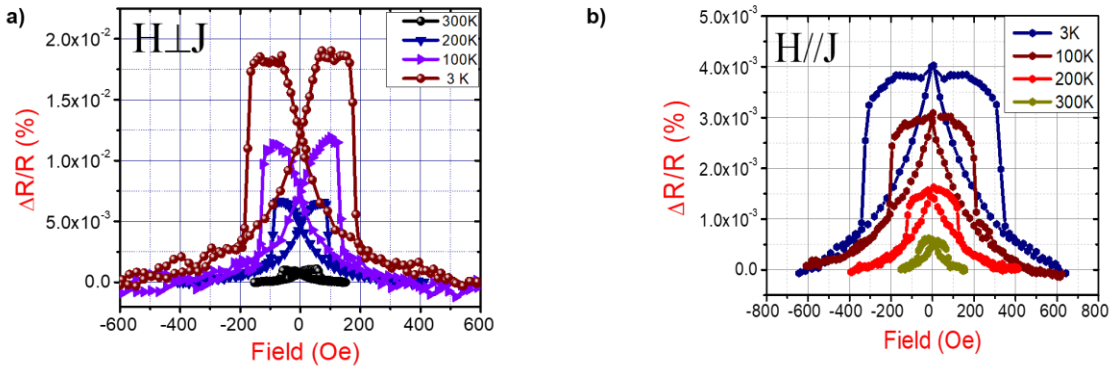

Figure 5- 10: Longitudinal MR ratio results for the two configurations with current either perpendicular or parallel to the applied magnetic field for different temperatures. a) *ΔR/R (%)* as function of magnet field for different temperatures in (I ⊥ H) geometry. b) *ΔR/R (%)* as function of magnet field for different temperatures in (I // H) geometry.

5.3.3 Longitudinal Spin Seebeck Effect

We perform LSSE measurements in our YIG (20 nm)/Au(10 nm)/YIG (20 nm) spin valve to support our GMR results. That means we expect to see a clear trend in the V_{SSE} signal which shows each contribution from the individual YIG layers. The LSSE structure and mechanism is already discussed throughout this thesis, so I will focus on the result. In figure 5-11, (a) SSE voltage is plotted as function of magnetic field at room temperature showing the typical SSE behavior we see in YIG alone. It is not very clear to see the individual contribution from each YIG layer as they emerged together, and we believe this is related to the sample temperature being higher than room temperature due to the temperature increase the sample gets from the heater that is necessary for SSE measurement. Comparing the LSSE result to our VSM data in which the anti-parallel state is very obvious, strongly indicates that the sample temperature is higher than room temperature. This claim is bolstered when we cool our cryostat down to 3K where both the anti-parallel state and spin voltage obtained from each YIG layer are distinguished. Figure 5-11, (b) shows that when the magnetizations of both YIG layers are parallel to the magnetic field, the thermal spin current generated by each layer is additive whereas in the anti-parallel state, spin current from each layer diffuse opposite sides in the y-direction and cancel each other out. Thus, the SSE voltage is zero in this case. Finally, with cooling the sample to lower temperature, we conclude that the anti-parallel state persists to higher fields which corresponds to H_c for each layer alone which also shows increasing behavior with decreasing temperature. Also, the magnitude of the SSE voltage increases as seen in figure 5-11, (c).

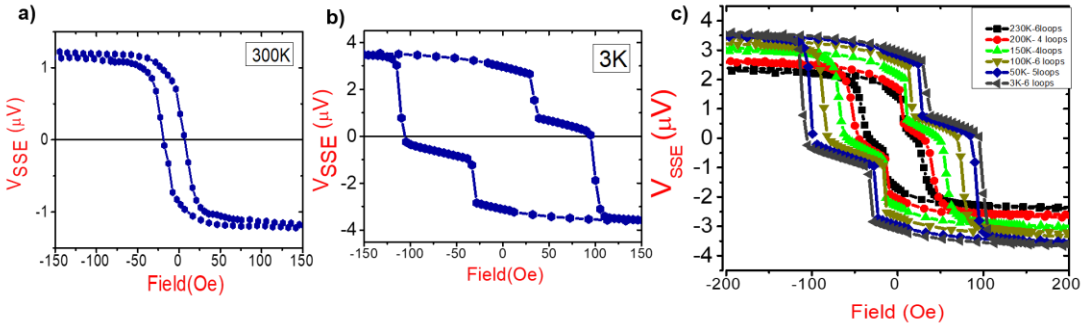

Figure 5- 11: Longitudinal spin Seebeck effect (LSSE) experiment in spin valve structure with Au as spacer with thickness of 10 nm. a) SSE voltage as a function of magnetic field at room temperature with anti-parallel state being not resolved. b) c) SSE voltage as a function of magnetic field at 3K with anti-parallel state is very clear. c) SSE voltage for different temperatures.

In summary, we have grown spin valve structures of both YIG/Pt/YIG and YIG/Au/YIG and measured their magnetic properties in order to confirm the decoupling of the YIG layers through the existence of an anti-parallel magnetization state between the bottom and top YIG layers. Pt and Au thickness are critical to make sure that it is enough to decouple the two layers of YIG. Realization of GMR using Pt as spacer is difficult due to is short spin diffusion length. However, in the case of Au, all prerequisites of achieving GMR are fulfilled and therefore, it is observed and confirmed by LSSE.

References:

1. Tsymbal, E.Y. & Pettifor, D.G. in Solid State Physics (eds. Ehrenreich, H. & Spaepen, F.) 113-237 (Academic Press, 2001).

2. Baibich, M.N. et al. Giant Magnetoresistance of (001)Fe/(001)Cr Magnetic Superlattices. *Physical Review Letters* **61**, 2472-2475 (1988).

3. Binasch, G., Grünberg, P., Saurenbach, F. & Zinn, W. Enhanced magnetoresistance in layered magnetic structures with antiferromagnetic interlayer exchange. *Physical Review B* **39**, 4828-4830 (1989).

4. Chappert, C., Fert, A. & Van Dau, F.N. The emergence of spin electronics in data storage. *Nature Materials* **6**, 813 (2007).

5. Roland, W., Roland, M. & Günter, R. Advanced giant magnetoresistance technology for measurement applications. *Measurement Science and Technology* **24**, 082001 (2013).

6. Barthélémy, A., Fert, A. & Petroff, F. in Handbook of Magnetic Materials 1-96 (Elsevier, 1999).

7. Rizal, C., Moa, B. & Niraula, B. Ferromagnetic Multilayers: Magnetoresistance, Magnetic Anisotropy, and Beyond. *Magnetochemistry* **2**, 22 (2016).

8. Parkin, S.S.P. Giant Magnetoresistance in Magnetic Nanostructures. *Annual Review of Materials Science* **25**, 357-388 (1995).

9. Parkin, S.S.P., More, N. & Roche, K.P. Oscillations in exchange coupling and magnetoresistance in metallic superlattice structures: Co/Ru, Co/Cr, and Fe/Cr. *Physical Review Letters* **64**, 2304-2307 (1990).

10. Dieny, B. Giant magnetoresistance in spin-valve multilayers. *Journal of Magnetism and Magnetic Materials* **136**, 335-359 (1994).

11. Tang, C. et al. Exquisite growth control and magnetic properties of yttrium iron garnet thin films. *Applied Physics Letters* **108**, 102403 (2016).

12. Aldosary, M. et al. Platinum/yttrium iron garnet inverted structures for spin current transport. *Applied Physics Letters* **108**, 242401 (2016).

13. Li, J. et al. Observation of magnon-mediated current drag in Pt/yttrium iron garnet/Pt(Ta) trilayers. *Nature Communications* **7**, 10858 (2016).

Chapter 6

Interface Modulated Spin Dynamics via Pt Resistivity Engineering in YIG/Pt Bilayers

6.1 Introduction and Motivation

Recent research reports have shown experimentally an enhancement of Spin Hall angle (SHA) θ_{SH} via increasing the electrical resistivity (ρ) of the materials. This increase can be engineered through element doping, introducing defects (disorder) and dilute alloys over a wide range of composition. Let's define here the spin Hall angle θ_{SH} as the efficiency of the spin-charge conversion $\theta_{SH} = (\frac{2e}{\hbar}) \times \frac{J_s}{J_e}$ Where J_s and J_e are spin and charge densities respectively.[1] Also, θ_{SH} can be defined as the ratio of the spin Hall (σ^{SH}) and charge (σ) conductivities, i.e. $\theta_{SH} = \frac{\sigma^{SH}}{\sigma}$ where σ is the charge conductivity of the material.[2]

First -principles calculations for Py/Pt claim that there is a monotonical increase in SHA with temperature and proportional to the resistivity of bulk Pt and spin-flip diffusion length (λ_{sf}) of Pt is proportional to the conductivity (σ).[3] Beside this correlation between highly resistive Pt and θ_{SH}, this paper suggests the charge current density may be more concentrated at the interface leading to larger interfacial SHA.[3] Based on Elliott-Yafet spin relaxation (EY) mechanism[4,5], higher conductivity (σ) would

lead to a higher (λ_{sf}) concomitantly, i.e., $(\lambda_{sf})\ \alpha\ (\sigma)$ which means λ_{sf} should scale linearly with $1/\rho_{Pt}$.

Experimental work carried out by Zhang, C *et al*. to study magnetization switching via spin-orbit torque in nanoscale structure of (MgO/CoFeB/W) based on critical role of W deposition conditions found out with high resistive β-phase of W from 110 to 202 μΩ.cm, the threshold switching current is decreased as SHA increased by a factor of 2-3 from (0.14-10.17 to 0.34-0.49). [6] Furthermore, another work of spin pumping done by Obstbaum, M. *et al*. shows substantial increase of the spin Hall angle (SHA) in alloy system of Py/Au_xPt_{1-x} bilayers determined for a wide range of composition. They found the pronounced maximum value of SHA is when $x \approx 0.5$ where the resistivity is the maximum at 150 μΩ.cm.[7] Also, another work in lateral spin valve devices is able to derive both θ_{SH} and λ_{sf} of Pt in the same device where the θ_{SH} is increased from ~ 2% to 14% as the Pt resistivity increases from ~ 7 to 70 μΩ.cm.[8]

For the spin Hall effect (SHE), it has two contributions, intrinsic regime where spin Hall conductivity is independent of charge conductivity while for extrinsic SHE, the spin Hall angle $(\theta_{SH}\ (t_{NM}) = \frac{2e}{\hbar}\ \sigma_{SH}\rho_{NM}\ (t_{NM})\ )$.[9] As we seen that theoretically and experimentally the spin Hall angle can be increased as resistivity of heavy metals increase, then in FM/HM bilayers, the spin current becomes larger and enters the FM layer with larger effect of the spin-orbit torque. Therefore, spin dynamics, on the other hand, can be affected and modulated across the interface. This change can be detected

through magnetization dissipation term of LLG equation which is parametrized by the Gilbert damping constant.

So, in this chapter, we investigate the room temperature spin dynamics of yttrium iron garnet (YIG) in heterostructures with different Pt resistivity in the range of 25 to 205 μΩ.cm. First, under different sputtering condition, we can engineer and control different resistivities in 5 nm thick Pt layer. Then, we study the structure and morphology of each condition and compare that to the normal condition. To extract the Gilbert damping coefficient, both FMR cavity and broadband waveguide are used to obtain resonance linewidth ΔH of the FMR spectrum as a function of FMR frequency. Based on this measurement, the quality of the of YIG/Pt interface can be quantified through the effective spin mixing conductance ($g_{eff}^{\uparrow\downarrow}$) which defines as the efficiency of spin currents across the interface are generated.

6.2 Engineering High Resistive Pt

We examined two different growth approaches trying to increase the resistance of Pt thin layer. DC magnetron sputtering is used to grow Pt for all samples mentioned here where the sputtering power (*P*) and Ar gas pressure are systematically varied. To start with, Hall bar channel is made on Si/SiO_2 as seen in figure 6-1, (a) to identify the thickness rate for Pt each time the conditions are changed and later to measure the resistance through I-V curve measurements. The first method used here is trying to increase sputtering power for the growth from 10 to 100 W as plotted in figure 6-1, (b).

the resistivity does not increase and is fluctuated around 30 μΩ.cm. Then, we try the second method of varying the growth pressure of Ar from 20 to 30 mTorr and the measured resistivity of 5 nm thick Pt increased exponentially up to 6000 30 μΩ.cm as shown in figure 6-1, (c). However, when we deposit Pt using the same conditions on YIG, the resistance is dropped a lot to ~ 40 μΩ.cm. After that, we use single crystal GGG substrate which is ultra-smooth and flat similar as YIG surface. Ar pressure is varied from 1.5 mTorr which is the minimum to strike the plasma plume to100 mTorr with keeping the growth power fixed to 60 W. The result as seen in figure 6-1, (d) is that the resistivity is increased from 25 to 205 μΩ.cm by a factor of eight. Based on this result, we achieve the high resistive recipe and need then to deposit different high resistive Pt directly on YIG to study the interfacial effect on spin dynamics.

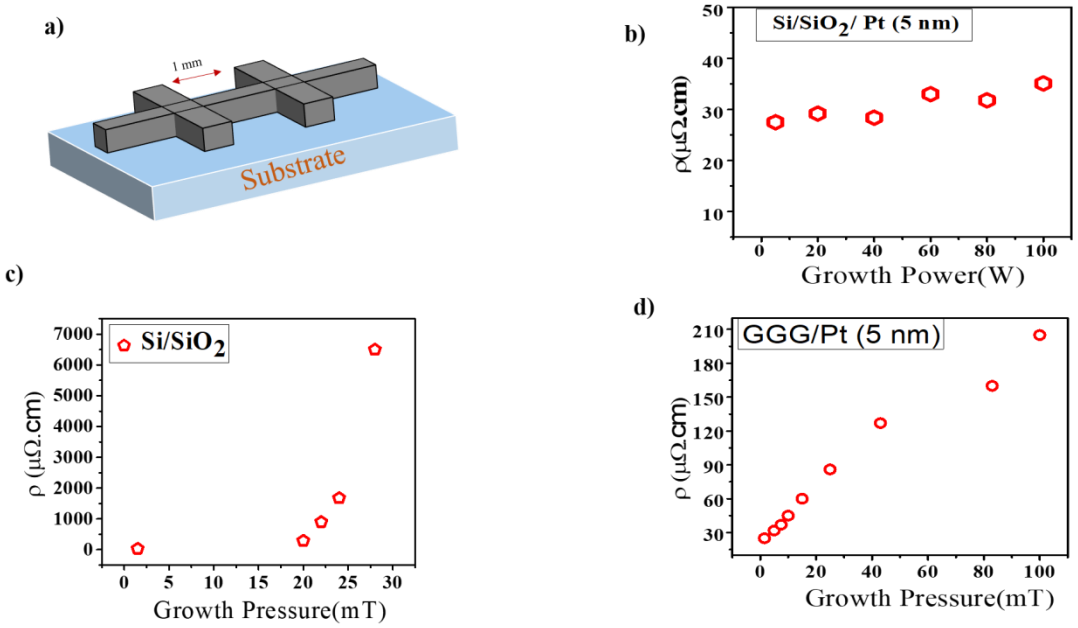

Figure 6- 1: Different growth result of engineering high resistive Pt layer. a) The Hall-bar geometry made using both photoresist and photolithography with dimensions of *W*= 100 µm, and the length (*L*) between tow leads is 1mm. b) Resistivity of Pt as a function of sputtering power as first attempt of increasing resistivity. c) Resistivity of Pt as a function of Ar sputtering pressure deposited on Si/SiO_2. d) Resistivity of Pt as a function of Ar sputtering pressure deposited on Single crystal GGG substrate.

After figuring out the high resistive recipe, we deposit 5 nm thick Pt everywhere with different Ar pressure on different YIG samples with thickness of 10 nm. Now, we need to know the morphology of each YIG film for different Pt condition and as seen in figure 6-2, the surface of each sample is different. So, AFM scan is used on an area of 2 µm× 2 µm on each sample and we start first with bare YIG as comparison to others and the roughness mean square (RMS) is 0.16 as seen in (a). For lower Ar pressure up to 5 mTorr, the surface is still flat and smooth with RMS up to 0.2 nm. As the pressure increase, the surface becomes rougher with RMS of 0.37 at 25 mTorr to 1.5 nm at 100 mTorr. Figure 6-2, (h) summarize all samples roughness as a function of Ar pressure.

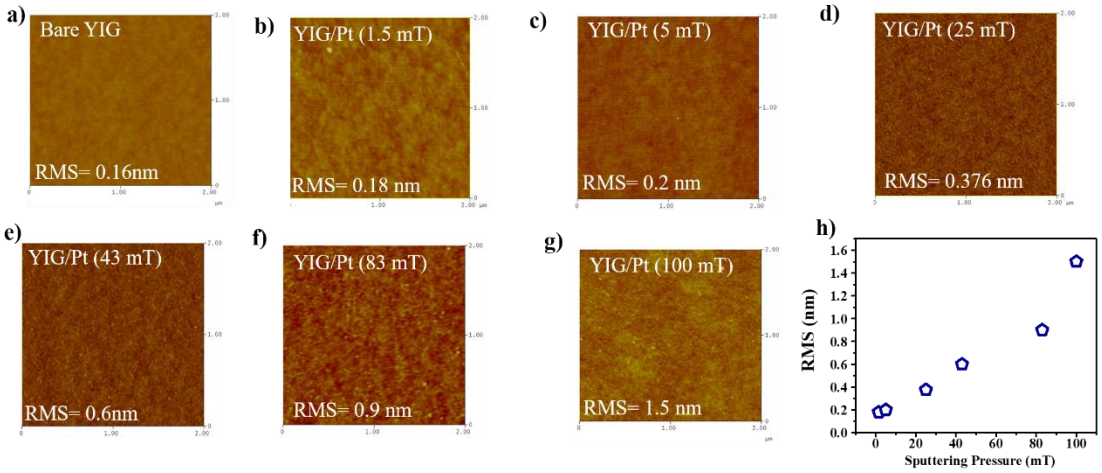

Figure 6- 2: AFM scans for each sputtering condition as the Ar pressure increased. AFM scan on an area of 2 µm× 2 µm for (a) Bare YIG, (b) Ar pressure of 1.5 mTorr. (c) Ar pressure of 5 mTorr. (d) Ar pressure of 25 mTorr. (e) Ar pressure of 43 mTorr. (f) Ar pressure of 83 mTorr. (g) Ar pressure of 100 mTorr. (h) Summary of the roughness (RMS) as a function of Ar pressure for Pt growth.

6.3 Interface Effect on Spin Dynamics Modulation

The goal of this work is to study the high resistive Pt layer with thickness of 5 nm on magnetization precession of bottom YIG layer with 10 nm thickness during resonance as spin current is pumping across the interface and how that affect the Gilbert damping coefficient (α). Many aspects need be investigated such as expecting higher damping based on higher spin Hall angle and quality of interfacial layer between Pt and YIG as to control the spin current flow from YIG into Pt. Therefore, to study the Gilbert damping tunability, Cavity FMR and broadband coplanar waveguide FMR are used the spin

dynamics for bare YIG and then 5 nm Pt on top deposited afterwards for each growth condition of Pt.

6.3.1 Cavity FMR Measurements

We measure all samples of bare YIG with thickness of 10 m first in the FMR cavity using a Bruker 9.6 GHz X-band EMX EPR spectrometer in which single peak of FMR derivative absorption spectrum for each angle from in-plane (θ_H=90˚) up to out-of-plane (θ_H=0˚) is captured. The angle is measured with respect to z direction. These single peak spectra can be fitted with a single Lorentzian derivative to obtain two important quantities from the fit, the peak to peak linewidth (ΔH_{pp}) and resonance field (H_{res}). The mean values for both ΔH_{pp} and H_{res} for all ten samples are ~ 10 Oe and ~2389 respectively. Furthermore, to study the in-plane anisotropy, we perform FMR as a function of polar angles (θ_H) and then fit that to some anisotropy equations to obtain the best-fit parameters, the effective saturation magnetization ($4\pi M_{eff}$) and the g-factor where their mean values are ~2200 Oe and 2.2. The data of all bare YIG samples are plotted below with YIG/Pt measurements.

All 10 samples of bare YIG have almost similar FMR results, so we need to focus now on Pt layer with different resistivity. Highly conductive and resistive samples are reported here. In details, both high conductive samples grown at lower Ar pressure show larger FMR response after Pt being deposited in terms of broadening of peak-to-peak linewidth (ΔH_{pp}) as increased by a factor of five as seen in figure 6-3 and 6-4. With respect to $4\pi M_{eff}$, it increased by 15% for the sample grown at lowest Ar pressure

whereas for other sample grown at 5 mTorr, there is no difference. At this point, these sample are very conductive, and we do not expect the line broadening is based on resistivity.

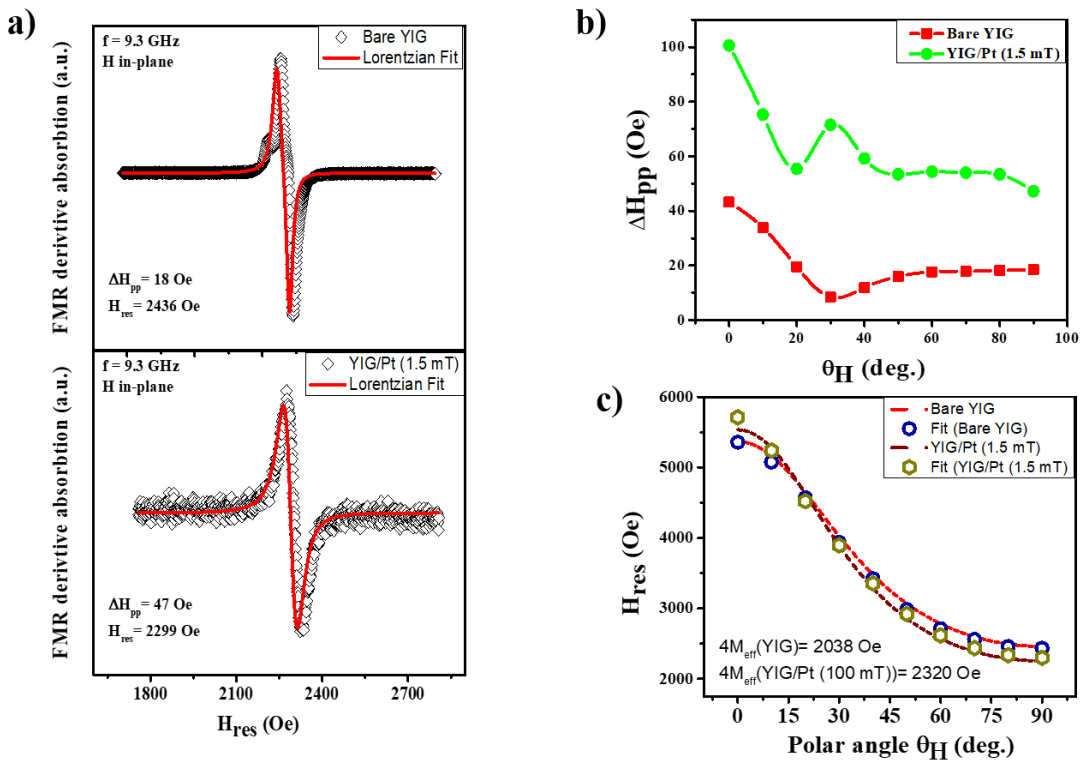

Figure 6- 3: Comparison of FMR cavity spectra measurements on bare YIG and YIG/Pt (5 nm) for high conductive Pt grown at Ar pressure 1.5 mTorr. a) FMR derivative absorption spectra for bare 10 nm thick YIG and YIG/Pt (5 nm) respectively measured with magnetic fields in-plane and cavity frequency of 9.3 GHz. Lorentzian derivative fit is shown by red lines. b) Linewidth broadening (ΔH_{pp}) dependence as a function of polar angle (θ_H) for bare YIG and YIG/Pt. c) Resonance field (H_{res}) dependence as a function of polar angle (θ_H) for both YIG and YIG/Pt (5 nm).

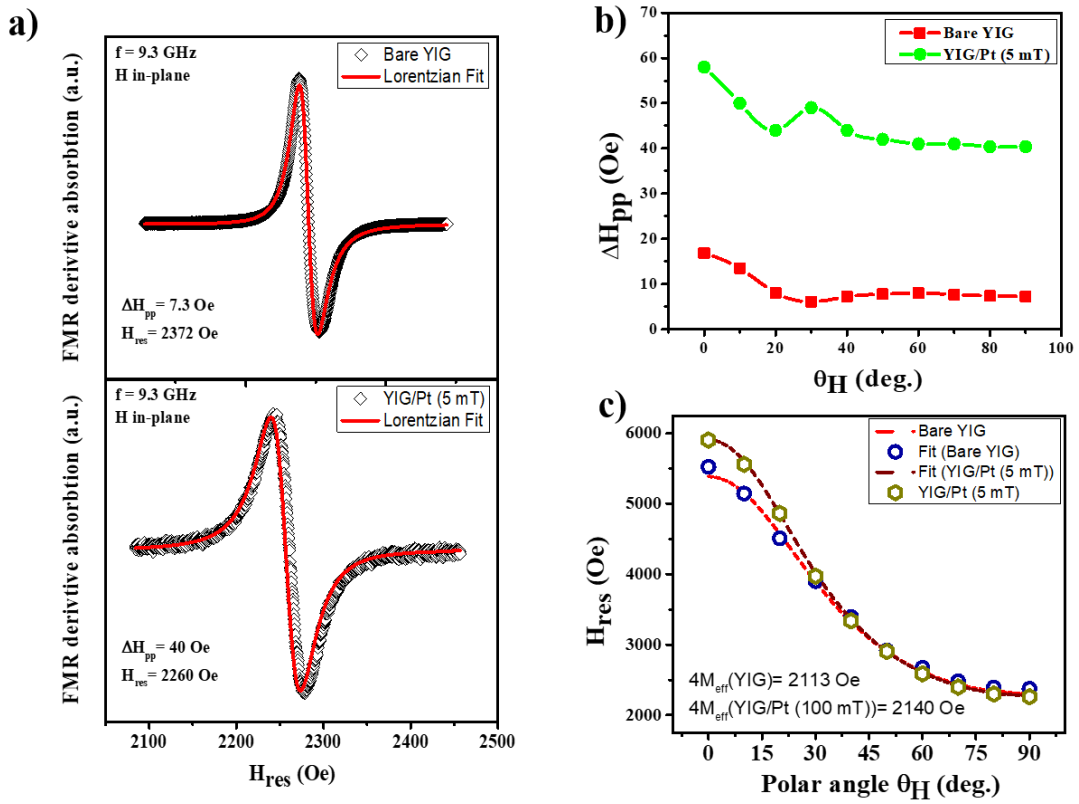

Figure 6- 4: Comparison of FMR cavity spectra measurements on bare YIG and YIG/Pt (5 nm) for high conductive Pt grown at Ar pressure 5 mTorr. a) FMR derivative absorption spectra for bare 10 nm thick YIG and YIG/Pt (5 nm) respectively measured with magnetic fields in-plane and cavity frequency of 9.3 GHz. Lorentzian derivative fit is shown by red lines. b) Linewidth broadening (ΔH_{pp}) dependence as a function of polar angle (θ_H) for bare YIG and YIG/Pt. c) Resonance field (H_{res}) dependence as a function of polar angle (θ_H) for both YIG and YIG/Pt (5 nm).

On the other hand, for high resistive Pt layer of 160 and 205 μΩ.cm cases, surprisingly as we believe the spin Hall angle is increased based on literature, there no effect for spin pumping where the result is the same for bare YIG and after 5 nm Pt being deposited. As shown in figure 6-5 and 6-6, the linewidth broadening (ΔH_0) is still the

same for bare YIG and YIG/Pt. One possibility of why there is change is that the first layer on Pt deposition is rough blocking most of spin current from being drawn by Pt acting as spin pumping. Interface quality will be discussed in spin mixing conductance section.

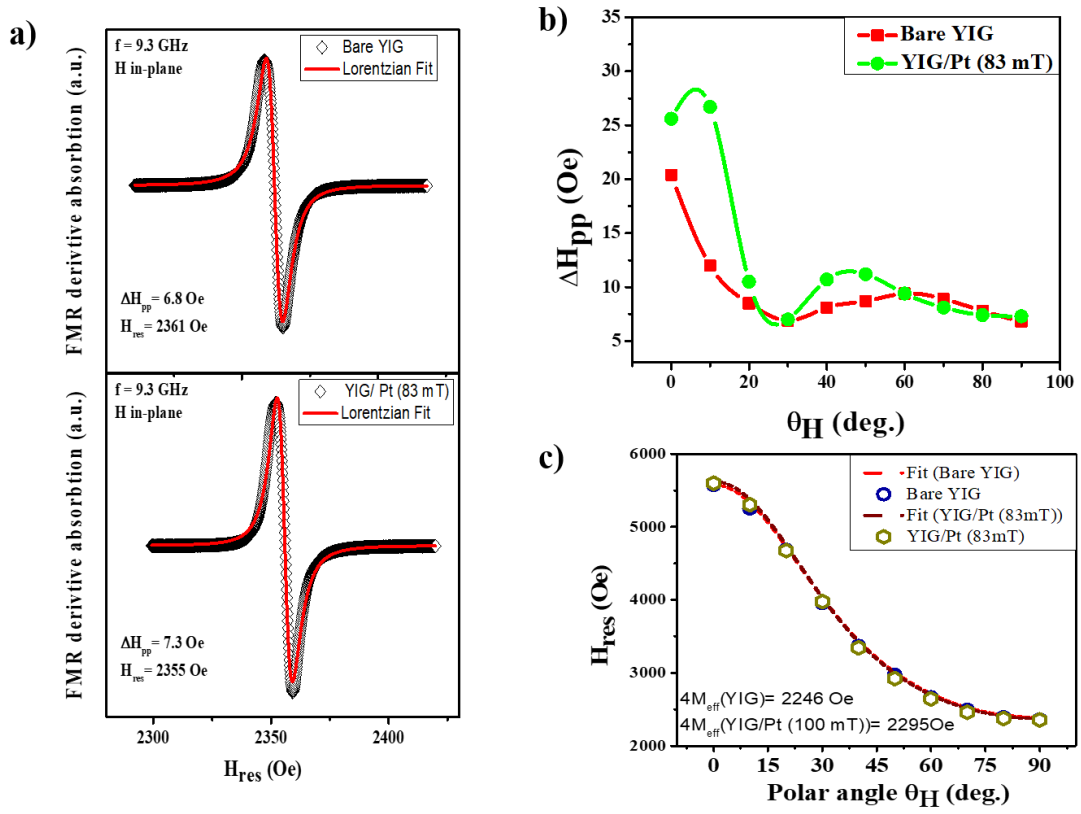

Figure 6- 5: Comparison of FMR cavity spectra measurements on bare YIG and YIG/Pt (5 nm) for high resistive Pt grown at Ar pressure 83 mTorr. a) FMR derivative absorption spectra for bare 10 nm thick YIG and YIG/Pt (5 nm) respectively measured with magnetic fields in-plane and cavity frequency of 9.3 GHz. Lorentzian derivative fit is shown by red lines. b) Linewidth broadening (ΔH_{pp}) dependence as a function of polar angle (θ_H) for bare YIG and YIG/Pt. c) Resonance field (H_{res}) dependence as a function of polar angle (θ_H) for both YIG and YIG/Pt (5 nm).

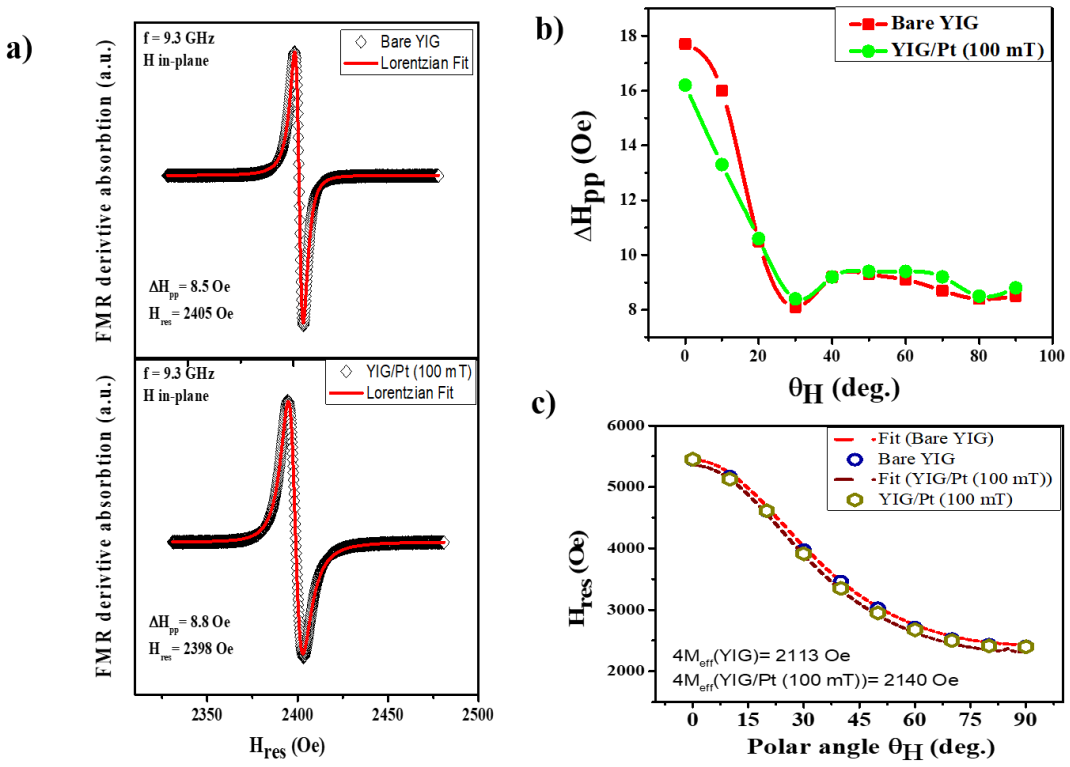

Figure 6- 6: Comparison of FMR cavity spectra measurements on bare YIG and YIG/Pt (5 nm) for high resistive Pt grown at Ar pressure 100 mTorr. a) FMR derivative absorption spectra for bare 10 nm thick YIG and YIG/Pt (5 nm) respectively measured with magnetic fields in-plane and cavity frequency of 9.3 GHz. Lorentzian derivative fit is shown by red lines. b) Linewidth broadening (ΔH_{pp}) dependence as a function of polar angle (θ_H) for bare YIG and YIG/Pt. c) Resonance field (H_{res}) dependence as a function of polar angle (θ_H) for both YIG and YIG/Pt (5 nm).

6.3.2 Coplanar Waveguide Measurements

As the FMR cavity shows the effect of high conductive Pt layer on YIG through broadening FMR linewidth whereas high resistive Pt layer does not have a response, broadband FMR measurements using a coplanar waveguide set-up operated with

frequency up to 14 GHz is used to confirm the FMR cavity data via extracting the Gilbert damping constant (α). Figure 6-7 shows the linear relation between linewidth broadening (ΔH) and FMR frequency for both high conductive and resistive samples and α can be calculated from $\Delta H = \frac{2\pi\alpha}{\gamma} f + \Delta H_0$ where γ and ΔH_0 are the gyromagnetic ratio and the inhomogeneity broadening respectively. it turns out that the α is increased in both high conductive samples by a factor of 5 and $\Delta\alpha \approx 7 \times 10^{-3}$ whereas α for the high resistive ones is almost the same as for bare YIG.

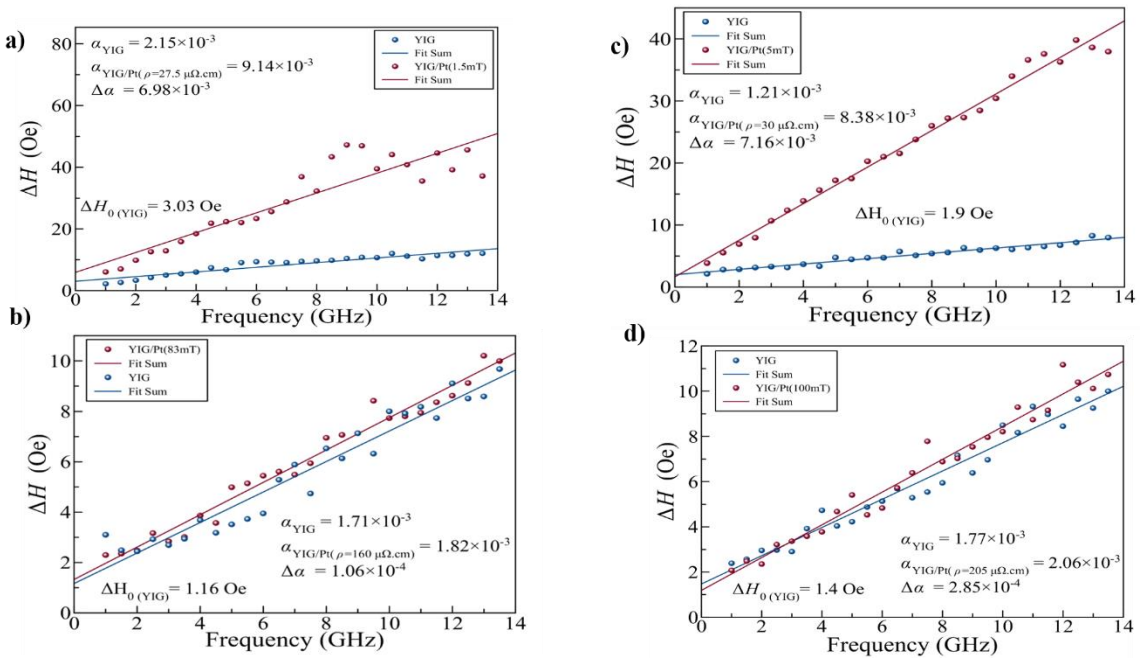

Figure 6- 7: Extracted Gilbert damping from linear fit between FMR linewidth (ΔH) and FMR frequency (f). Frequency dependence of FMR linewidth for four samples, first bare YIG and then 5 nm Pt deposited on the top. a) Both bare YIG and YIG/Pt (5 nm) grown at 1.5 mTorr. b) Both YIG and YIG/Pt (5 nm) grown at 5 mTorr. c) Both YIG and YIG/Pt (5 nm) grown at 83 mTorr. d) Both YIG and YIG/Pt (5 nm) grown at 100 mTorr.

Figure 6-8 summarizes all results of bare YIG and then the same sample used to sputter 5 nm of Pt on the top with different growth condition each time. Therefore, figure 6-8, (a) shows Δα as a function of Pt pressure for all 10 samples with very clear trend of high conductive samples have higher Gilbert damping constant α and then the trend decreases as resistivity becomes larger with the difference being almost zero starting at 15 up to 100 mTorr. The same trend is seen in figure 6-8, (b) in FMR cavity measurement of the difference between the linewidth broadening between YIG/Pt and bare YIG. There is extra point where we deposit 0.5 nm Pt with at 1.5 mTorr on YIG and then 4.5 nm at 43 mTorr to probe the interface quality where α is enhanced by 41% compared to high conductive samples grown at 1.5 and 5 mTorr.

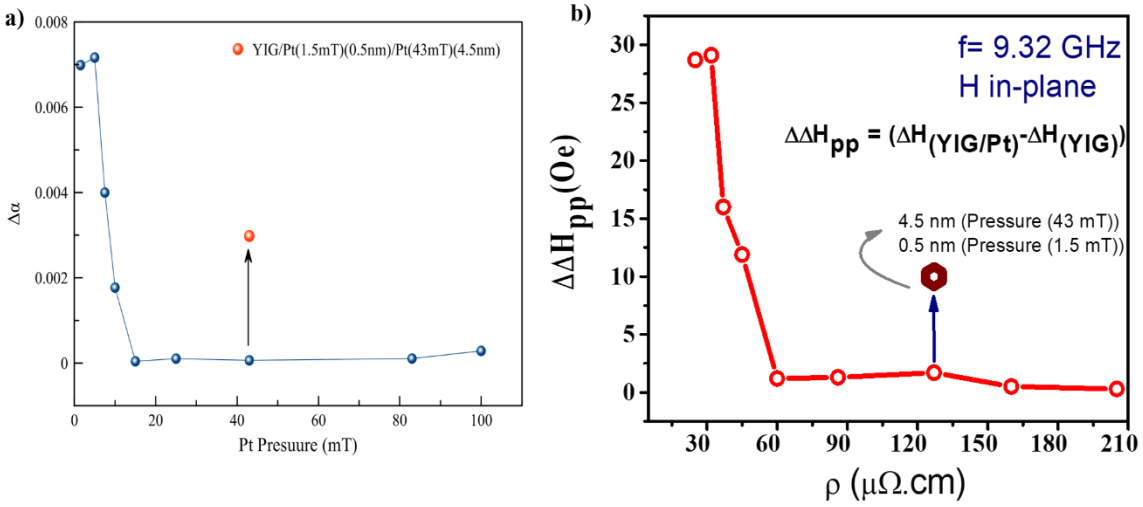

Figure 6- 8: Gilbert damping difference (Δα) and linewidth broadening difference ($\Delta\Delta H_{pp}$) between bare YIG and YIG/Pt for different sputtering growth conditions. a) Gilbert damping difference as a function of Ar pressure. b) linewidth broadening difference ($\Delta\Delta H_{pp}$) as a function of Pt resistivity.

6.4 Interface Analysis via Spin-Mixing Conductance

The effective spin mixing conductance ($g_{eff}^{\uparrow\downarrow}$) is the essential parameter to investigate the spin pumping experimentally reflecting the spin injection efficiency in spin pumping a cross the interface between YIG and Pt. $g_{eff}^{\uparrow\downarrow}$ is expressed by

$$g_{eff}^{\uparrow\downarrow} = \frac{4\pi M_s\, t_{YIG}}{g\mu_B}((\alpha_{\,Pt/YIG} - \alpha_{YIG}),$$

where $4\pi M_s$ is saturation magnetization, t_{YIG} is the thickness of YIG, g is the Lande-factor, μ_B is the Bohr magneton and $\Delta\alpha$ is the Gilbert damping difference between YIG and YIG/Pt. Figure 6-9 shows $g_{eff}^{\uparrow\downarrow}$ as a function of Pt resistivity with the same trend with higher conductivity has higher spin mixing conductance whereas the high resistive samples show negligible spin current injection through the interface. More importantly, we put 0.5 nm Pt of conductive Pt as a buffer layer and then 4.5 nm Pt of high resistive one grown at 43 mTorr and the result is indeed there is enhancement of 41% compared to the highest efficiency for those high conductive samples.

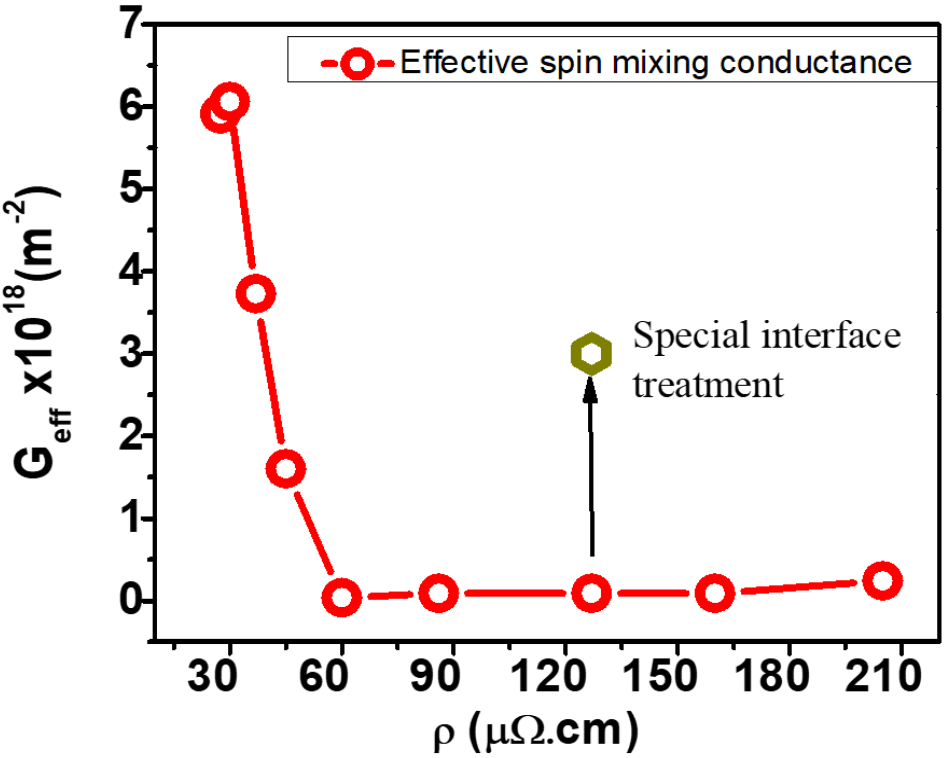

Figure 6- 8: Calculated Spin mixing conductance ($g_{eff}^{\uparrow\downarrow}$) as a function of Pt resistivity.

References:

1. Pai, C.-F., Ou, Y., Vilela-Leão, L.H., Ralph, D.C. & Buhrman, R.A. Dependence of the efficiency of spin Hall torque on the transparency of Pt/ferromagnetic layer interfaces. *Physical Review B* **92**, 064426 (2015).

2. Berger, A.J. et al. Determination of the spin Hall effect and the spin diffusion length of Pt from self-consistent fitting of damping enhancement and inverse spin-orbit torque measurements. *Physical Review B* **98**, 024402 (2018).

3. Wang, L. et al. Giant Room Temperature Interface Spin Hall and Inverse Spin Hall Effects. *Physical Review Letters* **116**, 196602 (2016).

4. Elliott, R.J. Theory of the Effect of Spin-Orbit Coupling on Magnetic Resonance in Some Semiconductors. *Physical Review* **96**, 266-279 (1954).

5. Yafet, Y. Conduction electron spin relaxation in the superconducting state. *Physics Letters A* **98**, 287-290 (1983).

6. Zhang, C. et al. Critical role of W deposition condition on spin-orbit torque induced magnetization switching in nanoscale W/CoFeB/MgO. *Applied Physics Letters* **109**, 192405 (2016).

7. Obstbaum, M. et al. Tuning Spin Hall Angles by Alloying. *Physical Review Letters* **117**, 167204 (2016).

8. Sagasta, E. et al. Tuning the spin Hall effect of Pt from the moderately dirty to the superclean regime. *Physical Review B* **94**, 060412 (2016).

9. Nguyen, M.-H., Ralph, D.C. & Buhrman, R.A. Spin Torque Study of the Spin Hall Conductivity and Spin Diffusion Length in Platinum Thin Films with Varying Resistivity. *Physical Review Letters* **116**, 126601 (2016).

Chapter 7

Systematic Control of Strain-induced Perpendicular Magnetic Anisotropy in Epitaxial Terbium Iron Garnet Thin Films

7.1 Introduction and Motivation

In the first chapter of this thesis, we gave a rich discussion about different kinds of anisotropy particularly their origin and their effect on magnetic properties. In this chapter, we focus on the interfacial strain anisotropy and its ability to tune magnetic properties by leveraging a lattice-mismatch and magnetostriction effect. One of the motivations for this work is that in rare-earth iron garnets (REIG) engineering and controlling perpendicular magnetic anisotropy (PMA) is still rudimentary, so our goal is to carry out a systematic study over a wide range of thin film thicknesses. Our second goal is to study the strain relaxation up to the maximum thickness our films can be grown before this effect dies off. It is well established that in ferromagnetic metal thin films, the relaxation is quick and this effect dies off at very small thickness such as a few monolayers.[1,2,3] However, REIGs are totally different from ferromagnetic metals in which they have a giant unit cell with 160 atoms with large lattice constant (~1.2 nm) and large Burger's vectors, $\boldsymbol{b}$ yielding a very large dislocation energy causing a slow relaxation decay. We pick $Tb_3Fe_5O_{12}$ (TbIG) as a candidate to study the full control of PMA because its magnetostriction constant is positive and large so that it allows us to modulate the strain over different thicknesses.

Therefore, in this chapter, we study and control strain-induced PMA in TbIG, epitaxially grown on GGG with (111) orientation, over a wide range of thicknesses from 5 to 100 nm. Because TbIG magnetization ($4\pi M_s$) is small, we use an innovative way to determine the PMA field through electrical measurements of the induced anomalous Hall effect in Pt deposited on the TbIG thin films. We characterize TbIG structure through RHEED pattern and monitor its relaxation evolution through XRD spectra. Another interesting feature of TbIG is that it has a compensation temperature (T_{comp}) ~ 240 K which led us to perform a comprehensive study into the behavior of the AHE both above and below T_{comp}. Surprisingly, just above and below T_{comp}, a huge perpendicular shift in AHE hysteresis loop is observed due mainly to some Tb spins being frozen and hard to switch. Overall, this complete study demonstrates a general approach of tailoring magnetic anisotropy in REIG materials by utilizing modulated strain via epitaxial growth.

7.2 Engineering PMA in $Tb_3Fe_5O_{12}$

Under strain-free conditions, the magnetization of a REIG thin film lies in the film plane because the magnetocrystalline anisotropy is generally smaller than the shape anisotropy which favors the in-plane orientation. However, due to relatively large magnetostriction constant λ, the strain-induced magnetic anisotropy energy can be even more important in thin films. This property gives epitaxial growth of REIG films a unique advantage in controlling magnetic anisotropy. Depending on the sign of λ, suitable substrates can be chosen to not only manipulate the magnitude, but also the sign of the total magnetic anisotropy energy, therefore the orientation of the magnetization

vector. For example, for positive (negative)λ, compressive (tensile) strain is required to drive the magnetization normal to the film plane, which can be accomplished by controlling lattice mismatch in the pseudomorphic growth regime.

In order to orient the magnetization normal to the film, the perpendicular magnetic anisotropy (PMA) field $H_\perp$ must be positive and larger than the demagnetizing field. For the case of strained films grown on (100) and (111)-oriented substrates, $H_\perp$ is given by the following equations

$$H_\perp = \frac{2K_1 - 3\lambda_{100}\sigma_\parallel}{M_s} \qquad \text{for (100)} \qquad (1)$$

$$H_\perp = \frac{-4K_1 - 9\lambda_{111}\sigma_\parallel}{3M_s} \qquad \text{for (111)} \qquad (2)$$

where K_1 is the first-order cubic anisotropy constant, $\sigma_{||}$ is the in-plane stress, M_s the saturation magnetization and λ_{lmn} is the magnetostriction constant for the film grown in the [*lmn*] direction. From these equations, it follows that $H_\perp$ can be controlled by tuning the in-plane stress of the film, which can be achieved by controlling growth.

From the above equations, magnetostriction constant (λ_{lmn}) and in-plane stress ($\sigma_{||}$) are important quantities to tune the PMA. In the case of TbIG, the λ_{lmn} is $\lambda_{100} = -3.3\times10^{-6}$, $\lambda_{111} = 12\times10^{-6}$ at room temperature.[4] To achieve PMA, a compressive strain is required for positive λ_{lmn} which has to be λ_{111} and a tensile strain for negative λ_{lmn} which in this case λ_{100}. To specify the substrate, we choose GGG where the strain is less than 1% which can be accommodated for pseudomorphic growth of TbIG. That means we

need to use (111) orientation. In the table below, the PMA field for GGG (111) is positive and 2.2 T yielding robust PMA. However, in the case of (100), the PMA is negative with value of -0.6 T indicating more in-plane anisotropy.

Orientation	λ_{111} (10^{-6})	K_1 (10^{-3} erg·cm^{-3})	GGG lattice constant (Å)	TbIG lattice constant (Å)	$4\pi M_s$ (G)	In-plane strain $\varepsilon_{\parallel}$	$H_{\perp}$ (T)
(111)	12	-6	12.383	12.435	225	0.418%	2.2
(100)	-3.3	-6	12.383	12.435	225	0.418%	-0.6

Table 7- 1: Estimation of the perpendicular magnetic anisotropy field PMA ($H_{\perp}$) as a function of GGG substrate with orientation of (111) and (100) at room temperature.

7.3 Epitaxial Growth of Strained TbIG on GGG (111)

After the standard cleaning process of GGG (111) substrate as discussed in chapter two, the TbIG thin films were grown using PLD technique in which the substrates were baked inside the chamber at ~ 220°C for five hours with a base pressure < 10^{-6} Torr before deposition. After this annealing process, the substrates were then annealed at ~ 600°C under a 1.5 mTorr oxygen pressure with 12% (wt. %) ozone for 30 minutes; then under these oxygen and temperature conditions, a 248 nm KrF excimer laser pulse was set to strike the target with a power of 156 mJ and at a repetition rate of 1 Hz. After deposition, the films were annealed *ex situ* at 800°C for 200 seconds under a steady flow of oxygen using rapid thermal annealing (RTA).

7.3.1 Structure and Morphology Properties

To characterize the structural properties of the deposited TbIG, reflection high energy electron diffraction (RHEED) was used to track the evolution of the film growth. Right after deposition, RHEED shows the absence of any crystalline order. After the *ex situ* RTA process, RHEED patterns appear revealing a single crystal structure for all the samples. Figure 7-1, (a and b) show typical RHEED patterns for both directions of $[1\bar{1}0]$ and $[11\bar{2}]$ for TbIG with the thickness of 30 nm. Atomic force microscopy (AFM) was performed on all grown samples, indicating uniform and atomically flat films with low root-mean-square (RMS) roughness of 1.34 Å and with no pinholes observed as seen in 3-D scan (figure 7-1, (c)). The absence of three-dimensional islands on the surface from AFM measurements confirms the uniformity of the thin films.

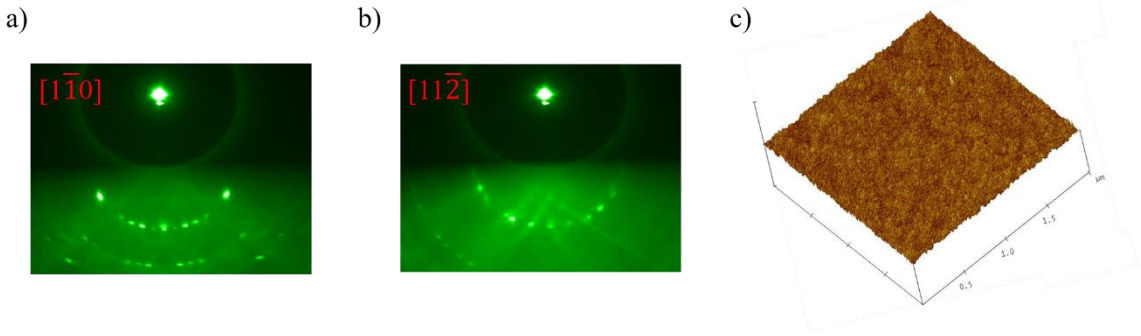

Figure 7- 1: RHEED and surface characterization of GGG (111)/TbIG(30 nm) thin films. (a)&(b) RHEED patterns of (a) E-beam along $[1\bar{1}0]$ direction and (b) E-beam along $[11\bar{2}]$ direction. Both show single crystal structure after annealing. (c) $2\mu m \times 2\mu m$ of 3D AFM surface morphology scan of TbIG (30 nm) thin film with RMS roughness of 1.34 Å.

7.3.2 Strain Characterization by XRD

X-ray diffraction (XRD) was performed on all the samples to further confirm their crystalline structure, using a PANalytical Empyrean diffractometer with Cu K_α radiation and a Ni filter, at room temperature in 0.002° steps in the 2θ range of 10°-90°. for the TbIG samples one main peak for TbIG and GGG is observed, corresponding to the (444) Bragg peak, thus confirming epitaxy and the single crystal structure for both samples. No secondary phase was observed, corroborating the high quality of the obtained films.

For films with $t > 10$ nm, the XRD data shows that the Bragg peak corresponding to both REIGs is shifted to the left from the expected peak positions for the respective bulk crystals (figure 7-2, (a)), thus indicating an elongation on the lattice parameter perpendicular to the surface, leading to a compressive in-plane strain in the lattice. Moreover, a systematic shift to higher 2θ values of the diffraction peaks as the thickness of the thin film increases is a direct measurement of the relaxation of the lattice parameters towards the bulk values (figure 7-2, (b)). The surprisingly slow relaxation behavior in REIG thin films contrasts sharply with ferromagnetic metal films, demonstrating a unique magnetic anisotropy control possibility by film thickness.

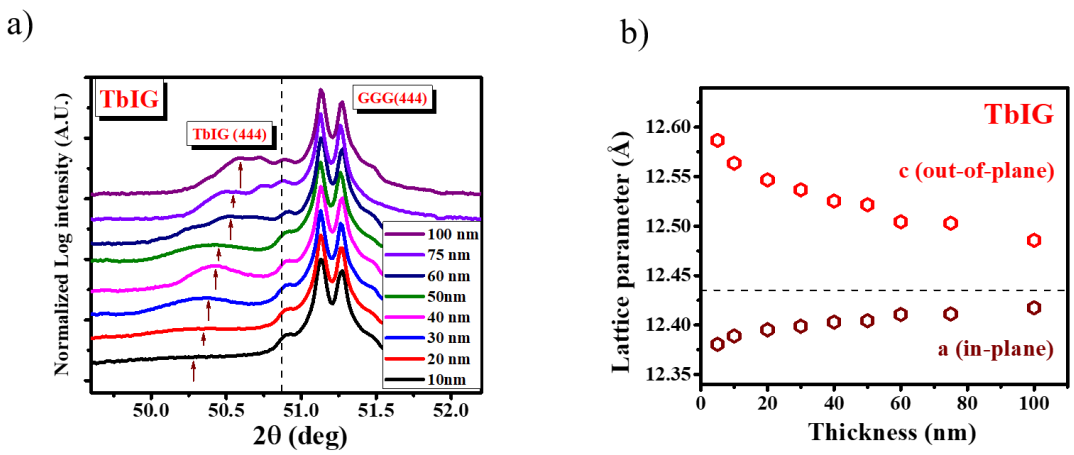

Figure 7- 2: Structure analysis of GGG (111)/TbIG thin films for different thickness. (a) Normalized semi-log plot of θ -2θ XRD scans of TbIG of thickness t= 10, 20, 30, 40, 50, 60, 75 and 100 nm grown on GGG (111) substrate. The dashed line shows the 2θ positions of the bulk material. The arrows indicate the position evolution of (444) peak for TbIG as strain relaxes. (b) Thickness dependence of the out-of-plane lattice constant *c* and in-plane lattice constant *a* for TbIG on GGG (111). The dashed line represents the bulk lattice constant (a= 12.435 Å) for TbIG.

In order to determine the in-plane stress $\sigma_{\parallel}$ in the garnet films, it is necessary to consider the elastic deformation tensor of the material. When a film with cubic crystalline structure is grown on a single crystal substrate, and assuming the material originally is isotropic, then two strain components can be considered: an in-plane biaxial strain $\varepsilon_{\parallel}$ and an out-plane uniaxial strain $\varepsilon_{\perp}$. These parameters are related through the elastic stiffness constants by[5,6]

$$\epsilon_{\parallel} = -\frac{c_{11}+2\,c_{12}+4\,c_{44}}{2c_{11}+4\,c_{12}-4\,c_{44}}\,\epsilon_{\perp} \quad \text{for film grown on (111) substrate,} \qquad (3)$$

And $$\epsilon_{\perp} = \frac{c-a_0}{a_0}, \qquad (4)$$

c being the out-of-plane lattice parameter for the strained film, and a_0 the lattice parameter for the relaxed (bulk) material; c can be obtained from the XRD data according to the equation $c = d_{hkl}\sqrt{h^2 + k^2 + l^2}$. For the case t < 10 nm, $\varepsilon_\parallel$ can be obtained directly from the RHEED pattern. $\sigma_\parallel$ can be calculated then by

$$\sigma_\parallel = -6c_{44}\frac{c_{11}+2c_{12}}{2c_{11}+4\,c_{12}-4\,c_{44}}\epsilon_\perp \qquad \text{for the (111) case,} \qquad (5)$$

where c_{ii} corresponds to the elastic stiffness constants. For TbIG (c_{11} = 26.53×10^{11} dyne/cm^2, c_{12} = 11.07×10^{11} dyne/cm^2, c_{44} = 7.15×10^{11} dyne/cm^2), [7] the values for $\sigma_\parallel$ can be calculated then from equation (5), which are listed in Table 7-2.

7.3.3 Magnetic Measurements

Magnetization hysteresis curves (M vs. H) were obtained on the grown films using a vibrating sample magnetometer (VSM) at room temperature with the applied magnetic fields normal and parallel to the plane. From the raw data, the linear paramagnetic background from the GGG substrate was subtracted. All TbIG thicknesses show an easy-axis hysteresis loop up to 100 nm for magnetic fields perpendicular to the plane, and a hard-axis loop for in-plane magnetic fields. TbIG thin films preserve the strong PMA over the entire thickness range (up to 100 nm). The saturation magnetization for all films is summarized in Table 7-2. The average saturation magnetization is $4\pi M_s$ =

(234 ± 5) G, which is only 3.4% below the reported value for bulk TbIG ($4\pi M_s$ = 242.21 G).[8]

7.4 Anomalous Hall Hysteresis in TbIG/Pt

Since the TbIG films are magnetic insulators, the Hall response of Pt imprints the magnetic anisotropy in different thicknesses of TbIG via the magnetic proximity effect and/or the spin current effect.[9] Therefore, a 5 nm thick Pt layer was sputtered into the Hall bar geometry with a length of l = 600 µm and a width of w = 100 µm using standard photolithography as seen in figure 7-2, (a). Also, in the same figure, we define the current direction and Hall voltage (V_{yx}) measurement set-up. Our measured Hall response contains two parts: the ordinary Hall effect (OHE) which is linear in field, and the anomalous Hall effect (AHE) which is proportional to the out-of-plane component of magnetization. Figure 7-2, (b) shows sharp squared out-of-plane AHE hysteresis loops after subtraction of linear background from OHE. All TbIG thicknesses from 2 unit cells up to 75 nm show very sharp square loops of AHE indicating that PMA is large, and relaxation is very slow in TbIG. However, in a 100 nm thick sample, The AHE hysteresis loop is not a perfectly square loop as seen in figure 7-3, (c) telling that the spins are not perfectly out of plane, but they have some angles tilted into in plane. In other words, the squareness in this case is not one anymore. All of AHE measurements are taken at room temperature,

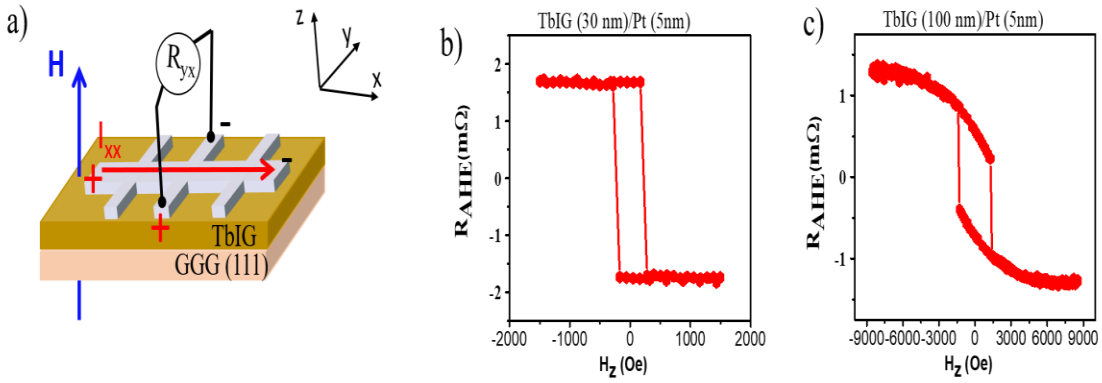

Figure 7- 3: Schematic illustration of AHE measurements geometry and AHE hysteresis loops measured in TbIG/Pt (5nm) bilayer for 30 and 100 nm thicknesses of TbIG at room temperature. a) Hall—bar pattern for 5nm Pt deposited on TbIG thin films. All connections are specified to define (R_{yx}) and field is applied in the out-of-plane direction. Transport measurements of AHE resistance as function of magnetic field yielding square hysteresis loop for TbIG (30 nm)/Pt(5 nm) at room temperature. c) the same as b) except the thickness of TbIG is 100 nm which indicates that some magnetic component is in film plane.

As we engineer PMA in other REIG thin films where the strain ratio, magnetostriction constant and total magnetizations are different, we aim to compare the AHE magnitude with respect to total magnetization. In this comparison, besides TbIG, we choose $Eu_3Fe_5O_{12}$ (EuIG) which is not discussed in this thesis and $Tm_3Fe_5O_{12}$ (TmIG) which is discussed elsewhere[9,10]. To make a fair comparison, we need to keep the REIG and Pt thicknesses constant at 30 nm and 5 nm respectively for the three bilayers. From the transport measurements, the magnitude of AHE resistivity (ρ_{AHE}) for the REIG/Pt systems are 0.429, 0.529, and 0.89 $n\Omega \cdot cm$ as appeared in Figure 7-4, (a) for EuIG/Pt, TmIG/Pt and TbIG/Pt, respectively. Figure 7-4, (b) shows the comparison of both measured $4\pi M_s$ and ρ_{AHE} from figure 7-4, (a) among all three bilayers. The $4\pi M_s$ value is 1400 G for TmIG, 915 G for EuIG, and 225 G for TbIG. The difference in the magnetization is due to the different magnetic moment of the rare-earth elements which

are coupled antiferromagnetically with the net Fe^{3+} moment and causes partial compensation of the net Fe^{3+} moment. Note that the ($4\pi M_s$) decreases from TmIG to TbIG by a factor of five whereas ρ_{AHE} stays in nearly the same range for all of them. This sharp contrast clearly indicates that the ρ_{AHE} of the Pt layer is correlated with the net magnetic moment of sublattices of Fe^{3+} ions, which is a constant, rather than the total magnetic moment of REIGs (including Fe^{3+} and RE^{3+}). This can be explained by the fact that the conduction electrons of Pt are primarily hybridized with the 3*d* Fe^{3+} electrons which are more spatially extended than the 4*f* electrons of the rare earth elements.

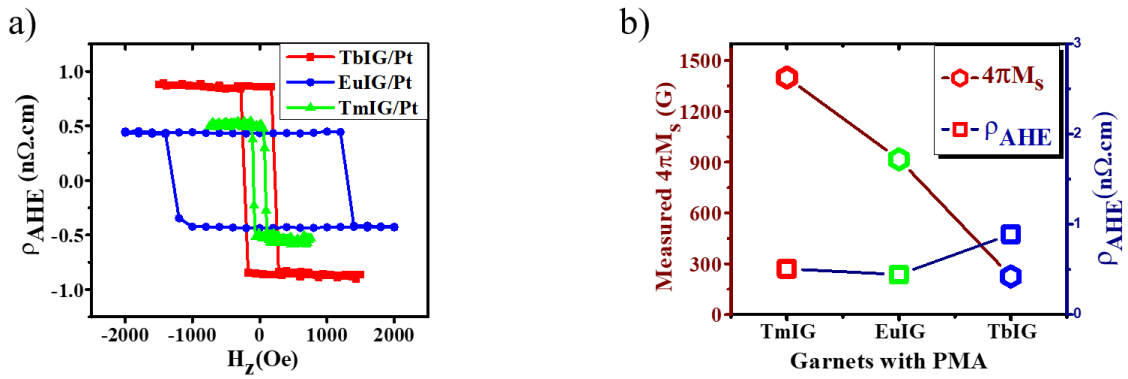

Figure 7- 4: AHE resistivities in three REIG thin films and comparison between AHE magnitude and total magnetization for both REIG thin films/Pt. a) The anomalous Hall resistivity measured with an out-of-plane field sweep for three PMA garnets (TbIG (30 nm)/Pt(5 nm), EuIG(30 nm)/Pt(5 nm) and TmIG(30 nm)/Pt(5 nm)). (b) Measured magnetization values ($4\pi M_s$) and anomalous Hall resistivity magnitude as a function of PMA garnets (TbIG, EuIG and TmIG).

7.5 Analysis and Discussion of PMA Field

An important factor is the combination of the lattice-mismatch-induced in-plane compressive strain and positive magnetostriction coefficients which can drive the

magnetization perpendicular to the film plane in TbIG. The strong PMA in TbIG films is characterized by squared magnetic hysteresis loops for out-of-plane fields and hard-axis behavior for in-plane fields.

Magnetic anisotropy energy of thin films in general consists of three terms and can be written as

$$K_u = 2\pi {M_s}^2 + K_c + K_\sigma, \qquad (6)$$

where K_c is magnetocrystalline anisotropy which can be approximated by the first-order cubic anisotropy constant (K_1). In TbIG, (K_1) is negative and ($\approx -10^4 erg/cm^3$); the term $2\pi {M_s}^2$corresponds to the shape anisotropy ($\approx 10^4 erg/cm^3$) which gives the in-plane demagnetizing field; K_σ is the strain-induced anisotropy which is determined by magnetostriction coefficient (λ_{lmn}) and in-plane strain ($\varepsilon_{||}$). For TbIG, K_σ is positive and large ($\approx 10^5 erg/cm^3$) as can be seen in Table 7-2. As a result, comparing these three anisotropies, K_σ is at least one order of magnitude larger than K_c and $2\pi {M_s}^2$.

Therefore, to evaluate how the compressive strain influences the magnetic anisotropy, magneto-transport measurements in TbIG/Pt bilayers are performed at room temperature with either an electromagnet or a superconducting magnet in a physical property measurement system. So, we first determine the anisotropy field from the hard-axis AHE loops and quantitatively study *t*-dependence in TbIG/Pt(5 nm). TbIG shows perpendicular magnetization for all films with the thickness up to 100 nm. This is primarily due to a smaller saturation magnetization value in TbIG which causes the PMA field to be dominant over the demagnetizing field in the entire thickness range. Detailed

transport measurements for the Hall resistivity (ρ_{AHE}) and longitudinal magnetoresistance (MR) (R_{xx}) responses are performed with *in-plane field sweeps* as drawn in figure 5-7, (a) to reach the in-plane magnetic field saturation value (H_S^{ip}) in which both ρ_{AHE} and R_{xx} signals saturate. Figure 7-5, (b and c) show an example of the H_S^{ip} extraction procedure for TbIG (60 nm)/Pt (5 nm) with perpendicular magnetization easy axis from both the Hall and MR signals which give the same value. Dashed lines define the positive and negative saturation of the in-plane field (H_S^{ip}). For 60 nm thick TbIG, the saturation field from both Hall and MR is ~ 17.50 kOe as featured in figure 7-5, (b and c).

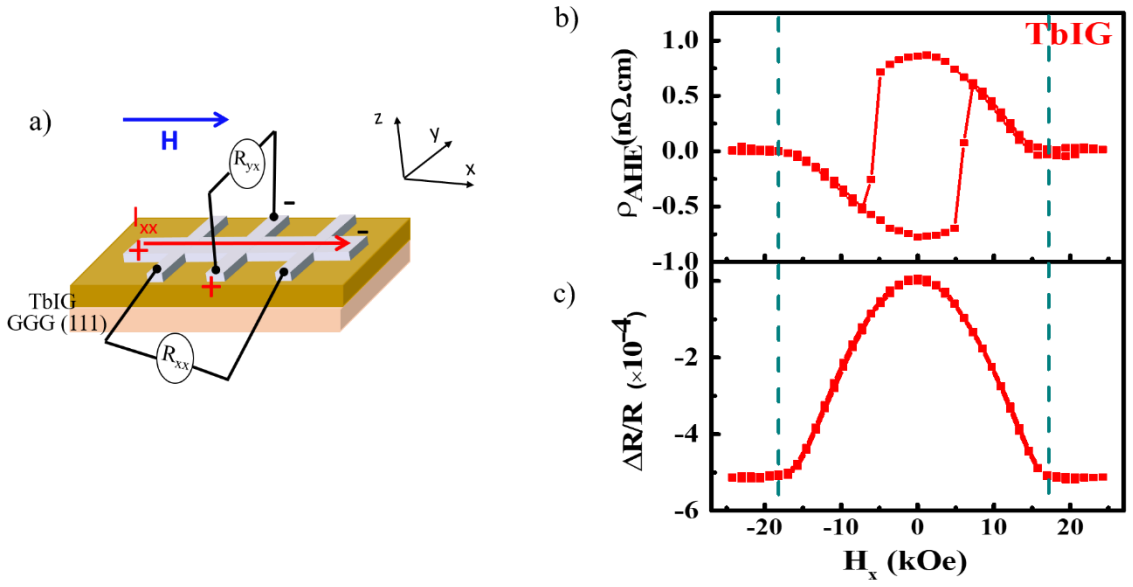

Figure 7- 5: Measurement geometry and Hall resistivity (ρ_{AHE}) and longitudinal magnetoresistance ratio ($\Delta R/R$) measurements as a function of in-plane magnetic field for TbIG/Pt at room temperature. a) Schematic drawing of both Hall and MR measurements with sweeping magnetic field in in-plane field. b) Hall resistivity (ρ_{AHE}) as a function of in-plane magnetic field for TbIG (60 nm)/Pt(5 nm). c) Longitudinal magnetoresistance ratio ($\Delta R/R$) as a function of in-plane magnetic field for TbIG (60 nm)/Pt(5 nm). The dashed lines represent the saturation magnetic field for in-plane geometry.

From transport measurements, $H_{\perp}$ is extracted from the following relation

$$H_S^{ip} = H_{\perp} - 4\pi M_s \qquad (7)$$

Figure 7-6, (a) shows the plot $H_{\perp}$ as a function of film thickness (*t)* where $H_{\perp}$ follows a $1/(t+t_o)$ behavior where $H_{\perp} = \left(\frac{4472.76}{t+48.50} - 24.36\right) kOe$ for TbIG as it has been observed in other works[11]. As described in equations (1) and (2), $H_{\perp}$ has a linear relation with the in-plane strain $\varepsilon_{\parallel}$, which in turn is proportional to the out-of-plane strain $\varepsilon_{\perp}$ according to equations (3), hence, it is expected that $H_{\perp}$ follows the same behavior as the out-of-plane strain, $\varepsilon_{\perp}$. According to the general model formulated for the effect of lattice mismatch in thin films[12], two regimes exist: for film thickness *t* below certain critical value t_c, the film will be pseudomorphic and the strain is given by $\varepsilon_{\parallel} = \eta = \frac{a_f - a_s}{a_s}$, while for $t > t_c$, the strain relaxes as $\varepsilon_{\parallel} \propto \eta \frac{t_c}{t}$. Figures 7-6, (b) shows that for the measured thickness ($t > 4$ nm), only the $1/(t+t_o)$ behavior is observed, indicating that the strain in the lattice relaxes over the entire thickness range. The fitted equation for the out-of-plane strain versus thickness is found to be $\varepsilon_{\perp} = 0.0001 + \frac{0.6237}{t+48.50}$; for TbIG these equations lead to a residual out-of-plane strain of 0.01% for TbIG when the film thickness is large enough to be considered to be in the bulk regime.

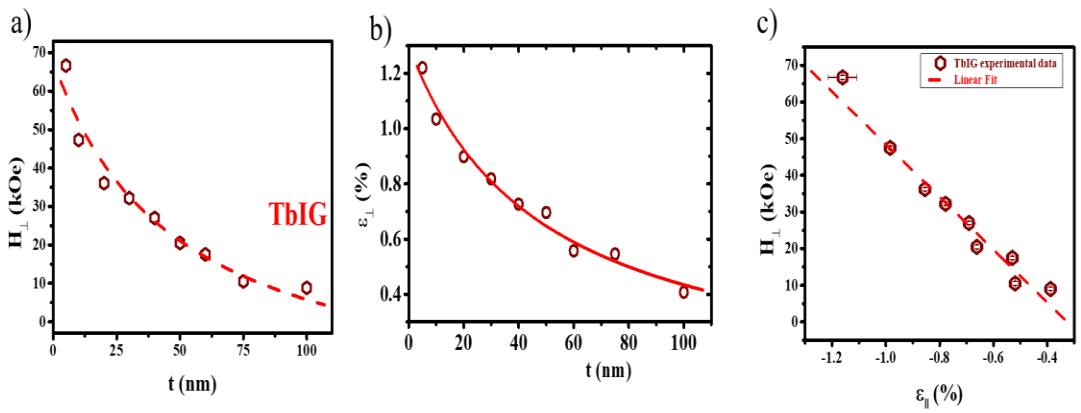

Figure 7- 6: Perpendicular magnetic anisotropy field $H_\perp$ and strain as a function of different thicknesses of TbIG thin films. a) $H_\perp$ as a function of TbIG thicknesses. b) out-of-plane strain $\varepsilon_\perp$ as a function of film thickness, showing the corresponding $1/t+t_o$ behavior for the measured interval. c) $H_\perp$ as a function of in-plane strain $\varepsilon_\parallel$ for TbIG. The dashed line is linear fit to obtain thin film magnetostriction constant (λ_{111}) for TbIG.

Figure 7-6, (c) shows $H_\perp$ as a function of $\varepsilon_\parallel$ for TbIG where a linear relation was observed. A least square fitting was performed and the magnetostriction coefficient λ was calculated. For TbIG, it was found that $\lambda_{111} = (1.35 \pm 0.06)\times10^{-5}$, being only 12% larger than the literature value ($\lambda_{111} = 1.2\times10^{-5}$),[4] this small variation may be attributed to the difference in growth conditions of both bulk and thin film samples which result in slightly different material properties and additionally the difference in measurement techniques.

The table below is a summary of the complete study parameters for different thicknesses ranging from 5 to 100 nm. For example, it lists all strained lattice constants measured by XRD, both out-of-plane tensile strain and in-plane compressive strain ratios,

magnetization for individual thickness, both saturation magnetic field in plane and PMA field. Finally, the uniaxial magnetic antitropy constant (K_u) is calculated from this relation

$$K_u = \frac{1}{2} M_s \times (H_{sat} + 4\pi M_s)$$

GGG (111)/TbIG								
Thickness (nm)	c (Å)	$\epsilon_\perp$(%)	$\epsilon_\parallel$(%)	$\sigma_\parallel \times 10^{10}$ (dyne/cm^2)	$4\pi M_s$ (Gauss)	H_{sat} (kOe)	$H_\perp$ (kOe)	$K_u \times 10^5$ (erg/cm^3)
5	12.587	1.22	-1.16	-3.71	--	66.50	66.73*	6.213*
10	12.564	1.03	-0.98	-3.14	--	47.25	47.48*	4.421*
20	12.547	0.90	-0.86	-2.73	253	36.00	36.25	3.652
30	12.537	0.82	-0.78	-2.48	223	32.00	32.22	2.852
40	12.525	0.73	-0.69	-2.21	242	26.75	26.99	2.598
50	12.522	0.70	-0.66	-2.11	221	20.25	20.47	1.803
60	12.504	0.56	-0.53	-1.69	230	17.25	17.48	1.603
75	12.503	0.55	-0.52	-1.66	247	10.25	10.50	1.030
100	12.486	0.41	-0.39	-1.24	222	8.75	8.97	0.792

Table 7- 2: Summary of strained lattice constants, both out of plane and in-plane stain calculations, magnetic property, PMA field and uniaxial magnetic anisotropy constant for TbIG films with thickness $5 \leq t \leq 100$ nm on GGG (111). The $H_\perp$ and K_u values marked with (*) were calculated using the average $4\pi M_s$ values.

7.6 Hardness in Switching of Tb Spin in (TbIG/Pt)

It is reported that the single crystal bulk of TbIG has a compensation temperature (T_{comp}) at 246 K [13,14] indicating the net magnetization goes to zero. Based on the magnetic structure of TbIG as drawn in figure 7-7, (d and e) the total magnetization of the sublattices of (*Fe*) on *a* site and (*Tb*) on *c* site is equal in magnitude with the anti-parallel magnetization of (*Fe*) sublattice on the *d* site at T_{comp}. It is good to mention that, Tb^{3+} ion has eight electrons in its *f*-subshell electronic configuration and thus six electrons unpaired which makes Tb magnetically ordered and thus it contributes to the total magnetization. In thin films reported in this thesis, we probe T_{comp} through measurements of AHE via sign change. That can be seen in figure 7-7, (a) where the AHE has a conventional (negative) sign whereas in figure (b) has a reverse sign proving the TbIG goes through T_{comp} and in all thickness from 10 to 100 nm, the T_{comp} window is between 240 and 230K. In figure 7-7, (d), schematic diagram shows the larger magnetic moments of *Fe* on *d* site are determining the magnetization by alignment with applied magnetic field for temperature above T_{comp}. Also, the other *Fe* on *a* and *Tb* on *c* are aligned antiferromagnetically with *Fe* on *d* due to super-exchange coupling discussed in chapter one. With decreasing temperature, the magnetization of *Tb* strongly increases, and its magnitude become larger than that of *Fe* on *d* below T_{comp}, therefore, the magnetic moments of Tb and *Fe* on *a* align with the magnetic field due to Zeeman energy where larger magnetization aligns with the field.

Just above and below T_{comp}, we observe a huge shift in the AHE loop as seen in figure 7-7, (a and b). First, depending on the initial state of both *Tb* and *Fe* spins, we can control this loop shift to be a negative or positive value. We start the measurement at 340 ˚C by sweeping the field from +0.9 to -0.9 T which means the initializing *Fe* spins are positive as they aligned with the magnetic field whereas the *Tb* spins have to be down (anti-parallel). As the induced AHE senses *Fe* moments and not the contribution of *Tb*, we infer its contribution by its effect on the moment of Fe. When the magnetic field decreases to negative where the *Fe* spins need to be switched with the field, the spins are difficult to switch due to the effective magnetic field produced by *Tb* in the opposite direction such that the *Fe* spins require a much larger magnetic field to switch in the temperature regime where the AHE shift occurs as seen clearly in figure 7-7, (a). We define this AHE shift by the shift in our measured hysteresis loops with respect the zero-magnetic field axis and it is calculated using $H_{Hardness\ shift} = \left|H_{(-)} + H_{(+)}\right|/2$ where $H_{(-)}$ and $H_{(+)}$ are the left and right coercive fields respectively. We cool the sample in zero field cooling (ZFC) procedure and the AHE shift in not noticeable until 268 K where the shift is -150 Oe. This hardness shift increases gradually to maximum value of -5500 Oe at 240K. Below compensation temperature ~233 K, all results are reversed due to *Tb* spins aligning with magnetic field and thus the Fe spins align in the opposite direction as seen in the sketch of figure 7-7, (d). Also, the AHE loop and hardness shift are positive with maximum shift of +850 Oe at 232.5 K. This hardness shift as a function of temperature reaches its maximum value around the compensation temperature whereas as is almost zero from 340 to 275 K and from 220 K to our lowest measured temperature of

4 K. As for the coercive field, H_c, it increases dramatically to the maximum value of 9.5 kOe at 240 K and then decreased gradually to 1.5 kOe at 100 K and then increase to 5.5 kOe at 4 K.

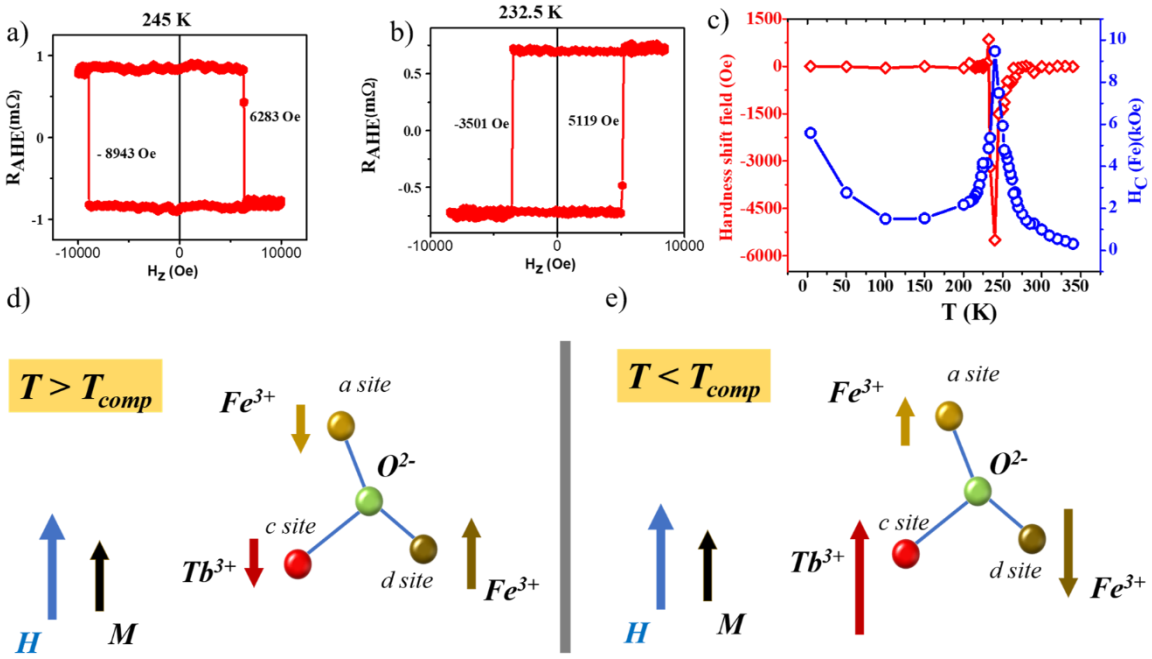

Figure 7- 7: Hardness shift in AHE hysteresis loop shift and schematic drawing of magnetic structure of TbIG above and below compensation temperature. a) Negative hardness shift in AHE hysteresis loop above T_{comp} (245K). b) Positive hardness shift in AHE hysteresis loop below T_{comp} (232.5 K). c) Hardness shift and coercive fields as a function of temperatures. d) Magnetic structure of sublattices of TbIG above T_{comp}. e) Magnetic structure of sublattices of TbIG below T_{comp}. The net magnetization ***M*** points along the external magnetic field ***H.*** The length of these arrows represents the magnitude of the magnetization of sublattices ions. d) and e) are adapted from Nature Comm. **7**, 10452 (2016).

The hardness of some Tb switching can be overcome by an applying a field which is large enough to force them to switch. An example is pictured in figure 7-8, (a). At 250 K where hardness shift field is observed up to 2 T and then it decreases slightly as field

increases up to 7 T and finally vanishes at 8.5 T indicating the field required to switch all Tb spins. Figure 7-8, (b) shows the full hardness switching field for *Tb* spins as function of temperature where the hardness switching field reaches its maximum of 14 T at 240 K. From the temperature dependence it is clear that both *Tb* and *Fe* spins switch together at the same field from 340 to 275 K and as well as below 220 K.

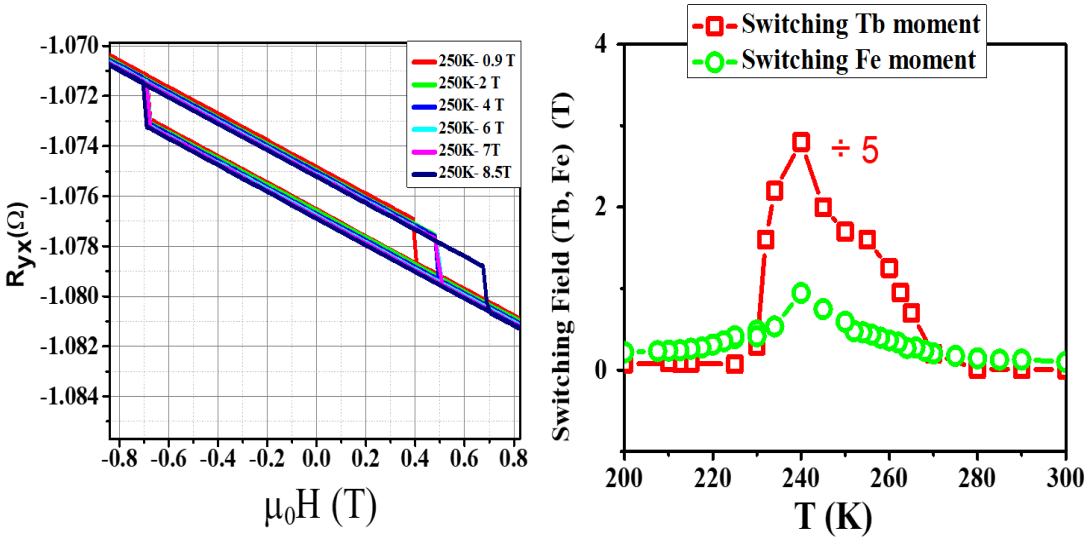

Figure 7- 8: Hardness switching field for different applied magnetic field and switching field for Tb and Fe spin as a function of Temperature. a) AHE hysteresis loop with hardness shift change at different applied field as an example of how to switch frozen Tb spins. b) Tb and Fe switching field as a function of temperature showing the maximum field to switch both at 240 K.

In summary, we have examined compressive in-plane strain engineering for materials with a positive magnetostriction constant as an effective way to tune the perpendicular magnetic anisotropy in coherently strained epitaxial TbIG (111) thin films. Electrical measurements performed on Pt Hall bars fabricated on these films show squared AHE hysteresis loops which are primarily sensitive to the net magnetic moments of Fe^{3+}. The PMA field decreases as ferrimagnetic insulator thickness increases due to slow relaxation of the in-plane strain. The magnetostriction value determined in our experiments are comparable to the ones reported for bulk crystals. More interesting, we observe a shift of AHE loop around the compensation temperature which is either positive or negative based on the initialization of the magnetic state and ascribe this huge shift to some frozen magnetic moments of Tb ions.

References:

1. Farle, M., Mirwald-Schulz, B., Anisimov, A.N., Platow, W. & Baberschke, K. Higher-order magnetic anisotropies and the nature of the spin-reorientation transition in face-centered-tetragonal Ni(001)/Cu(001). *Physical Review B* **55**, 3708-3715 (1997).

2. Qiu, Z.Q., Pearson, J. & Bader, S.D. Asymmetry of the spin reorientation transition in ultrathin Fe films and wedges grown on Ag(100). *Physical Review Letters* **70**, 1006-1009 (1993).

3. Ikeda, S. et al. A perpendicular-anisotropy CoFeB–MgO magnetic tunnel junction. *Nature Materials* **9**, 721 (2010).

4. Iida, S. Magnetostriction Constants of Rare Earth Iron Garnets. *Journal of the Physical Society of Japan* **22**, 1201-1209 (1967).

5. Anastassakis, E. Strained superlattices and heterostructures: Elastic considerations. *Journal of Applied Physics* **68**, 4561-4568 (1990).

6. Navarro-Quezada, A., Rodríguez, A.G., Vidal, M.A. & Navarro-Contreras, H. In-plane and out-of-plane lattice parameters of [11n] epitaxial strained layers. *Journal of Crystal Growth* **291**, 340-347 (2006).

7. Alberts, H.L. Elastic constants of single crystal terbium iron garnet. *Journal of Physics and Chemistry of Solids* **41**, 1161 (1980).

8. Winkler, G.D. Magnetic garnets / Gerhard Winkler (Vieweg, Braunschweig, 1981).

9. Tang, C. et al. Anomalous Hall hysteresis in Tm3Fe5O12/Pt with strain-induced perpendicular magnetic anisotropy. *Physical Review B* **94**, 140403 (2016).

10. Masashi, K. et al. Stress-Induced Perpendicular Magnetization in Epitaxial Iron Garnet Thin Films. *Applied Physics Express* **5**, 103002 (2012).

11. Bochi, G., Ballentine, C.A., Inglefield, H.E., Thompson, C.V. & O'Handley, R.C. Perpendicular magnetic anisotropy, domains, and misfit strain in epitaxial Ni/Cu 1− x Ni x/Cu/Si (001) thin films. *Phys. Rev. B* **52**, 7311 (1995).

12. Chappert, C. & Bruno, P. Magnetic anisotropy in metallic ultrathin films and related experiments on cobalt films. *J. Appl. Phys.* **64**, 5736-5741 (1988).

13. Geller, S., Remeika, J.P., Sherwood, R.C., Williams, H.J. & Espinosa, G.P. Magnetic Study of the Heavier Rare-Earth Iron Garnets. *Physical Review* **137**, A1034-A1038 (1965).

14. Guillot, M. & Le Gall, H. Magnetic study of the terbium iron garnet, Tbig, along the easy (111) direction : molecular field parameters. *Journal de Physique* **38**, 871-875 (1977).